

# H I 21-cm absorption survey of quasar-galaxy pairs: Distribution of cold gas around $z < 0.4$ galaxies

R. Dutta<sup>1\*</sup>, R. Srianand<sup>1</sup>, N. Gupta<sup>1</sup>, E. Momjian<sup>2</sup>, P. Noterdaeme<sup>3</sup>, P. Petitjean<sup>3</sup>, H. Rahmani<sup>4</sup>

<sup>1</sup> *Inter-University Centre for Astronomy and Astrophysics, Post Bag 4, Ganeshkhind, Pune 411007, India*

<sup>2</sup> *National Radio Astronomy Observatory, 1003 Lopezville Road, Socorro, NM 87801, USA*

<sup>3</sup> *Institut d'Astrophysique de Paris, CNRS and UPMC Paris 6, UMR7095, 98bis boulevard Arago, 75014 Paris, France*

<sup>4</sup> *Aix Marseille Université, CNRS, LAM (Laboratoire d'Astrophysique de Marseille) UMR 7326, 13388, Marseille, France*

Accepted. Received; in original form

## ABSTRACT

We present the results from our survey of H I 21-cm absorption, using GMRT, VLA and WSRT, in a sample of 55  $z < 0.4$  galaxies towards radio sources with impact parameters ( $b$ ) in the range  $\sim 0$ –35 kpc. In our primary sample (defined for statistical analyses) of 40 quasar-galaxy-pairs (QGP), probed by 45 sightlines, we have found seven H I 21-cm absorption detections, two of which are reported here for the first time. Combining our primary sample with measurements having similar optical depth sensitivity ( $\int \tau dv \leq 0.3 \text{ km s}^{-1}$ ) from the literature, we find a weak anti-correlation (rank correlation coefficient =  $-0.20$  at  $2.42\sigma$  level) between  $\int \tau dv$  and  $b$ , consistent with previous literature results. The covering factor of H I 21-cm absorbers ( $C_{21}$ ) is estimated to be  $0.24^{+0.12}_{-0.08}$  at  $b \leq 15$  kpc and  $0.06^{+0.09}_{-0.04}$  at  $b = 15$ –35 kpc.  $\int \tau dv$  and  $C_{21}$  show similar declining trend with radial distance along the galaxy's major axis and distances scaled with the effective H I radius. There is also tentative indication that most of the H I 21-cm absorbers could be co-planar with the extended H I discs. No significant dependence of  $\int \tau dv$  and  $C_{21}$  on galaxy luminosity, stellar mass, colour and star formation rate is found, though the H I 21-cm absorbing gas cross-section may be larger for the luminous galaxies. The higher detection rate (by a factor of  $\sim 4$ ) of H I 21-cm absorption in  $z < 1$  DLAs compared to the QGPs indicates towards small covering factor and patchy distribution of cold gas clouds around low- $z$  galaxies.

**Key words:** galaxies: quasar: absorption line – galaxies: ISM

## 1 INTRODUCTION

The H I gas in a galaxy's extended disc plays an indispensable role in the galaxy formation and evolution by acting as the intermediary phase between the accreting ionized gas from the intergalactic medium (IGM) and the molecular gas phase in the stellar disc that gets converted to stars. Being more extended than the stellar disc (typically by more than a factor of 2), the H I disc is also the component that gets affected the most by tidal interactions and merger events (Haynes et al. 1979; Rosenberg & Schneider 2002; Oosterloo et al. 2007; Sancisi et al. 2008; Chung et al. 2009; Mihos et al. 2012). Therefore, the H I cross-section of galaxies and its evolution with redshift is expected to have an imprint on galaxy formation in the hierarchical structure formation models.

In the local Universe ( $z \lesssim 0.2$ ), high spatial resolution H I 21-cm emission studies have been used to map the distribution and

kinematics of the atomic gas around galaxies (van der Hulst et al. 2001; Zwaan et al. 2001; Verheijen et al. 2007; de Blok et al. 2008; Walter et al. 2008; Begum et al. 2008; Catinella & Cortese 2015). However, sensitivities of present day radio telescopes make it difficult to directly map H I 21-cm emission from  $z \gtrsim 0.2$  galaxies. The highest redshift ( $z = 0.376$ ) H I 21-cm emission detection to date (Fernández et al. 2016) has been possible due to very long integration (178 hours) using the Karl G. Jansky Very Large Array (VLA). Alternatively, absorption lines seen in the spectra of background quasars whose sightline happen to pass through the discs or halos of foreground galaxies (we refer to such fortuitous associations as quasar-galaxy-pairs or QGPs from hereon), allow us to probe the physical, chemical and ionization state of gas in different environments such as the stellar discs, extended H I discs, high velocity clouds, outflows, accreting streams and tidal structures. The relationship between absorption strength and impact parameter ( $b$ ) obtained from a large number of quasar sightlines passing near foreground galaxies can then be used to statistically deter-

\* E-mail: rdutta@iucaa.in

mine the gas distribution in and around galaxies (as pioneered by Bergeron & Boissé 1991; Steidel 1995, in case of Mg II systems).

Considerable progress has been made in mapping the distribution of gas in the circumgalactic medium (CGM), that extends upto  $\sim 100$ s of kpc, using absorption from Mg II (Chen et al. 2010; Kacprzak et al. 2011; Churchill et al. 2013; Nielsen et al. 2013) as well as Lyman  $-\alpha$  (Chen et al. 2001; Prochaska et al. 2011; Tumlinson et al. 2013; Stocke et al. 2013; Borthakur et al. 2015). On the other hand, the high column density H I gas around galaxies can be traced using Damped Lyman  $-\alpha$  absorption-line systems (DLAs) (absorbers with neutral hydrogen column density,  $\log N(\text{H I}) \geq 20.3$ ; see for a review Wolfe et al. 2005). Observations of host galaxies of DLAs have found anti-correlation between  $N(\text{H I})$  and  $b$ , at  $z < 1$  (Rao et al. 2011), at  $1 < z < 2$  (Péroux et al. 2012; Rahmani et al. 2016), and at  $z > 2$  (Krogager et al. 2012). At  $z = 0$ , Zwaan et al. (2005), using H I 21-cm emission maps of local galaxies, have found that  $N(\text{H I})$  decreases with galactocentric radius.

H I 21-cm emission line observations of nearby dwarf and spiral galaxies indicate that the properties of the cold neutral medium (CNM) phase of the H I gas and small-scale structures detected in the H I gas are closely linked with the in-situ star formation in galaxies (e.g. Tamburro et al. 2009; Bagetakos et al. 2011; Ianjamasimanana et al. 2012). However, identification of CNM gas through H I 21-cm emission is not straightforward as it depends on Gaussian decomposition of the line profiles and associating components exhibiting smaller line widths with the CNM. Moreover, H I 21-cm emission studies usually do not have sufficient spatial resolution to detect parsec-scale structures. On the other hand, H I 21-cm absorption is an excellent tracer of the CNM phase (Kulkarni & Heiles 1988), and can be used to study parsec-scale structures in the H I gas using sub-arcsecond-scale spectroscopy (e.g. Srianand et al. 2013; Biggs et al. 2016). The optical depth of the H I 21-cm absorption line depends on  $N(\text{H I})$  and inversely on the spin temperature ( $T_s$ ), which is known to follow the gas kinetic temperature in the CNM (Field 1959; Bahcall & Ekers 1969; McKee & Ostriker 1977; Wolfire et al. 1995; Roy et al. 2006), and can be coupled to the gas kinetic temperature via the Lyman  $-\alpha$  radiation field in the warm neutral medium (WNM) (Liszt 2001). This along with its very low transition probability and its resonance frequency falling in the radio wavelengths make the H I 21-cm absorption line a good tracer of high column density cold H I gas without being affected by dust and luminosity biases.

Systematic searches of H I 21-cm absorption in samples of intervening Mg II systems and DLAs towards radio-loud quasars have estimated the CNM filling factor of galaxies as 10–20% (Briggs & Wolfe 1983; Kanekar & Chengalur 2003; Curran et al. 2005; Gupta et al. 2009; Curran et al. 2010; Srianand et al. 2012; Gupta et al. 2012; Kanekar et al. 2014). However, such studies have led to degenerate interpretations of the evolution of cold atomic gas fraction of galaxies, since there is a degeneracy between  $T_s$  and the fraction  $C_f$  of the background radio source covered by the absorbing gas. Moreover, selection based on optical/ultraviolet (UV) spectra leads to bias against dusty sightlines.

An alternative technique, that connects the H I 21-cm absorption with the galaxy properties, has been to search for H I 21-cm absorption from low- $z$  ( $z < 0.4$ ) QGPs (e.g. Carilli & van Gorkom 1992; Gupta et al. 2010; Borthakur et al. 2011; Borthakur 2016; Zwaan et al. 2015; Reeves et al. 2016). Such studies have revealed a weak anti-correlation between the H I 21-cm optical depth and impact parameter (Gupta et al. 2013; Zwaan et al. 2015; Curran et al. 2016). However, the number of low- $z$  QGPs that have

been searched for H I 21-cm absorption, with a good optical depth sensitivity (i.e.,  $3\sigma$  integrated optical depth, for a line width of  $10 \text{ km s}^{-1}$ , is  $\leq 0.3 \text{ km s}^{-1}$ , which is sensitive to detect 100 K gas with  $N(\text{H I})$  of  $\leq 5 \times 10^{19} \text{ cm}^{-2}$ ), till date is still small. As  $N(\text{H I})$  of few times  $10^{19} \text{ cm}^{-2}$  is observed in the outer disks of galaxies in H I 21-cm emission maps (e.g. van der Hulst et al. 2001; Walter et al. 2008), any survey aiming to detect CNM gas in galaxies via H I 21-cm absorption should reach such limiting column densities. Further, the connections between the distribution of H I 21-cm absorbers around low- $z$  galaxies and different parameters of galaxies, in particular, those that are governed by the ongoing star formation in these galaxies, geometry and stellar distributions of galaxies, are not yet well-established.

Here we present the results from our systematic survey of H I 21-cm absorption in a large homogeneous sample of  $z < 0.4$  galaxies. Our survey has resulted in seven H I 21-cm detections, the largest from any single survey of low- $z$  QGPs. The measurements from our survey increase the existing number of sensitive H I 21-cm optical depth measurements (as defined above) at low- $z$  by a factor of three, and the number of H I 21-cm absorption detections from QGPs by almost a factor of two. In addition, while most studies of QGPs in the literature have focused at  $z \lesssim 0.1$ , our sample probes galaxies upto  $z \sim 0.4$ , and has produced four H I 21-cm detections at  $z \geq 0.1$ . In this work, combining the H I 21-cm absorption measurements with the host galaxy properties, we attempt to statistically determine the distribution of H I 21-cm absorbers and hence that of cold H I gas around low- $z$  galaxies.

Identifying how the H I 21-cm absorption line properties depend on the locations of the radio lines-of-sight with respect to the foreground galaxies is essential to make progress in using H I 21-cm absorption measurements in future blind H I 21-cm absorption surveys (Morganti et al. 2015), with the Square Kilometre Array (SKA) pre-cursors like MeerKAT (Jonas 2009) and ASKAP (DeBoer et al. 2009) and pathfinders like AperTIF (Verheijen et al. 2008) and uGMRT, to probe galaxy evolution. These surveys are expected to detect several hundred H I 21-cm absorbers. Hence, we expect that the results from our survey would play a crucial role in interpreting the huge volume of data expected from these upcoming surveys. In addition, our study will help to bridge the missing link between the Galactic interstellar medium (ISM) studies and high redshift ( $z > 1$ ) H I 21-cm absorber studies for which host galaxy properties are difficult to study using present day telescopes.

This paper is structured as follows. In Section 2, we describe the sample selection and various properties of the galaxies in our sample. In Section 3, we describe our radio observations using the Giant Metrewave Radio Telescope (GMRT), VLA and Westerbork Radio Synthesis Telescope (WSRT), and optical observations using the South African Large Telescope (SALT). In Section 4, we discuss the physical conditions in a few individual systems from our sample. Next, we study the distribution of H I 21-cm absorbers around low- $z$  galaxies and their dependence on host galaxy properties in Section 5. We discuss our results in Section 6 and conclude by summarizing our results in Section 7. Throughout this work we have adopted a flat  $\Lambda$ -CDM cosmology with  $H_0 = 70 \text{ km s}^{-1} \text{ Mpc}^{-1}$  and  $\Omega_M = 0.30$ .

## 2 SAMPLE DESCRIPTION

### 2.1 Sample Selection

At first we constructed a parent sample of QGPs using the Sloan Digital Sky Survey (SDSS; York et al. 2000) and the Faint Im-

ages of the Radio Sky at Twenty-Centimeters (FIRST; White et al. 1997) databases. To do this we cross-matched SDSS-Data Release 9 (DR9) galaxies with photometric redshift,  $z_{\text{phot}} \leq 0.4$ , and FIRST radio sources with peak flux density at 1.4 GHz  $\geq 50$  mJy within a  $40''$  search radius. The redshift range was chosen to ensure that the redshifted H I 21-cm absorption frequency is uniformly covered at the most sensitive radio interferometers (i.e. GMRT, VLA and WSRT), and to maximize the possibility of sub-arcsecond-scale spectroscopic and H I 21-cm emission follow-ups. The search radius was chosen to restrict to radio sightlines that would probe the foreground galaxies at low impact parameters ( $40''$  corresponds to  $b = 16\text{--}215$  kpc for the range of  $z_{\text{phot}} = 0.02\text{--}0.4$  of the sample, with  $b = 93$  kpc at median  $z_{\text{phot}} = 0.13$ ). The flux density cut on the radio sources was imposed in order to obtain a H I 21-cm optical depth sensitivity, defined as  $3\sigma$  upper limit on the integrated optical depth from spectra smoothed to  $10 \text{ km s}^{-1}$ ,  $\int \tau dv_{10}^{3\sigma} \leq 0.3 \text{ km s}^{-1}$ . This corresponds to a sensitivity of  $N(\text{H I}) \leq 5 \times 10^{19} \text{ cm}^{-2}$  for  $T_s = 100 \text{ K}$  and  $C_f = 1$ . Note that  $10 \text{ km s}^{-1}$  is the typical width of the individual H I 21-cm absorption line components detected from QGPs (see Section 3.2). We then visually inspected the SDSS images of the resultant pairs to confirm that the galaxies have been correctly identified. This selection technique resulted in 106 QGPs which we refer to as the SDSS parent sample. Note that at this stage we did not place any condition on the nature of the radio source except for a flux density cut. For simplicity, we use the term QGP to refer to all pairs of radio sources and galaxies throughout this work, irrespective of the nature of the radio sources.

We carried out H I 21-cm absorption line searches for 43 of the QGPs in the SDSS parent sample. To select which sources to observe from the parent sample, preference was given to those QGPs: (a) which had spectroscopic redshift of the galaxy already available from SDSS or the literature, (b) whose optical spectra we were able to obtain with the optical telescopes accessible to us, and (c) which had impact parameters (based on spectroscopic redshift)  $\lesssim 30$  kpc. We restricted to QGPs with  $b \lesssim 30$  kpc, as ground-based imaging studies of galaxies responsible for DLAs/sub-DLAs at  $0.1 \leq z \leq 1$  have found that DLA and sub-DLA column densities occur at median impact parameters of 17 and 33 kpc, respectively (Rao et al. 2011). Further, the expected median  $b$  for systems with  $\log N(\text{H I}) > 20.3$  is 8 kpc, based on conditional probability distribution of  $N(\text{H I})$  and  $b$  from H I 21-cm emission maps of galaxies at  $z = 0$  (Zwaan et al. 2005).

In addition to the above QGPs from the parent sample, we searched for H I 21-cm absorption from five ‘galaxy on top of quasars’ (GOTOQs; see Noterdaeme et al. 2010; York et al. 2012; Straka et al. 2013), in order to sample sightlines at small impact parameters passing close to the stellar discs of galaxies. The GOTOQs were selected by visually identifying intervening H  $\alpha$  and other emission lines superimposed in the SDSS spectra of the background quasars (with FIRST peak flux density  $\geq 50$  mJy). Additionally, we searched for H I 21-cm absorption towards four quasars where faint optical continuum emission is seen around the quasars in the SDSS images and weak intervening Ca II absorption is detected in the background quasar’s spectrum, but no corresponding emission lines are detected in the SDSS spectrum. Further, in order to include very low- $z$  ( $z \lesssim 0.01$ ) galaxies not present in the SDSS parent sample, we carried out H I 21-cm absorption line search of three QGPs identified from literature (Boisse et al. 1988; Corbelli & Schneider 1990; Womble 1993). At such low- $z$ , sub-arcsecond-scale spectroscopy and H I 21-cm emission observations become feasible. For example, joint analysis of H I 21-cm emission and absorption was possible in case of the QGP, J0041–0143, from

our sample (Dutta et al. 2016). In total, we searched for H I 21-cm absorption from 55 QGPs.

The distribution of the photometric redshift, the angular separation from the background radio source, the SDSS  $r$ -band magnitude, and the observed SDSS  $g - r$  colour for the galaxies in the parent sample are shown in Fig. 1 (open blue histograms). We also show the same for the galaxies searched for H I 21-cm absorption by us in orange shaded histograms. Note that SDSS photometric catalog contains objects to a magnitude limit of  $r \sim 22.5$  mag, which corresponds to  $r$ -band limiting luminosity of  $5.5 \times 10^6 - 3.4 \times 10^9 L_{\odot}$  for the range of  $z_{\text{phot}} = 0.02\text{--}0.4$  of the parent sample, and  $2.7 \times 10^8 L_{\odot}$  at median  $z_{\text{phot}} = 0.13$ . It can be seen from Fig. 1, that due to the requirement of spectroscopic redshifts of galaxies for carrying out H I 21-cm spectral line search, our observed sample is biased towards the brighter and the bluer galaxies from the parent sample, and hence, most of the galaxies observed by us are at  $z_{\text{phot}} \leq 0.2$ .

In order to carryout statistical studies, we categorize the QGPs observed by us as ‘primary’, ‘supplementary’ and ‘miscellaneous’. The primary sample consists of QGPs where we are confident that the radio source is a background source. The supplementary sample consists of QGPs where we are not sure about the radio source being in the background or about the galaxy redshift. The miscellaneous sample consists of QGPs where we are sure that the radio source is not a background source.

(i) *Primary Sample*: Our primary sample consists of 40 QGPs. In all except eight pairs, spectroscopic redshifts of the background radio sources are available in SDSS or in the literature, ensuring that these are background sources. We measured the redshift of one radio source using IUCAA Girawali Observatory (IGO). Out of the seven radio sources without spectroscopic redshifts, four have photometric redshifts available in SDSS which ensure that the probability of  $z_{\text{rad}} > z_{\text{gal}}$  is high, even after taking into account the redshift errors. The remaining three radio sources also have high probability of being  $z \geq 0.5$  quasars and hence background sources, based on their SDSS and WISE colours (Wu et al. 2012). Hence, we take these seven radio sources to be background sources. We discuss in Section 5 the effects of excluding these sources in our statistical analyses. Our primary sample consists of 32 QGPs from SDSS, five GOTOQs, and three  $z \lesssim 0.01$  QGPs selected from literature as mentioned above. Three background radio sources in the primary sample show multiple radio emitting components at arcsecond-scales, that can be used for searching H I 21-cm absorption. Because of this, in total we have 45 radio sightlines around 40 galaxies in our primary sample where we have searched for H I 21-cm absorption. H I 21-cm absorption line searches towards these sources have resulted in seven H I 21-cm detections. The distribution of the photometric redshift, the angular separation from the background radio source, the SDSS  $r$ -band magnitude, and the observed SDSS  $g - r$  colour for the galaxies in the primary sample are shown in Fig. 1 (black shaded histograms).

(ii) *Supplementary Sample*: Our supplementary sample consists of 10 QGPs. In five cases, the radio sources have no optical and infrared counterparts detected in the SDSS and WISE images, respectively. One of the radio sources is detected in the SDSS images but we cannot place any constraints on its redshift. These six sources are included in the supplementary sample, since it cannot be confirmed with the existing data whether these radio sources are behind the galaxies. From the Combined EIS-NVSS Survey Of Radio Source (Best et al. 2003; Brookes et al. 2006, 2008), we see that 21 out of 24, i.e.  $88^{+12}_{-19}\%$ , of the radio sources

brighter than 50 mJy at 1.4 GHz have  $z > 0.4$  (the quoted errors are  $1\sigma$  Gaussian confidence intervals computed using tables 1 and 2 of Gehrels (1986) assuming a Poisson distribution). However, to remove additional sources of uncertainty in our analyses we do not include radio sources without optical/infrared counterparts in our primary sample. Note that H I 21-cm absorption has not been detected towards such radio sources till date. The other four systems in the supplementary sample were identified as potential GTOQs, i.e. faint optical emission is seen around the quasars in the SDSS images and weak Ca II absorption is detected in the quasar’s SDSS spectra. However, no corresponding galactic emission lines are detected in the SDSS spectra. Further, we do not detect any continuum or line emission from foreground galaxies in two of these cases, using SALT long-slit observations with the slit aligned along the extension seen around the quasars. We carried out H I 21-cm absorption line search of these sources at the redshift of the Ca II absorption. We do not include these four sources in the primary sample as the galaxy redshifts are not certain and we cannot rule out the possibility that the optical emission seen around the quasars in SDSS images could be from the quasar host galaxies. No H I 21-cm absorption was detected towards these 10 sources. The measurements from these systems are shown in the plots presented in this work, but they are not included in any of the statistical analyses.

(iii) *Miscellaneous Sample*: We report the H I 21-cm absorption line measurements towards 5 QGPs as part of a miscellaneous sample in this work, but do not include them in any analysis/discussion. Spectroscopic redshifts of the background radio sources were not available in SDSS or in the literature for these systems at the time of their radio observations. We measured the redshift of two radio sources using IGO and SALT and that of three sources subsequently became available in SDSS or in the literature. These radio sources turned out to be either at the same redshift as or slightly lower (within  $\sim 200 \text{ km s}^{-1}$ ) than that of the foreground galaxy. Three of these sources are part of merging systems while two appear to be part of group of nearby galaxies at similar redshifts. H I 21-cm absorption has been detected towards two of the merging galaxy pairs. One of them has already been reported in Srianand et al. (2015). We report for the first time here the detection of a broad ( $\sim 150 \text{ km s}^{-1}$ ) and strong H I 21-cm absorption ( $N(\text{H I}) (C_f/T_s) \sim 5.5 \times 10^{19} \text{ cm}^{-2} \text{ K}^{-1}$ ) at  $z = 0.2$  towards the pair J205449.61+004153.0/J205449.64+004149.8 (see Fig. F3). Such a strong H I 21-cm absorption is rare and usually seen in merging galaxy pairs (Srianand et al. 2015). Details of H I 21-cm absorption towards this system will be presented in a future work.

The summary of all the sources observed by us, split into primary, supplementary and miscellaneous samples as described above, are provided in Table 1. This table also gives the number of radio sightlines probed and H I 21-cm absorption detected in each category. The properties of all the sources observed by us are provided in Table A1 and discussed in Section 2.3.

## 2.2 Literature Sample

In order to interpret the nature of H I 21-cm absorbers around low- $z$  galaxies, we combine the H I 21-cm measurements of our primary sample with those of QGPs from literature. Since the existing studies of QGPs in literature have been carried out with various selection techniques and sensitivities, we define here a sample of QGPs searched for H I 21-cm absorption in literature that is relevant for our analyses and consistent with the definition of our primary sam-

**Table 1.** Summary of different samples discussed in this work.

Sample	No. of galaxies	No. of radio sightlines	H I 21-cm detections
Total Observed	55	62	9
Primary	40	45 (7*)	7 (0*)
Supplementary	10	12	0
Miscellaneous	5	5	2
Literature	24	24 (3*)	9 (3*)
Combined (Primary + Literature)	64	69 (10*)	16 (3*)

\* Number of radio sources without spectroscopic redshifts albeit having identified optical/infrared counterparts.

ple. We consider the literature measurements from the compilation presented in Table 5 of Gupta et al. (2010), as well as more recent measurements from Borthakur et al. (2011, 2014); Borthakur (2016); Zwaan et al. (2015); Reeves et al. (2015, 2016), subject to the following conditions. (i) We consider only systems selected on the basis of presence of a radio sightline near the galaxy, without any prior detection of absorption lines in the quasar’s optical/UV spectra. This is to obtain an unbiased estimate of the covering factor of H I 21-cm absorbers around low- $z$  galaxies (see Section 5). (ii) Most of the H I 21-cm measurements obtained in the literature are less sensitive than ours. Hence, in order to have uniform optical depth sensitivity across all the measurements, we include only measurements of H I 21-cm non-detections in literature with  $\int \tau dv_{10}^{3\sigma} \leq 0.3 \text{ km s}^{-1}$  (see Section 3.2). (iii) We restrict to measurements which are at impact parameters  $\lesssim 30 \text{ kpc}$ . (iv) We exclude measurements towards associated systems, or where  $z_{\text{rad}}$  is within  $\sim 200 \text{ km s}^{-1}$  of  $z_{\text{gal}}$ . (v) We exclude radio sources without optical and/or infrared counterparts and hence whose redshifts cannot be constrained. (vi) In case of low spatial resolution single dish measurements of Borthakur (2016), we do not consider the H I 21-cm non-detections with H I 21-cm emission detected in the spectrum, as the absorption could be filled-in by the emission (see e.g. Borthakur et al. 2011).

The details of the literature sample so defined are presented in Table B1. Note that seven of the QGPs in the SDSS parent sample are part of the sample of Borthakur et al. (2010, 2014); Borthakur (2016). We observed three of these QGPs, while the other four are part of the literature sample. All except three of the background radio sources in the literature sample are classified as quasars based on their optical spectra. For one of the radio sources only photometric redshift is available and two others no redshifts are available. We include these sources in the sample since their optical and infrared counterparts are present and H I 21-cm absorption have been detected towards them. We discuss in Section 5 the effects of excluding these sources in the statistical analyses. In total there are 24 QGPs in the literature sample, out of which H I 21-cm absorption have been detected in 9 cases (see Table 1). We refer to our primary sample plus the literature sample as the “Combined sample”.

## 2.3 Sample Properties

In this section, we discuss various properties of the primary and literature samples as listed in Tables A1 and B1, respectively.

(i) *Nature of background radio sources*: As mentioned in Section 2.1, the optical counterparts of all except seven radio sources in the primary sample have spectroscopic redshifts available from SDSS, NASA/IPAC Extragalactic Database (NED), or our IGO ob-

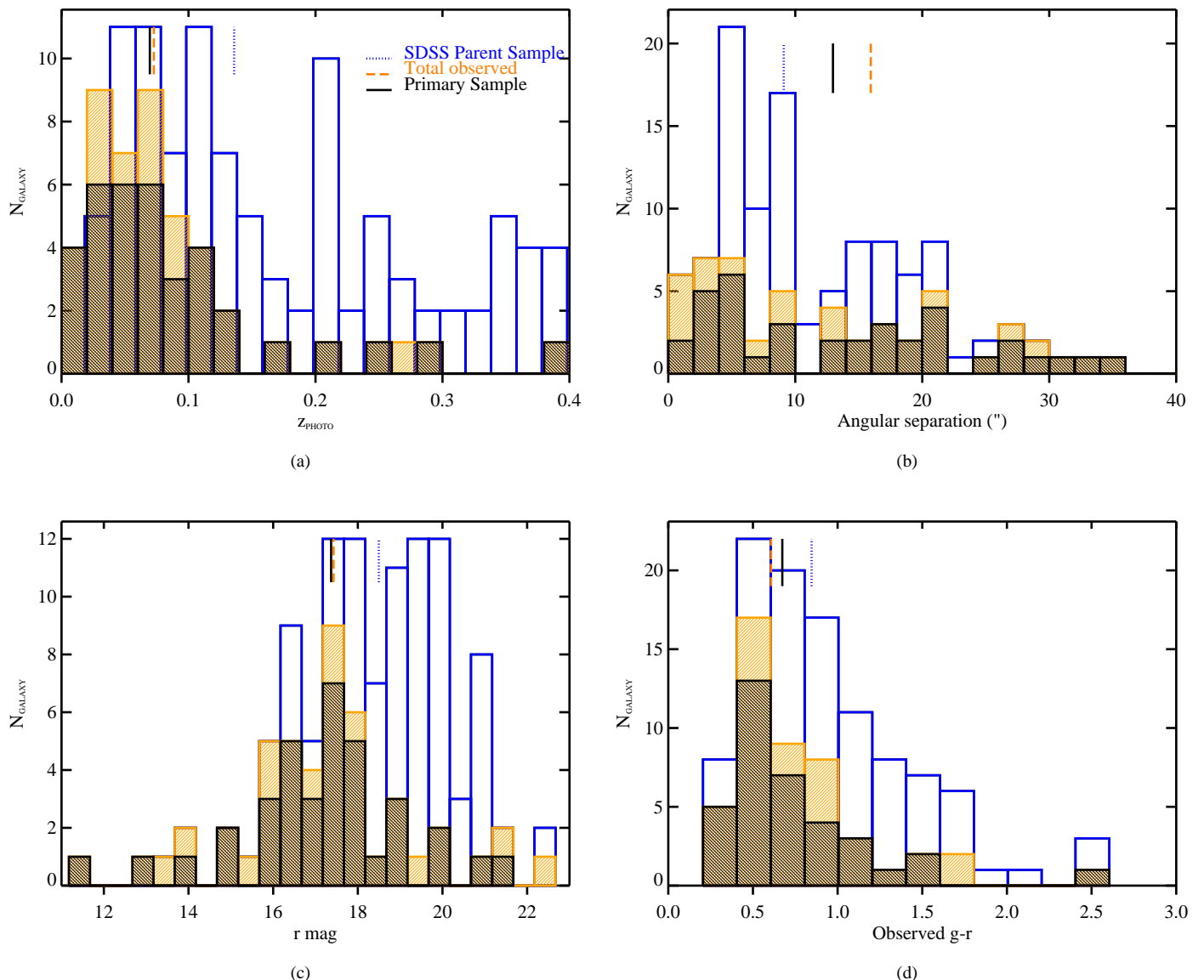


**Figure 1.** Distributions of: (a) the photometric redshift, (b) angular separation from the background radio source, (c)  $r$ -band magnitude, and (d) the observed  $g - r$  colour of the galaxies in the SDSS parent sample are shown in open blue histograms. The shaded orange histograms (with hashes at  $45^\circ$ ) are for the galaxies searched for H I 21-cm absorption by us, and the shaded black histograms (with hashes at  $135^\circ$ ) are for those that are in the primary sample. The median values of the parameters for the parent sample, the observed sample (primary + supplementary + miscellaneous) and the primary sample are marked by dotted, dashed and solid ticks, respectively, in each plot. Note that the angular separation from the background radio source of the three  $z \lesssim 0.01$  galaxies ( $70''$ ,  $220''$ ,  $320''$ ) are not shown in panel (b).

servations. The ones without spectroscopic redshifts are taken as background sources based on their SDSS and WISE photometry. All the radio sources with spectroscopic redshifts available are classified as quasars based on their optical spectra. For the rest either no classification is available or classification based on photometry indicates that they are radio galaxies. We provide the optical classification from literature and morphology of the radio sources based on their FIRST images in Table A1. Of the 38 background radio sources in our primary sample, 28 are compact, 7 are resolved and 3 show double peaks in the FIRST images (quasars with deconvolved sizes  $\leq 2''$  are classified as compact; White et al. 1997). The three sources which are double in the FIRST images are resolved into a central core (cospatial with the optical core) and two lobes in

our GMRT images. In total there are 45 radio sightlines (with peak flux density  $\geq 50$  mJy) in the primary sample.

In case of the radio sources in the literature sample, as mentioned in the previous section, all except three have spectroscopic redshifts available which classify them as background quasars. For the remaining three sources, optical/infrared counterparts are present but no classification is available. Radio morphology at arc-second resolution is available for 20 of the radio sources from FIRST ( $\sim 5''$ ) or other VLA images ( $\sim 1-5''$ ) (Stanghellini et al. 1998; Reid et al. 1999; Keeney et al. 2011). Among these sources seven are resolved while rest are compact.

(ii) *Galaxy redshifts:* The spectroscopic redshifts of 21 galaxies in our primary sample are taken from SDSS, while that of five

galaxies are taken from NED (the detailed references are provided in Table A1). We measured the redshifts of two galaxies using the Apache Point Observatory (APO) 3.5-m telescope, and that of seven galaxies using SALT. The details of the APO observations are provided in Gupta et al. (2010) and that of the SALT observations are provided in the next section. There are five galaxies in our primary sample that are identified as GOTOQs based on emission in the background quasar's SDSS spectra. The galaxies in our primary sample have redshifts in the range  $0.00008 \leq z \leq 0.37$ , with a median redshift of 0.08. The distribution of galaxy redshifts as a function of impact parameter is shown in panel (a) of Fig. 2. It can be seen that galaxies in the literature sample have  $z < 0.15$  with median  $z \sim 0.03$ .

(iii) *Impact parameters:* The impact parameters ( $b$ ) are calculated based on the projected angular separation between the centre of the galaxy and the radio sightline. The GOTOQ J1443+0214 is not detected in the SDSS images even after subtracting the quasar contribution, and the galactic line emission probably originates in a low surface brightness region within 5 kpc to the quasar sightline (Gupta et al. 2013). The impact parameter for this GOTOQ is taken to be  $< 5$  kpc. The 45 radio sightlines in the primary sample probe a range of impact parameters  $\sim 5 \leq b$  (kpc)  $\leq 34$ , with a median  $b \sim 16$  kpc. From panel (a) of Fig. 2, it can be seen that the range of impact parameters (median  $b \sim 13.9$  kpc) probed by the literature sample is similar to that by the primary sample.

(iv) *Orientation:* The galaxy inclination ( $i$ ) and azimuthal orientation ( $\phi$ ) of the radio sightline with respect to the galaxy are calculated from the minor-to-major axis ratio and the position angle of the major axis of the galaxy, respectively, from SDSS-DR12  $r$ -band photometry (Alam et al. 2015). The orientation is defined as the projected angle that the radio sightline makes with the projected major axis of the galaxy, with  $\phi = 0^\circ$  for sightlines along the major axis and  $\phi = 90^\circ$  for sightlines along the minor axis. We use the parameters from the best fit between the exponential and the de Vacouleurs fit provided by SDSS and also visually verify the parameters. The errors in  $i$  range from  $\sim 2$ – $10^\circ$ . We treat galaxies with  $i < 30^\circ$  as face-on galaxies and do not estimate  $\phi$  in these cases.

For the GOTOQ, J1300–2830, we estimate  $i$  and  $\phi$  from the SDSS  $r$ -band image (after masking the quasar) based on isophotal ellipses using STSDAS package in IRAF. For the GOTOQ, J1438+1758, we estimate  $i$  and  $\phi$  from visual inspection of the SDSS  $r$ -band image, since the galaxy emission could not be well fit by ellipses. One of the galaxies in our primary sample (J1748+7005) and six of the galaxies in the literature sample are not covered in the SDSS footprint. Since these are very low- $z$  galaxies their optical photometry are present in NED and we use their  $B$ -band photometric measurements to estimate  $i$  and  $\phi$ . For the galaxy J104257.74+074751.3, we use the photometric measurements provided in Borthakur et al. (2010). Note that excluding the galaxies for which photometric measurements are not available in SDSS does not change the statistical results obtained in this work beyond the quoted statistical uncertainties.

(v) *Galaxy properties:* We estimate the absolute magnitudes of the galaxies using the *kcorrect* algorithm (v.4.2) by Blanton & Roweis (2007). Specifically, we use the IDL based *sdss\_kcorrect* routine, the SDSS-DR12 Galactic extinction corrected *asinh ugriz* model magnitudes (Alam et al. 2015), and the galaxy redshifts to obtain the  $k$ -corrections. For two of the GOTOQs (J1300+2830 and J1438+1758), we estimate the *ugriz* magnitudes from the total counts due to the galaxy (after masking the quasar and subtracting the sky contribution) within an aperture of  $1.5''$  radius in the

respective SDSS images. Recall that the GOTOQ, J1443+0214, is not detected in the SDSS images and hence photometric measurements of this galaxy are not possible. The stellar masses are obtained from the *kcorrect* output. The typical error in the SDSS magnitudes is 0.01 and the typical uncertainty in the stellar masses derived from SDSS photometry is 50% (Blanton & Roweis 2007).

The stellar masses of the galaxies in the primary sample are in the range of  $10^{7.8} - 10^{11.0} M_\odot$  with a median of  $10^{10.0} M_\odot$ , while the  $B$ -band luminosities are in the range of  $10^{8.5} - 10^{10.6} L_\odot$  with a median of  $10^{10.0} L_\odot$ . The median  $g - r$  colour is 0.58, with most of the galaxies having  $g - r < 1.0$ , except for one with  $g - r \sim 1.6$ , which is identified as a luminous red galaxy (Gupta et al. 2013). Note that the galaxies in the literature sample have lower median stellar mass ( $10^{9.0} M_\odot$ ) and  $B$ -band luminosity ( $10^{9.2} L_\odot$ ).

The distribution of the galaxy luminosities, stellar masses and colours as function of impact parameter are shown in Fig. 2. Considering the primary sample, it can be seen that at  $b < 10$  kpc, our sample consists mostly of low luminosity and low stellar mass galaxies. This is most probably because the number density of fainter and smaller galaxies is higher and hence the probability of selecting such galaxies is higher. From the same figure, we see that at  $b \geq 10$  kpc, our sample probes mostly galaxies with high luminosity and high stellar mass. It seems that we have preferentially selected the brightest and largest galaxy that is closest to the radio sightline. Hence, it is to be noted that the distributions of galaxy luminosities and stellar masses as function of impact parameter are not uniform by construct of our sample. On the other hand, these distributions are more uniform for the literature sample, which probes more low luminosity and low stellar mass galaxies at  $b \geq 10$  kpc than our primary sample.

The SDSS local galaxies show a bimodal colour distribution, i.e. they fall on either the blue or the red sequence. To check how our galaxies compare with the general galaxy population at similar redshifts, we used a magnitude-dependent colour cut,  $^{0.1}(g - r) = 0.80 - 0.30(^{0.1}M_r + 20)$  (Blanton & Berlind 2007). Here  $^{0.1}M_r$  indicates the absolute magnitude in the  $r$ -band  $k$ -corrected to  $z = 0.1$ . We find that  $\sim 70\%$  of the galaxies in the primary sample are blue and rest are red, as also indicated by panel (d) of Fig. 1, and this holds on combining our primary sample with the literature sample.

In the following section, we present the details of our optical and radio observations.

### 3 OBSERVATIONS AND DATA REDUCTION

#### 3.1 Optical Observations

We obtained the optical spectra of seven galaxies in our sample using the Robert Stobie Spectrograph (RSS) on SALT in long-slit mode, under the programs 2013-2-IUCAA-001, 2014-1-IUCAA-001, 2014-2-SCI-017 (PI: Dutta). The observations were carried out with a  $1.''5$  slit and the PG0900 grating (resolution of  $\sim 5 \text{ \AA}$  at 5000  $\text{\AA}$ ). The slit positions were chosen to align both the galaxy and the quasar in the slit. Each pair was observed for a total  $\sim 4800$  sec, split into two blocks with spectral coverage of  $\sim 4000$ – $7000 \text{ \AA}$  and  $\sim 5000$ – $8000 \text{ \AA}$ . The wavelength ranges were chosen to maximize the coverage of the expected wavelength ranges of the  $H\alpha$ ,  $H\beta$  and  $OIII$  emission lines and the  $CaII$  absorption lines (within the photometric redshift errors). We used data reduced by the SALT

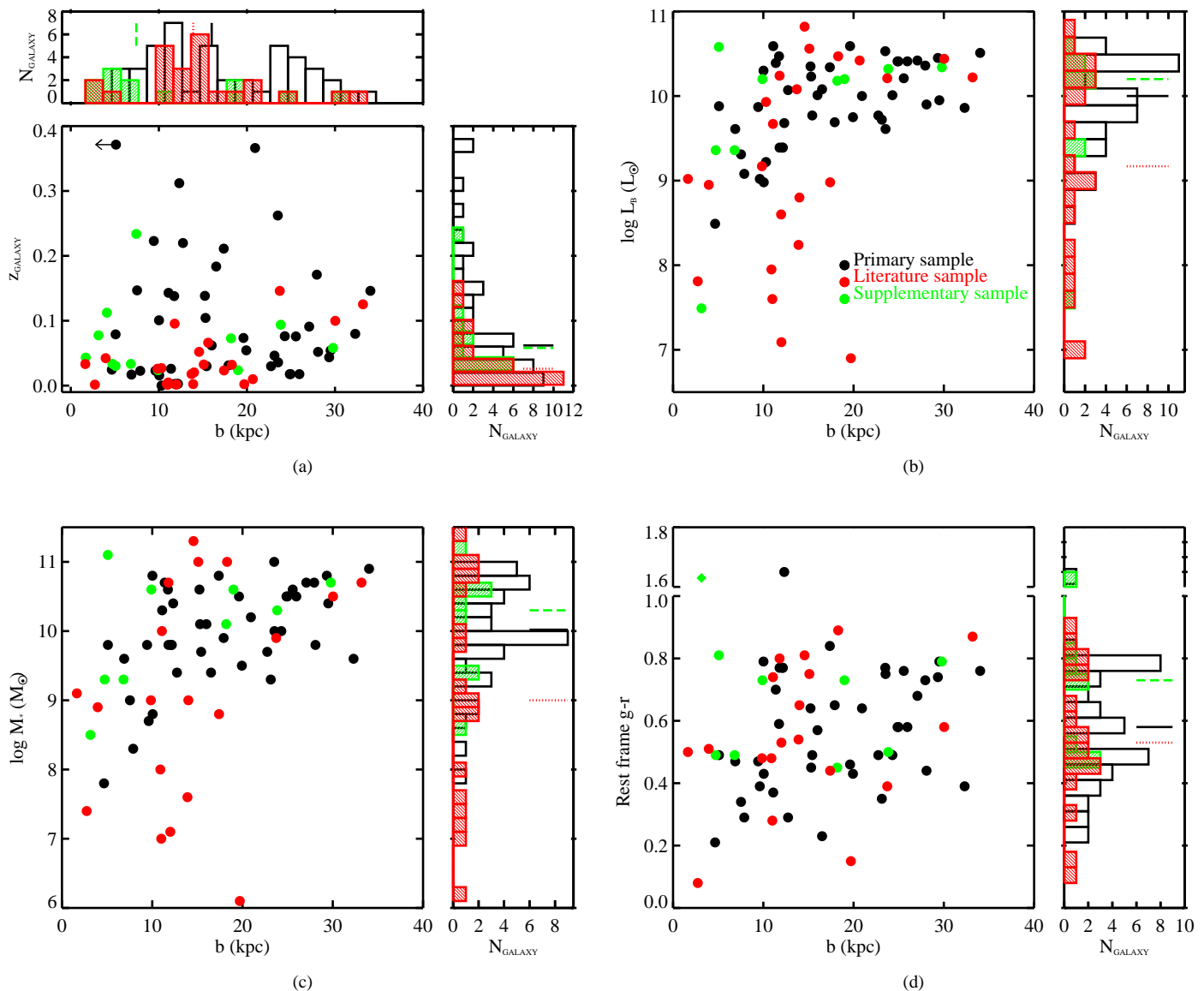


**Figure 2.** The distributions of: (a) galaxy redshifts, (b)  $B$ -band luminosity, (c) stellar mass, and (d) rest-frame SDSS  $g - r$  colour as a function of impact parameter. The black, red and green circles are for the galaxies in the primary, literature and supplementary samples, respectively. The histograms of the impact parameters, galaxy redshifts, luminosities, stellar masses and colours are also shown next to the plots, following the same colour convention. The solid, dotted and dashed ticks mark the median of the distributions for the primary, literature and supplementary samples, respectively.

science pipeline (Crawford et al. 2010), i.e. PYSALT<sup>1</sup> tasks were used to prepare the image headers for the pipeline, apply CCD amplifier gain and crosstalk corrections, subtract bias frames and create mosaic images. We subsequently flat-fielded the data, applied a wavelength solution using arc lamp spectra, performed cosmic ray removal, applied background subtraction, combined the two-dimensional spectra and extracted the one-dimensional spectra using standard IRAF tasks<sup>2</sup>. The emission and/or absorption lines

used to determine the galaxy redshifts and the galaxy spectra are given in Appendix C.

### 3.2 Radio Observations

Of the 55 sources that were searched for H I 21-cm absorption by us, 50 were observed with the GMRT, two with the VLA, two with the WSRT, and one was observed with both the GMRT and the WSRT. The GMRT observations were carried out using the L-band receiver. Prior to 2011 the sources were observed using the 2 MHz baseband bandwidth split into 128 channels (spectral resolution  $\sim 4 \text{ km s}^{-1}$  per channel, velocity coverage  $\sim 500 \text{ km s}^{-1}$ ). The later observations were carried out using the 4.17 MHz baseband bandwidth split into 512 frequency channels (spectral resolution  $\sim 2 \text{ km s}^{-1}$  per channel, velocity coverage  $\sim 1000 \text{ km s}^{-1}$ ).

<sup>1</sup> PYSALT user package is the primary reduction and analysis software tools for the SALT telescope (<http://pysalt.salt.ac.za/>).

<sup>2</sup> IRAF is distributed by the National Optical Astronomy Observatories, which are operated by the Association of Universities for Research in Astronomy, Inc., under cooperative agreement with the National Science Foundation.



The VLA observations (Proposal ID: 15A–176) were carried out in A-configuration (maximum baseline of 36.4 km) using a single 8 MHz sub-band in dual polarization split into 4096 channels (spectral resolution  $\sim 0.5 \text{ km s}^{-1}$  per channel, velocity coverage  $\sim 2000 \text{ km s}^{-1}$ ). In the case of WSRT observations a total bandwidth of 10 MHz split into 2048 spectral channels was used to acquire data in the dual polarization mode. This corresponds to a total bandwidth of  $\sim 2400 \text{ km s}^{-1}$  and a channel width of  $\sim 1.2 \text{ km s}^{-1}$  before Hanning smoothing.

In all the observations, the pointing centre was at the quasar coordinates and the band was centred at the redshifted H I 21-cm frequency estimated from the galaxy redshifts. Data were acquired in the two linear polarization products, XX and YY (circular polarization products, RR and LL, in the case of the VLA). Standard calibrators were regularly observed during the observations for flux density, bandpass, and phase calibrations (no phase calibrators were observed for WSRT observations). The details of the radio observations of the sources are given in Table D1.

The data were reduced using the National Radio Astronomy Observatory (NRAO) Astronomical Image Processing System (AIPS) following standard procedures as outlined in Gupta et al. (2010). The results obtained from the H I 21-cm absorption line searches of the QGPs are provided in Table E1. During the course of our observations we have reported the results of H I 21-cm absorption studies of 10 sources (9 from the primary sample, Gupta et al. 2010, 2013; Srianand et al. 2013, 2015; Dutta et al. 2016). The results of our H I 21-cm absorption searches of the remaining 45 sources (31 from the primary sample) are presented for the first time in this work.

We provide the standard deviation in the optical depth at the observed spectral resolution ( $\sigma_\tau$ ), and  $3\sigma$  upper limit on the integrated optical depth from spectra smoothed to  $10 \text{ km s}^{-1}$  ( $\int \tau dv_{10}^{3\sigma}$ ). In case of H I 21-cm absorption detections, we also provide the peak optical depth ( $\tau_p$ ) and the total integrated optical depth ( $\int \tau dv$ ), both at the observed spectral resolution. The choice of  $10 \text{ km s}^{-1}$  for estimating the optical depth sensitivity is motivated by the fact that the median Gaussian full-width-at-half-maximum (FWHM) of all the detected H I 21-cm absorption components in the primary sample is  $\sim 10 \text{ km s}^{-1}$ . The H I 21-cm absorption spectra in the primary sample have  $\int \tau dv_{10}^{3\sigma}$  in the range  $0.015\text{--}0.380 \text{ km s}^{-1}$ , with median of  $0.131 \text{ km s}^{-1}$  and 90% have  $\int \tau dv_{10}^{3\sigma} \leq 0.3 \text{ km s}^{-1}$ . Note that the H I 21-cm measurements in our primary sample have increased the existing number of sensitive (i.e.  $\int \tau dv_{10}^{3\sigma} \leq 0.3 \text{ km s}^{-1}$ ) H I 21-cm optical depth measurements of QGPs by a factor of  $\sim 3$ .

The H I 21-cm absorption spectra of the QGPs and the radio continuum contours of the radio sources overlaid on the optical images of the galaxies are provided in the online version, in Appendix F and Appendix G, respectively. The typical spatial resolution of the GMRT images is  $\sim 2\text{--}3$  arcsec, while that of the VLA images is  $\sim 1\text{--}2$  arcsec, and that of the WSRT images is  $\sim 20$  arcsec (see Table D1).

#### 4 INDIVIDUAL SYSTEMS

We have detected H I 21-cm absorption from seven QGPs in our primary sample. Five of these have been reported in Gupta et al. (2010, 2013); Srianand et al. (2013); Dutta et al. (2016). In this work we report two new H I 21-cm absorption detections from the QGPs, J1243+4043 and J1438+1758. We discuss the physical conditions in the QGP, J1438+1758, in Section 4.1. Detailed

study of the QGP, J1243+4043, including Global Very Long Baseline Interferometry H I 21-cm absorption spectra and optical long-slit spectra, will be presented in a future work. In Section 4.2, we discuss the implications of our measurements of the QGP, J1243+1622, from which Schneider & Corbelli (1993) have reported tentative H I 21-cm absorption. In Sections 4.3 and 4.4, we discuss about two QGPs, J1300+2830 and J1551+0713, respectively. These two are intriguing since these are the only QGPs in our sample where the quasar sightlines appear to pass through the optical disc of the galaxies in the SDSS images, but no significant H I 21-cm absorption is detected towards them (though tentative absorption features are present). Readers interested in only the statistical results may go directly to Section 5.

##### 4.1 QGP J1438+1758

The QGP J1438+1758 is a GOTOQ, i.e. the foreground galaxy was identified by us from emission lines in the SDSS spectrum of the background quasar. The foreground galaxy, located  $\sim 3''$  ( $b = 7.5$  kpc) south of the quasar (see panel (a) of Fig. 3), is not identified as a separate photometric object in SDSS. A narrow H  $\alpha$  emission line is seen at  $z_{\text{gal}} = 0.1468$  in both the SDSS-DR7 and the SDSS-Baryon Oscillation Spectroscopic Survey (BOSS) spectra (fibre diameters of  $3''$  and  $2''$  or  $\sim 8$  and  $\sim 5$  kpc at  $z_{\text{gal}}$ , respectively), with the line strength being a factor of  $\sim 3$  weaker in the SDSS-BOSS spectrum than in the SDSS-DR7 spectrum. From Gaussian fit to the H  $\alpha$  emission (see panel (a) of Fig. 4), we obtain  $z_{\text{gal}} = 0.1468 \pm 0.0001$ . From the SDSS-DR7 spectrum, we measure flux of the H  $\alpha$  line as,  $F(\text{H}\alpha) = (12.6 \pm 2.8) \times 10^{-17} \text{ erg s}^{-1} \text{ cm}^{-2}$ . This gives the dust-uncorrected luminosity of  $L(\text{H}\alpha) = (7.3 \pm 1.6) \times 10^{39} \text{ erg s}^{-1}$ . Following Argence & Lamareille (2009), we estimate the total star formation rate (SFR) in the portion of the galaxy covered by the SDSS fibre as  $0.03 \pm 0.01 M_\odot \text{ yr}^{-1}$  (uncorrected for dust attenuation and fibre filling factor). For the SDSS fibre size, this leads to an average surface density of the SFR ( $\Sigma_{\text{SFR}}$ ) of  $0.0006 M_\odot \text{ yr}^{-1} \text{ kpc}^{-2}$ , for unit fibre filling factor. We also detect weak [O II] emission in the SDSS-DR7 spectrum and measure  $L([\text{O II}] \lambda 3727) = (6.9 \pm 2.5) \times 10^{39} \text{ erg s}^{-1}$  (uncorrected for dust). This gives the SFR as  $0.05 \pm 0.02 M_\odot \text{ yr}^{-1}$  following Kewley et al. (2004), consistent with the SFR obtained from H  $\alpha$ .

The SFR obtained above is well below the median SFR ( $\sim 2 M_\odot \text{ yr}^{-1}$ ) of [O III]-selected Mg II absorbers at  $0.4 < z < 0.7$  (Noterdaeme et al. 2010). The  $\Sigma_{\text{SFR}}$  is an order of magnitude smaller compared to that measured in  $z < 0.4$  galaxies which show H I 21-cm absorption (see Table 3 of Gupta et al. 2013), as well as that inferred for the CNM in  $z > 2$  DLAs by Wolfe et al. (2003) using C II\*. Hence, the quasar sightline seems to be probing the outer, low star-forming disc of the galaxy. If we assume that the Kennicutt-Schmidt law is obeyed in the outer disc of the galaxy, then we get  $\log N(\text{H I}) = 20.3$  (Kennicutt 1998a,b). However, if the star formation efficiency in the outer disc is much lower than that predicted by the Kennicutt-Schmidt law (see e.g. Bigiel et al. 2010; Rafelski et al. 2011; Elmegreen & Hunter 2015), the  $N(\text{H I})$  will be higher.

We estimate the dust optical depth in the systematic  $V$  band of the galaxy ( $\tau_V$ ) and the colour excess ( $E(B - V)$ ) along the quasar sightline by fitting the quasar spectral energy distribution (SED) using the SDSS composite quasar spectrum (Vanden Berk et al. 2001), reddened by the Milky Way, LMC and SMC extinction curves (see Srianand et al. 2008, 2013; Noterdaeme et al. 2009, 2010, for the detailed procedure). The best-fitting ( $\chi^2_\nu \sim 1.3$ ) Milky Way extinction curve gives  $A_V = 0.10 \pm 0.01$  (where  $A_V$



$= 1.086\tau_V$ ). The errors quoted are mainly statistical. We applied the same procedure to a control sample of 159 SDSS non-BAL quasars within  $\Delta z = \pm 0.01$  of  $z_{\text{rad}}$  and  $\Delta r_{\text{mag}} = \pm 2.0$  of  $r_{\text{mag}}$  of the quasar and with  $\text{SNR} \geq 10$ . The resulting distribution of  $A_V$  has median value of 0.06 and rms of 0.24. This rms reflects a typical systematic error in the SED-fitting method due to the dispersion of the unreddened quasar SED. Hence, the quasar sightline does not show any significant evidence of reddening. If we assume  $R_V = 3.1$  as seen in the Milky Way, then  $E(B - V) = 0.03$ , which is much lower than what is measured in high- $z$  dusty Mg II and CO systems with 2175 Å dust absorption bump (Srianand et al. 2008; Noterdaeme et al. 2009; Jiang et al. 2011) as well as in low- $z$  galaxies with H I 21-cm absorption (Gupta et al. 2010, 2013; Srianand et al. 2013). The small value of extinction is more in line with the values generally seen towards intervening DLAs, Mg II and Ca II systems (York et al. 2006; Khare et al. 2012; Sardane et al. 2015). Using the observed relation between  $A_V$  and  $N(\text{H I})$  in the Milky Way (Bohlin et al. 1978), we get  $\log N(\text{H I}) = 20.2$  ( $1/\kappa$ ), where  $\kappa$  is the ratio of dust-to-gas ratio in the absorption system to that in the Milky Way.

Both the SDSS-DR7 and the SDSS-BOSS spectra of the quasar show Ca II and Na I absorption lines at the redshifted wavelengths expected for the foreground galaxy (see panels (b) and (c) of Fig. 4). We use the higher SNR SDSS-BOSS spectrum to obtain the rest equivalent widths of the Ca II  $\lambda 3934$  and the Na I  $\lambda 5891$  lines as  $0.22 \pm 0.05$  Å and  $0.27 \pm 0.09$  Å, respectively. The rest equivalent width of Ca II  $\lambda 3934$  measured here is consistent with the weak Ca II absorber population proposed by Sardane et al. (2015), which were shown to have an abundance pattern typical of halo gas with less depletion of the refractory elements and a typical  $E(B - V) \sim 0.01$ . Using the empirical relation between  $E(B - V)$  and rest equivalent width of Na I obtained by Poznanski et al. (2012), we estimate  $E(B - V) = 0.05^{+0.05}_{-0.03}$ , consistent within uncertainties with the value obtained from SED fitting.

We detect H I 21-cm absorption towards the background quasar at the redshift of the galaxy. The H I 21-cm absorption profile is best fit with two Gaussian components, (i.e.  $\chi^2_\nu = 1.2$  for double Gaussian fit compared to  $\chi^2_\nu = 2.0$  for single Gaussian fit), A and B, separated by  $\sim 13$  km s $^{-1}$ . The fit to the absorption is shown in panel (b) of Fig. 3, and the details of the fit are provided in Table 2. The velocity offset between the H I 21-cm absorption components and the redshift estimated from the H  $\alpha$  emission is well within the redshift measurement error. The total integrated optical depth of the H I 21-cm absorption is  $4.89 \pm 0.19$  km s $^{-1}$  which yields  $N(\text{H I}) (C_f/T_s) = (8.9 \pm 0.4) \times 10^{18}$  cm $^{-2}$  K $^{-1}$ . 90% of the total optical depth is contained within 20 km s $^{-1}$ . Our GMRT image of the background radio source (panel (a) of Fig. 3) shows that it is compact with a flux density of 53 mJy, consistent with that obtained by FIRST. High-resolution (sub-arcsecond-scale) map is not available for this source, and hence  $C_f$  is uncertain. For  $C_f = 1$  and a typical CNM mean temperature of 100 K, as observed in the Milky Way (Heiles & Troland 2003),  $\log N(\text{H I}) = 20.95 \pm 0.02$ . Comparing this with the  $N(\text{H I})$  obtained from SED fitting above gives  $\kappa = 0.2$ , consistent with the absorption arising from cold gas in the outer disk of the galaxy, where the dust-to-gas ratio is expected to be lower.

## 4.2 QGP J1243+1622

The QGP J1243+1622 (also known as 3C 275.1/NGC 4651;  $z_{\text{rad}} = 0.56$ ;  $z_{\text{gal}} = 0.0026$ ) has been studied in H I 21-cm absorption and

**Table 2.** Details of the Gaussian fit to the 21-cm absorption line detected towards J1438+1758.

ID	$z_{\text{abs}}$	FWHM (km s $^{-1}$ )	$\tau_p$	$T_k$ (K)	$N(\text{H I}) (C_f/T_s)$ ( $10^{19}$ cm $^{-2}$ K $^{-1}$ )
(1)	(2)	(3)	(4)	(5)	(6)
A	0.14677	$12 \pm 1$	$0.33 \pm 0.02$	$< 3150$	$0.76 \pm 0.11$
B	0.14682	$7 \pm 1$	$0.15 \pm 0.03$	$< 1070$	$0.20 \pm 0.07$

Column 1: Absorption component identification. Column 2: Redshift of absorption component. Column 3: Full width at half maximum (FWHM; km s $^{-1}$ ). Column 4: Peak optical depth. Column 5: Upper limit on the gas kinetic temperature ( $T_k$ ; K), obtained assuming the line width is purely due to thermal motions. Column 6:  $N(\text{H I})$  in terms of the covering factor,  $C_f$ , and the spin temperature,  $T_s$ , in units of  $10^{19}$  cm $^{-2}$  K $^{-1}$ .

emission by Corbelli & Schneider (1990); Schneider & Corbelli (1993). A tentative H I 21-cm absorption feature, with peak optical depth of  $0.0067 \pm 0.0012$ , was found in their VLA C-configuration observations at heliocentric velocity 643 km s $^{-1}$ . In their subsequent VLA B-configuration observations, the radio source (3C 275.1) resolves into two components. However, the absorption feature appeared weaker in the spectra towards both these components, as well as in the spectra extracted from data smoothed to the resolution of the C-configuration. Another tentative feature was identified at heliocentric velocity 636 km s $^{-1}$ , with peak optical depth of  $0.0059 \pm 0.0016$  and integrated optical depth of 0.03 km s $^{-1}$ , towards the southern component. The authors also report H I 21-cm emission along the quasar sightline from the outer disk of NGC 4651 at the level of  $N(\text{H I}) \sim 3 \times 10^{19}$  cm $^{-2}$  from VLA D-configuration observations. Combining this with their optical depth measurement they constrain the H I gas in the outer H I disk of NGC 4651 to be warmer than  $\sim 500$  K.

The radio source resolves into a core (cospatial with the optical quasar) and two lobes separated by  $\sim 15''$  in our GMRT image (panel (c) of Fig. 3). There appears to be tentative weak absorption features (marked by ‘A’ and ‘B’ in panel (d) of Fig. 3), near the velocities of the tentative features reported by Schneider & Corbelli (1993), in the spectra towards the continuum peaks of the northern lobe and the core. However, the integrated optical depth of these features ( $0.03 \pm 0.01$  km s $^{-1}$  and  $0.04 \pm 0.02$  km s $^{-1}$  for A and B, respectively) are not significant ( $\leq 3\sigma$ ). We obtain  $\int \tau dv^{3\sigma} \leq 0.030$  km s $^{-1}$  towards the two lobes and  $\leq 0.060$  km s $^{-1}$  towards the core, consistent with the measurement of Schneider & Corbelli (1993). All three radio sightlines are at  $b \sim 12$  kpc from NGC 4651. Chung et al. (2009) have estimated the isophotal H I diameter (where the azimuthally averaged H I surface density falls to  $1 M_\odot \text{pc}^{-2}$ ) and the effective H I diameter (encompassing 50% of the total flux) of NGC 4651 to be 30.3 kpc and 15.6 kpc, respectively. From the high resolution and high sensitivity H I emission map of NGC 4651 presented in Chung et al. (2009), the H I distribution is asymmetric and extended to the west, i.e. away from the radio sightlines. In the opposite side of the H I tail i.e. to the north-east, a stellar tail is found in the optical images (see Fig. 3). The quasar sightlines lie just at the edge of the H I disk of NGC 4651 in this map, where  $N(\text{H I}) \leq 6 \times 10^{19}$  cm $^{-2}$ , consistent with Schneider & Corbelli (1993). It is important to note that cold gas, if present in the outer disk of NGC 4651, could be clumpy and the  $N(\text{H I})$  obtained from H I emission represents the average H I surface density in that region. The H I 21-cm optical depth sensitivity achieved in this case will be good enough to detect  $T_s \sim 100$  K gas for  $N(\text{H I}) = 10^{19}$  cm $^{-2}$  when  $C_f = 1$ . The lack of H I 21-cm ab-

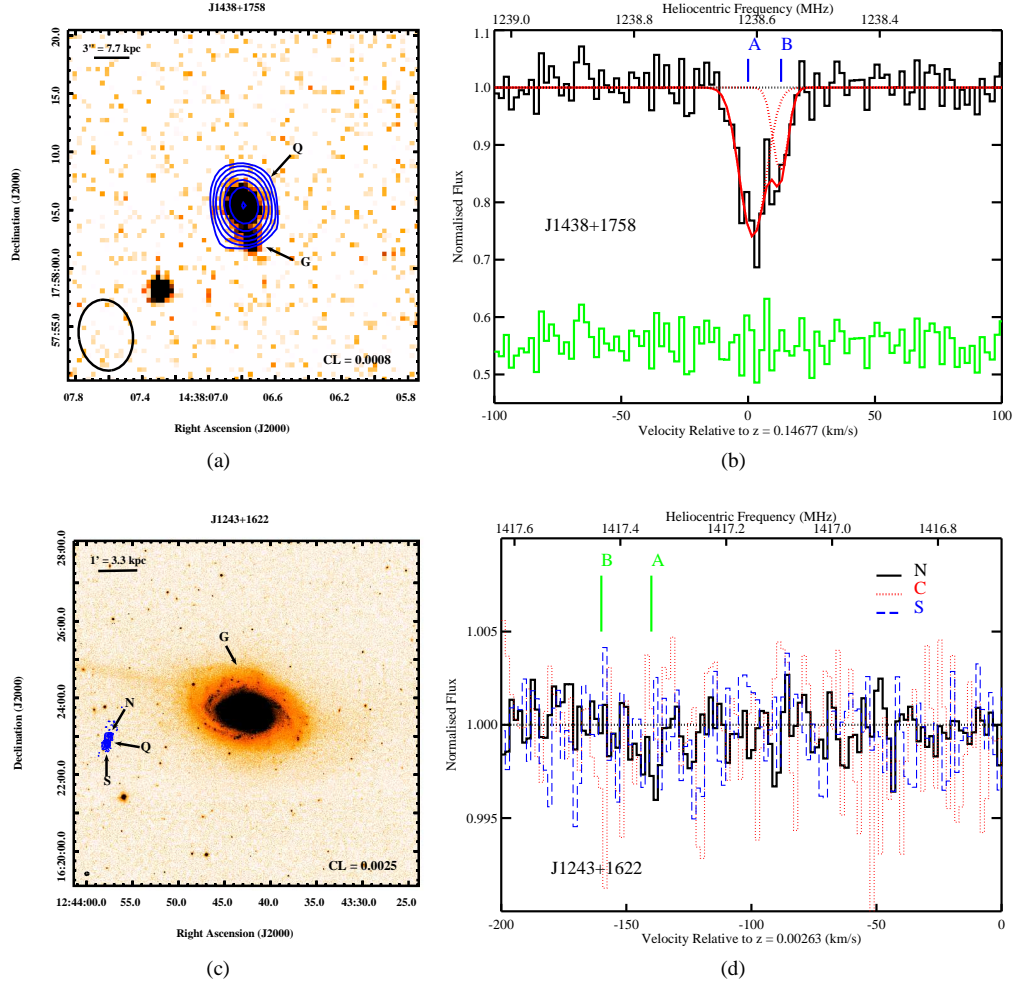


**Figure 3.** *Left:* SDSS *r*-band images overlaid with the 1.4 GHz continuum contours of the QGPs (a) J1438+1758 and (c) J1243+1622. In each image the quasar is marked by ‘Q’ and the galaxy is marked by ‘G’. In case of J1243+1622 the north and south lobes are marked by ‘N’ and ‘S’, respectively. The restoring beam of the continuum map is shown at the bottom left corner. The spatial scale is indicated at the top left corner. The contour levels are plotted as  $CL \times (-1, 1, 2, 4, 8, \dots)$  Jy beam $^{-1}$ , where CL is given in the bottom right of each image. The rms in the images (a) and (b) are 0.2 and 0.5 mJy beam $^{-1}$ , respectively. *Right:* 21-cm absorption spectra towards (b) J1438+1758 and (d) J1243+1622. In case of J1438+1758, individual Gaussian components and the resultant fits to the absorption profile are plotted as dotted and continuous lines, respectively. Residuals, shifted by an arbitrary offset for clarity, are also shown. Locations of the peak optical depth of the individual components are marked by vertical ticks. In case of J1243+1622, the H I 21-cm absorption spectra towards the core and southern lobe are overlotted on the spectrum towards the northern lobe (solid line), in dotted and dashed lines, respectively. Locations of the weak tentative absorption features suggested by Schneider & Corbelli (1993) are marked by vertical lines. We do see weak albeit statistically insignificant ( $\leq 3\sigma$ ) features at these locations even in our spectra.

sorption is consistent with either  $N(\text{H I})$  being very small or  $T_s/C_f \gtrsim 550$  K towards the core and  $\gtrsim 1100$  K towards the two lobes if we assume  $N(\text{H I}) = 6 \times 10^{19} \text{ cm}^{-2}$  as seen in the outer regions of the emission map.

### 4.3 QGP J1300+2830

The QGP, J1300+2830, is a GOTOQ with the foreground galaxy located  $\sim 3''$  ( $b = 9.4$  kpc) north-east of the quasar ( $z_{\text{rad}} = 0.65$ ) in the SDSS image (see panel (a) of Fig. 5). A narrow  $\text{H}\alpha$  emission line from the foreground galaxy is detected on top of the broad  $\text{H}\beta$  emission from the background quasar in the SDSS spectrum. From Gaussian fit to the  $\text{H}\alpha$  emission line, we obtain  $z_{\text{gal}} = 0.2229 \pm 0.0001$  and  $F(\text{H}\alpha) = (23.52 \pm 6.47) \times 10^{-17} \text{ erg s}^{-1} \text{ cm}^{-2}$  (see panel (a) of Fig. 6). This leads to a dust-uncorrected luminosity

of  $L(\text{H}\alpha) = (3.45 \pm 0.95) \times 10^{40} \text{ erg s}^{-1}$  and SFR (in the portion of the galaxy covered by the SDSS fibre) =  $0.14 \text{ M}_{\odot} \text{ yr}^{-1}$  (Argence & Lamareille 2009). A weak  $[\text{O III}] \lambda 5008$  emission line is also detected at a redshift consistent with the  $\text{H}\alpha$  emission, on top of  $[\text{O II}]$  emission from the quasar (see panel (b) of Fig. 6), which gives  $L([\text{O III}] \lambda 5008) = (3.44 \pm 1.06) \times 10^{40} \text{ erg s}^{-1}$  (uncorrected for dust).

The  $\Sigma_{\text{SFR}} = 0.003 \text{ M}_{\odot} \text{ yr}^{-1} \text{ kpc}^{-2}$  is comparable to the values measured in  $z < 0.4$  galaxies which show H I 21-cm absorption (see Table 3 of Gupta et al. 2013), as well as that inferred for the CNM in  $z > 2$  DLAs by Wolfe et al. (2003) using C II\*. However, we do not detect H I 21-cm absorption from this galaxy ( $\int \tau dv_{10}^{3\sigma} \leq 0.239 \text{ km s}^{-1}$ ). It is interesting to note that this is the only GOTOQ, out of the six (five in our sample and one from Borthakur et al. (2010)) that have been searched for H I 21-cm absorption, where H I 21-cm absorption has not been detected. We

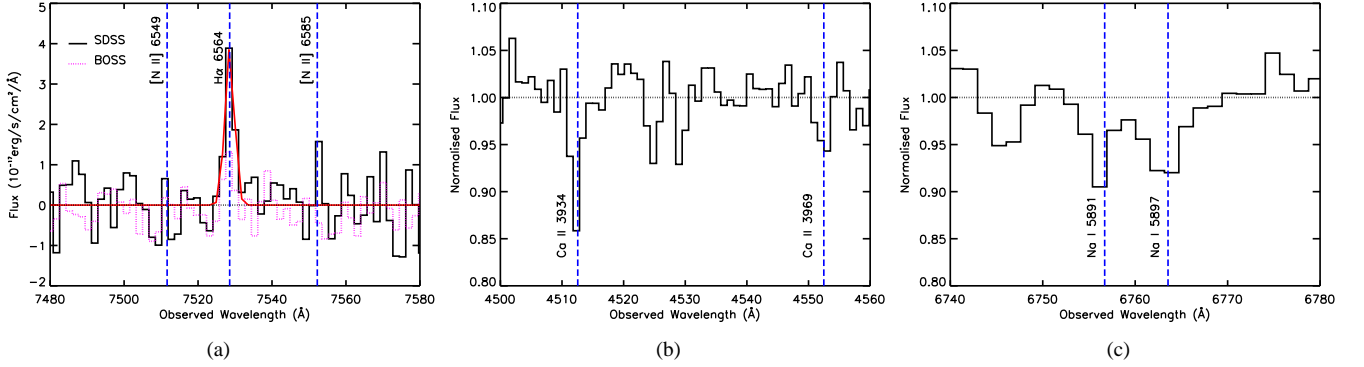


**Figure 4.** Gaussian fit to the  $H\alpha$  emission at  $z_{\text{gal}} = 0.1468$  towards J1438+1758 is overplotted on the SDSS-DR7 spectrum, after subtracting the quasar continuum, in panel (a). The SDSS-BOSS spectrum is also shown in dotted histogram for comparison. The flux normalized SDSS-BOSS spectrum towards J1438+1758 with the Ca II and Na I absorption detected at  $z_{\text{gal}} = 0.1468$ , is shown in panels (b) and (c), respectively. The vertical ticks mark the position of the  $H\alpha$  and [N II] emission lines and absorption lines of Ca II and Na I doublet.

show the VLA H I 21-cm absorption spectra smoothed to  $2 \text{ km s}^{-1}$  in panel (b) of Fig. 5. We note that a weak absorption feature ( $\int \tau dv = 0.10 \pm 0.06$ ) is observed with  $\lesssim 2\sigma$  significance at  $20 \text{ km s}^{-1}$  from the  $H\alpha$  redshift. The radio source is compact in our VLA image (panel (a) of Fig. 5) with a flux density of 119 mJy, similar to that obtained by Miller et al. (2009). No sub-arcsecond-scale map of the radio source is available at 1.4 GHz.

We measure rest equivalent width of the Ca II  $\lambda 3934$  line as  $0.43 \pm 0.06 \text{ \AA}$  (see panel (c) of Fig. 6). The presence of Ca II absorption means that there is H I gas along the quasar sightline. However, the Na I doublet is not detected and we put a  $3\sigma$  upper limit on the rest equivalent width of Na I  $\lambda 5891 \leq 0.11 \text{ \AA}$ . In the Galactic ISM,  $N(\text{Na I})/N(\text{Ca II}) > 1$  for the observed values of  $N(\text{Na I})$  (Welty et al. 1996, figure 9), while the present ratio is  $\lesssim 0.1$  assuming linear part of the curve of growth. This could mean that the gas is not arising from the dusty and dense ISM where Ca depletion is high ( $\sim -3$  dex). This is discussed further in Section 6.1.

#### 4.4 QGP J1551+0713

The QGP J1551+0713 consists of a quasar ( $z_{\text{rad}} = 0.68$ ) whose sightline appears to pass through the outer optical disc of a foreground galaxy ( $5''$  north of the galaxy's centre) in the SDSS image (see panel (c) of Fig. 5). We obtained the redshift of the galaxy,  $z_{\text{gal}} = 0.1007 \pm 0.0005$ , from our SALT long-slit spectrum. The galaxy appears to be a non-star-forming early-type galaxy. No emission lines are detected in the SALT spectrum of the galaxy, but stellar absorption from  $H\alpha$ , Ca II and Na I lines are detected (see Fig. C1), implying an old stellar population.

The radio emission from the quasar is compact in our GMRT image (panel (c) of Fig. 5) with a flux density of 68 mJy, consistent with that obtained by FIRST. No sub-arcsecond-scale image of this quasar is available. Weak tentative absorption features are detected towards this quasar (marked by 'A' and 'B' in panel (d) of Fig. 5). However they are not statistically significant ( $\leq 2.0\sigma$ ), with  $\int \tau dv = 0.10 \pm 0.06 \text{ km s}^{-1}$  and  $0.13 \pm 0.07 \text{ km s}^{-1}$  for A and B, respectively. For a typical CNM temperature of 100 K, the  $\int \tau dv_{10}^{3\sigma} \leq 0.265 \text{ km s}^{-1}$  constraint leads to  $\log N(\text{H I}) \leq 19.7$ . The H I 21-cm non-detection in this case can be due to the absence of gas along the sightline or most of the gas along the sightline being warm. The first possibility is supported by the non-detection of Ca II and Na I absorption lines at the redshift of the galaxy in the

quasar spectrum, with  $3\sigma$  upper limits on rest equivalent widths as  $0.13 \text{ \AA}$  (Ca II  $\lambda 3934$ ) and  $0.09 \text{ \AA}$  (Na I  $\lambda 5891$ ), respectively.

## 5 STATISTICAL ANALYSES

In this section we study the optical depth and covering factor of H I 21-cm absorbers around low- $z$  galaxies as function of their spatial location as well as the host galaxy properties. To estimate the covering factor of H I 21-cm absorbers ( $C_{21}$ ) we use a  $3\sigma$  optical depth sensitivity,  $\tau_0$ , i.e.  $C_{21}$  is defined as the fraction of systems showing H I 21-cm detections with  $\int \tau dv_{10}^{3\sigma} \leq \tau_0$  and  $\int \tau dv \geq \tau_0$ . As mentioned in Section 3.2,  $\sim 90\%$  of the QGPs in our primary sample have  $\int \tau dv_{10}^{3\sigma} \leq 0.3 \text{ km s}^{-1}$ , corresponding to a sensitivity of  $\log N(\text{H I}) \leq 19.7$  for  $T_s = 100 \text{ K}$  and  $C_f = 1$ . Hence, we use  $\tau_0 = 0.3 \text{ km s}^{-1}$  throughout this work, unless mentioned otherwise, to estimate  $C_{21}$ . For the statistical analyses in this section we include the measurements from our primary sample and the literature sample. In total there are 64 galaxies (69 radio sightlines) in the Combined sample, out of which H I 21-cm absorption has been detected in 16 sightlines (see Table 1). Note that for the QGPs, J1015+1637, J1606+2717 and J1748+7005, we adopt the more sensitive optical depth constraints obtained by Borthakur (2016), Borthakur et al. (2014) and Greisen et al. (2009), respectively, for the purpose of the statistical analyses here.

### 5.1 Radial profile of H I 21-cm absorbers

#### 5.1.1 Impact parameter

Left panel in Fig. 7 shows the integrated H I 21-cm optical depth as a function of impact parameter around galaxies. The filled symbols correspond to  $\int \tau dv$  of the H I 21-cm detections and the open symbols to  $\int \tau dv_{10}^{3\sigma}$  of the H I 21-cm non-detections. The black, red and green symbols are for QGPs in the primary, literature and supplementary samples, respectively. The size of the symbols represents the luminosity of the galaxies, with small size for galaxies with  $L_B \leq 10^{10} L_\odot$  and large for galaxies with  $L_B > 10^{10} L_\odot$ . Galaxies without photometric measurements are plotted with a different symbol (diamond). H I 21-cm absorption has been detected over the range  $1.7 \leq b(\text{kpc}) \leq 25$ . It can be seen from Fig. 7 that the H I 21-cm optical depth declines with increasing  $b$  albeit with a

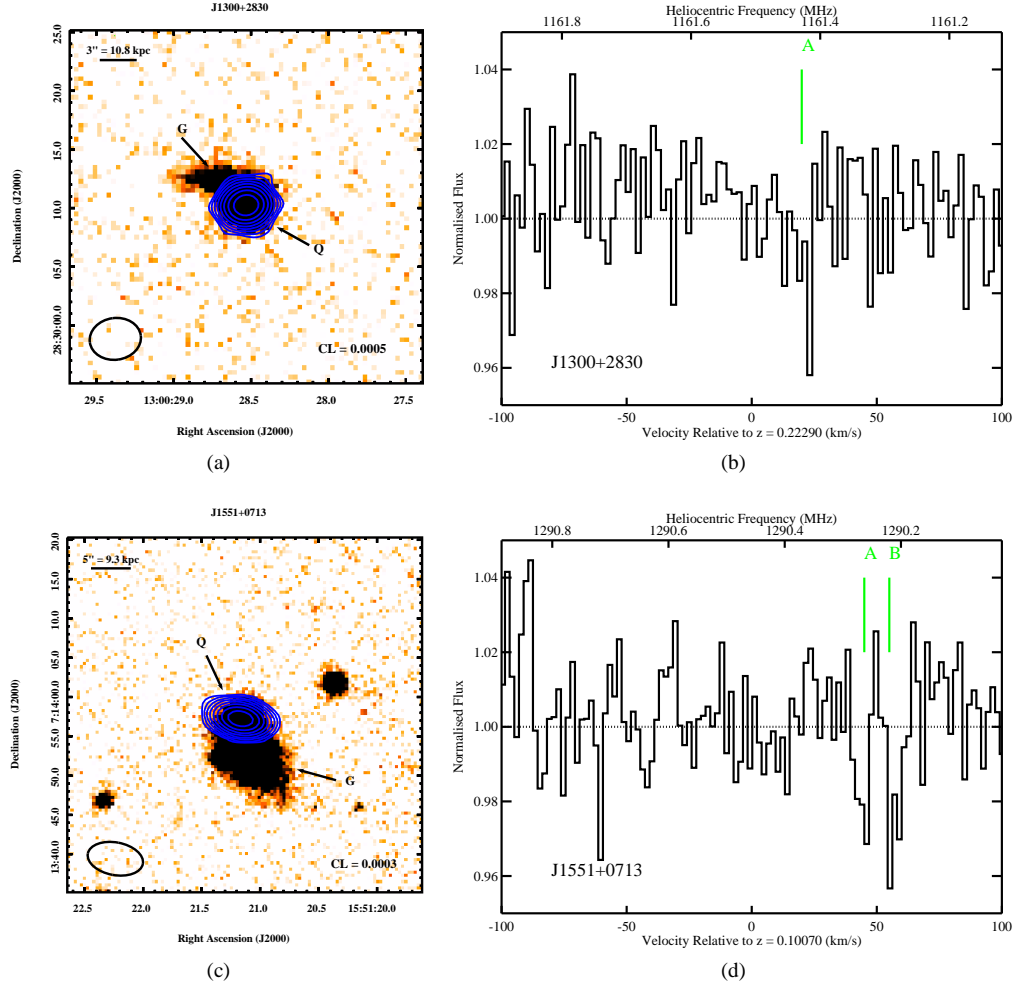


**Figure 5.** *Left:* SDSS *r*-band images overlaid with the 1.4 GHz continuum contours of the QGPs (a) J1300+2830 and (c) J1551+0713. In each image the quasar is marked by ‘Q’ and the galaxy is marked by ‘G’. The restoring beam of the continuum map is shown at the bottom left corner. The spatial scale is indicated at the top left corner. The contour levels are plotted as  $CL \times (-1, 1, 2, 4, 8, \dots)$  Jy beam $^{-1}$ , where CL is given in the bottom right of each image. The rms in the images is 0.1 mJy beam $^{-1}$ . *Right:* H I 21-cm absorption spectra towards (b) J1300+2830 and (d) J1551+0713. Locations of the weak tentative absorption features present in these spectra are identified by vertical ticks.

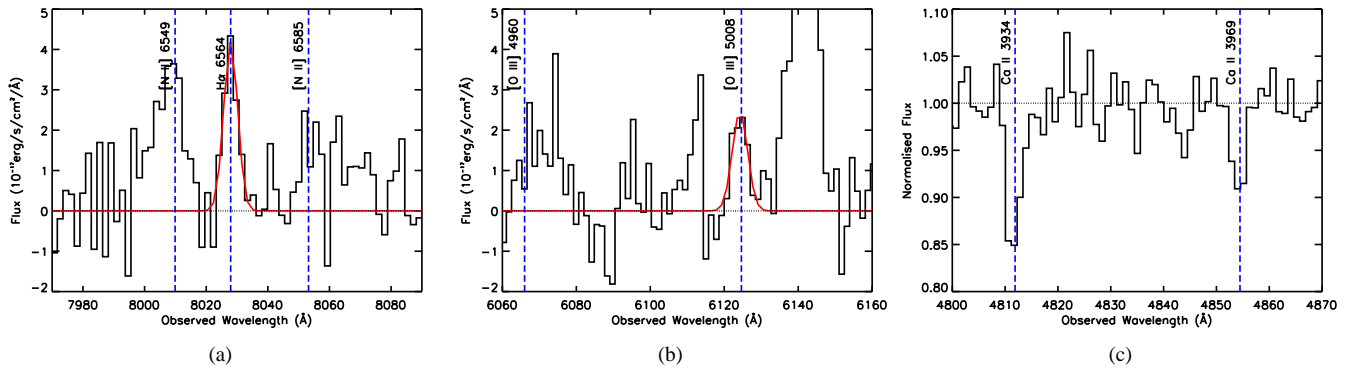


**Figure 6.** Gaussian fits to the H  $\alpha$  and [O III]  $\lambda 5008$  emission lines at  $z_{\text{gal}} = 0.2229$  towards J1300+2830 are overplotted on the SDSS spectrum, after subtracting the quasar continuum, in panels (a) and (b), respectively. The flux normalized SDSS spectrum towards J1300+2830 with the Ca II absorption detected at  $z_{\text{gal}} = 0.2229$  is shown in panel (c). The vertical ticks mark the position of the H  $\alpha$ , [N II] and [O III] emission lines and the absorption from Ca II doublet.

large scatter. As shown in figure 9 of Zwaan et al. (2015), the distribution of  $N(\text{H I})$  (derived from  $\int \tau dv$ ) with impact parameter of the low- $z$  QGPs follows the general declining trend of  $N(\text{H I})$  with galactocentric radius obtained from emission maps of local galaxies (Zwaan et al. 2005).

A weak anti-correlation between  $\int \tau dv$  of the H I 21-cm detections and  $b$  (Spearman rank correlation coefficient of  $\sim -0.3$  at a significance level of 0.81) has been reported previously by Gupta et al. (2013); Zwaan et al. (2015). Recently, Curran et al. (2016) have reported an anti-correlation using Kendall-tau test (probability of the anti-correlation arising by chance,  $P(r_k) = 9.39 \times 10^{-4}$ , which is significant at  $S(r_k) = 3.31\sigma$ ) between the H I 21-cm absorption strength and impact parameter using 90 low- $z$  H I 21-cm observations in literature and including upper limits on the H I 21-cm optical depth as censored data points. However, they do not provide the value of the correlation coefficient,  $r_k$ . We perform a survival analysis on all the measurements in the Combined sample, by including the  $3\sigma$  upper limits as censored data points. In particular, we perform Kendall's  $\tau$  correlation test using the 'cenken' function under the 'NADA' package in R to obtain  $r_k = -0.20$ ,  $P(r_k) = 0.01$ ,  $S(r_k) = 2.42\sigma$ . The results from test for correlation between  $\int \tau dv$  and various parameters are given in Table 3.

The anti-correlation obtained by us is at a lesser significance than that obtained by Curran et al. (2016). This could be due to the differences between the samples used by them and us, which we list here: (a) Our Combined sample consists of 31 new measurements from our primary sample and 7 new measurements from Borthakur (2016) that were not present in the sample of Curran et al. (2016). (b) We have considered only measurements upto  $b \sim 30$  kpc, whereas Curran et al. (2016) have considered measurements upto  $b \sim 200$  kpc. (c) From table 1 of Curran et al. (2016), we notice that for the upper limits on the integrated optical depth measurements from Borthakur et al. (2011), they have considered a line width of  $1 \text{ km s}^{-1}$ . However, for the rest of the upper limits they have considered a line width of  $10 \text{ km s}^{-1}$ . We have used a line width of  $10 \text{ km s}^{-1}$  uniformly for all upper limits in the Combined sample. (d) As per the definition of our primary sample (see Section 2.2), we have not included measurements towards radio sources without optical counterparts and measurements towards systems that were picked based on the presence of metal absorption in the quasar spectra, whereas Curran et al. (2016) have not imposed such conditions on their sample.

To check the dependence of the anti-correlation between  $\int \tau dv$  and  $b$  on galaxy properties, we divide the galaxies into two groups based on the median  $L_B = 10^{10} L_\odot$ . We find that the anti-correlation becomes stronger but not more significant considering only the low-luminosity galaxies ( $r_k = -0.26$ ,  $P(r_k) = 0.03$ ,  $S(r_k) = 2.09\sigma$ ), and weaker and less significant considering only the high-luminosity galaxies ( $r_k = -0.15$ ,  $P(r_k) = 0.20$ ,  $S(r_k) = 1.23\sigma$ ). Similar results are found when we divide the galaxies based on their stellar masses and colours, i.e. the anti-correlation is stronger for low-mass and bluer galaxies.

Coming to covering factor of H I 21-cm absorbers, top left panel of Fig. 7 shows  $C_{21}$  in two bins of  $b$  based on the median value ( $\sim 15$  kpc).  $C_{21}$  drops from  $0.24^{+0.12}_{-0.08}$  at  $b \leq 15$  kpc to  $0.06^{+0.09}_{-0.04}$  at  $b = 15-35$  kpc. The dependence of  $C_{21}$  on various parameters is given in Table 4. Next, we divide galaxies in each impact parameter bin based on their luminosity into high and low luminosity groups. It can be seen from the above figure that  $C_{21}$  shows declining trend with  $b$  for both luminosity groups. We also find that  $C_{21}$  shows similar declining trend with  $b$  when we divide

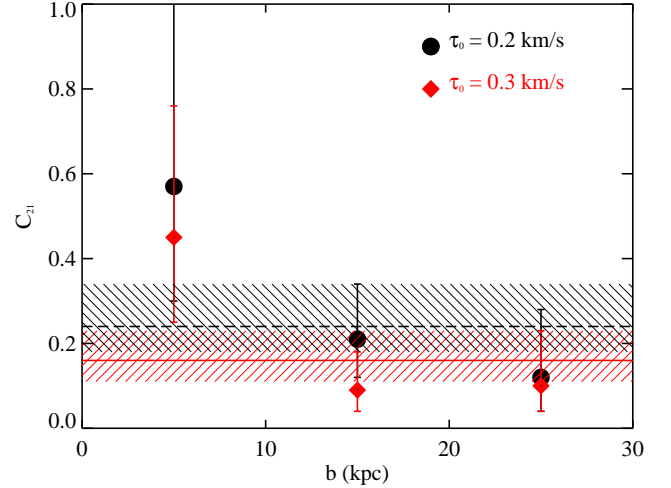


**Figure 8.** The covering factor of H I 21-cm absorbers ( $C_{21}$ ) in three different impact parameter bins (0–10, 10–20 and 20–30 kpc) for two different optical depth sensitivities,  $\tau_0 = 0.2$  and  $0.3 \text{ km s}^{-1}$ , for the combined sample. The horizontal red solid line is the mean  $C_{21}$  within 30 kpc for  $\tau_0 = 0.3 \text{ km s}^{-1}$ , while the dashed black line is for  $\tau_0 = 0.2 \text{ km s}^{-1}$ . The shaded regions mark the corresponding  $1\sigma$  errors.

galaxies based on their stellar masses and colours. The decrease of  $C_{21}$  with  $b$  is further illustrated in Fig. 8, where  $C_{21}$  is estimated for three different impact parameter bins,  $b = 0-10$ ,  $10-20$  and  $20-30$  kpc, and for two different sensitivities,  $\tau_0 = 0.2$  and  $0.3 \text{ km s}^{-1}$ . While  $C_{21}$  can be  $0.45^{+0.31}_{-0.20}$  (respectively  $0.57^{+0.45}_{-0.27}$ ) at  $b < 10$  kpc for  $\tau_0 = 0.3 \text{ km s}^{-1}$  (respectively  $0.2 \text{ km s}^{-1}$ ), the average  $C_{21}$  within  $b = 30$  kpc is  $0.16^{+0.07}_{-0.05}$  (respectively  $0.24^{+0.10}_{-0.06}$ ) for  $\tau_0 = 0.3 \text{ km s}^{-1}$  (respectively  $0.2 \text{ km s}^{-1}$ ). Note that due to the small number of detections and large  $1\sigma$  Poisson errors, the above dependence of  $C_{21}$  on  $b$  is not statistically significant.

Recall that seven radio sources in the primary sample and three radio sources in the literature sample do not have spectroscopic redshifts available, but are considered as background sources based on optical and infrared photometry (see Sections 2.1 and 2.2). We find that excluding these 10 systems does not change the anti-correlation between  $\int \tau dv$  and  $b$ . The average  $C_{21}$  within  $b = 30$  kpc ( $0.14^{+0.07}_{-0.05}$ ) and the trend of  $C_{21}$  with  $b$  also remain the same within the uncertainties. Similarly, including the sources in the supplementary sample does not change the above results within the uncertainties, with average  $C_{21} = 0.14^{+0.06}_{-0.04}$  within  $b = 30$  kpc.

### 5.1.2 Scaled impact parameter

We scale the impact parameter with an estimate of the H I radius of the galaxy based on its optical luminosity. Since H I emission cannot be mapped from all our galaxies, for the sake of uniformity we use an estimate of the probable H I size based on the correlation found between the optical B-band magnitude and H I size of spiral and irregular galaxies in the field at low redshift (Broeils & Rhee 1997; Lah et al. 2009). Using this relation we estimate the effective radius ( $R_{\text{HI}}$ ) within which half of the H I mass of the galaxy is contained. This amounts to scaling the impact parameter with the galaxy luminosity since  $R_{\text{HI}} \propto L_B^\beta$ , where  $\beta \sim 0.4$ . This is similar to the scaling relation found between optical size and luminosity



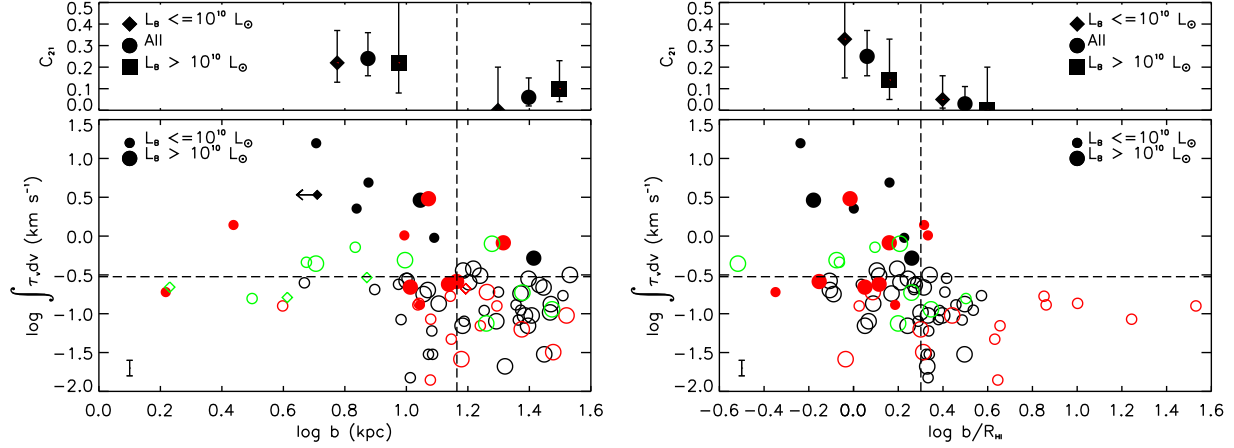


**Figure 7.** *Left:* Integrated H I 21-cm optical depth around galaxies as a function of impact parameter. The black, red and green circles are for QGPs in the primary sample, the literature sample and the supplementary sample, respectively. The solid and open circles represent  $\int \tau dv$  and  $\int \tau dv_{10}^{3\sigma}$  of the H I 21-cm detections and non-detections, respectively. The small circles are for galaxies with  $L_B \leq 10^{10} L_\odot$  while the large circles are for galaxies with  $L_B > 10^{10} L_\odot$ . Galaxies without luminosity measurements available are plotted as diamonds. The typical error in the optical depth measurements is shown at the bottom left of the plot. To the top of the plot, the covering factor of H I 21-cm absorbers (for  $\tau_0 = 0.3 \text{ km s}^{-1}$ ) in the Combined sample is shown as a function of impact parameter in two different bins demarcated at the median  $b$ . The circles, diamonds and squares in the top panels show  $C_{21}$  for all the galaxies, galaxies with  $L_B \leq 10^{10} L_\odot$  and galaxies with  $L_B > 10^{10} L_\odot$ , respectively. *Right:* The same as in the figure to the left for impact parameter scaled with effective H I radius (see Section 5.1.2 for details). In both panels, the horizontal dotted lines mark  $\int \tau dv = 0.3 \text{ km s}^{-1}$  and the vertical dotted lines marks the median  $b$  and  $b/R_{\text{HI}}$ .

**Table 3.** Results of correlation analysis between the H I 21-cm absorption strength and various parameters for the Combined sample.

Parameter (1)	N (2)	$r_k$ (3)	$P(r_k)$ (4)	$S(r_k)$ (5)
$b$	69	-0.20	0.01	$2.42\sigma$
$b/R_{\text{HI}}$	67	-0.20	0.01	$2.45\sigma$
$R$	68	-0.16	0.05	$1.90\sigma$
$R/R_{\text{HI}}$	67	-0.18	0.03	$2.13\sigma$
$i$	68	+0.05	0.59	$0.54\sigma$
$\phi$	53	-0.17	0.07	$1.79\sigma$
$\sin(i)\cos(\phi)$	53	+0.15	0.11	$1.58\sigma$
$L_B$	67	-0.02	0.80	$0.26\sigma$
$M_*$	62	-0.01	0.89	$0.15\sigma$
$g-r$	62	-0.03	0.77	$0.30\sigma$
$\Sigma_{\text{SFR}}$	36	-0.03	0.83	$0.22\sigma$

Column 1: Parameter against which correlation of  $\int \tau dv$  is tested. Column 2: Number of measurements included in the test. Column 3: Kendall rank correlation coefficient. Columns 4: Probability of the correlation arising by chance. Column 5: Significance of the correlation assuming Gaussian statistics. The upper limits ( $\int \tau dv_{10}^{3\sigma}$ ) are considered as censored data points while performing survival analysis using the ‘cenken’ function under the ‘NADA’ package in R.

of nearby galaxies detected by the Arecibo Legacy Fast Arecibo L-Band Feed Array (ALFALFA) survey and SDSS (Toribio et al. 2011). H I 21-cm optical depth as a function of the scaled impact parameter is shown in the right panel of Fig. 7.

We find an anti-correlation between  $\int \tau dv$  and  $b/R_{\text{HI}}$ , similar to that between  $\int \tau dv$  and  $b$  (see Table 3). As in the previous section, we find that the anti-correlation between  $\int \tau dv$  and  $b/R_{\text{HI}}$  is mostly driven by the low-luminosity (alternatively low stellar mass or bluer) galaxies. From top right panel of Fig. 7 and Table 4, it can be seen that  $C_{21}$  falls with  $b/R_{\text{HI}}$  and the probability of detecting H I 21-cm absorption at  $b/R_{\text{HI}} > 2$  is very small ( $\leq 0.05$ ). From the same figure, there does not appear to be any

**Table 4.** Covering factor ( $C_{21}$ ) of H I 21-cm absorbers in the Combined sample for different parameters estimated for  $\tau_0 = 0.3 \text{ km s}^{-1}$ .

Parameter range (1)	N (2)	$N_{21}$ (3)	$C_{21}$ (4)
$0.0 < b \text{ (kpc)} \leq 14.6$	33	8	$0.24^{+0.12}_{-0.08}$
$14.6 < b \text{ (kpc)} \leq 33.2$	31	2	$0.06^{+0.09}_{-0.04}$
$0.0 < b/R_{\text{HI}} \leq 2.0$	32	8	$0.25^{+0.12}_{-0.09}$
$2.0 < b/R_{\text{HI}} \leq 34.0$	30	1	$0.03^{+0.08}_{-0.03}$
$0.0 \leq R \text{ (kpc)} < 20.6$	31	6	$0.19^{+0.12}_{-0.08}$
$20.6 \leq R \text{ (kpc)} < 74.0$	32	3	$0.09^{+0.14}_{-0.05}$
$0.0 \leq R/R_{\text{HI}} < 2.4$	31	7	$0.23^{+0.12}_{-0.08}$
$2.4 \leq R/R_{\text{HI}} < 57.0$	31	2	$0.06^{+0.09}_{-0.04}$
$0.0 \leq i \text{ (}^\circ\text{)} < 30.0$	17	3	$0.18^{+0.17}_{-0.10}$
$30.0 \leq i \text{ (}^\circ\text{)} < 57.9$	25	1	$0.04^{+0.09}_{-0.03}$
$57.9 \leq i \text{ (}^\circ\text{)} < 90.0$	26	5	$0.19^{+0.13}_{-0.08}$
$0.0 \leq \phi \text{ (}^\circ\text{)} < 44.9$	25	5	$0.20^{+0.14}_{-0.09}$
$44.9 \leq \phi \text{ (}^\circ\text{)} < 90.0$	26	1	$0.04^{+0.09}_{-0.03}$
$0.0 \leq \sin(i)\cos(\phi) < 0.5$	25	1	$0.04^{+0.09}_{-0.03}$
$0.5 \leq \sin(i)\cos(\phi) < 1.0$	26	5	$0.20^{+0.14}_{-0.09}$

Column 1: The range of parameter values. Column 2:  $N$  is the total number of measurements with  $\int \tau dv_{10}^{3\sigma} \leq \tau_0$ . Column 3:  $N_{21}$  is the number of H I 21-cm detections with  $\int \tau dv_{10}^{3\sigma} \leq \tau_0$  and  $\int \tau dv \geq \tau_0$ . Column 4:  $C_{21} = N_{21}/N$ .

Note that for estimating  $\phi$ , we have considered only galaxies with  $i \geq 30^\circ$ . Errors represent Gaussian  $1\sigma$  confidence intervals computed using tables of Gehrels (1986) assuming a Poisson distribution.

difference in dependence of  $C_{21}$  on  $b/R_{\text{HI}}$  based on the galaxy luminosity. We note that similarly there is no difference in the trend of  $C_{21}$  with  $b/R_{\text{HI}}$  based on stellar mass and colour of galaxies.

We can treat  $\beta$  in the scaling relation between  $R_{\text{HI}}$  and  $L_B$  as a free parameter, in order to check whether the scatter in the relation between  $\int \tau dv$  and  $b/R_{\text{HI}}$  can be reduced. Varying  $\beta$  over 0–0.4 introduces  $\sim 15$ –20% variation in the strength and significance of

the anti-correlation between  $\int \tau dv$  and  $b/R_{\text{HI}}$ . The strongest ( $r_k = -0.24$ ) and most significant ( $S(r_k) = 2.82\sigma$ ) anti-correlation is obtained for  $\beta = 0.2$ . This may suggest that the cold H I gas distribution may not follow the same scaling relation with optical luminosity as that of the total H I gas. However, for consistency we quote the results for  $\beta = 0.4$  throughout this work.

### 5.1.3 Radial distance

We define the radial distance from the galaxy's centre to where the radio sightline passes through the plane of the disk as,

$$R = b[\cos^2 \phi + (\sin^2 \phi / \cos^2 i)]^{1/2}. \quad (1)$$

Here we are assuming that the H I and stellar components of the galaxies have similar morphology. As with  $b$ ,  $\int \tau dv$  is weakly anti-correlated with  $R$ , however the anti-correlation is slightly weaker and less significant (see Table 3). The anti-correlation is retained (at  $\sim 2\sigma$ ) when we scale  $R$  with the effective H I radius,  $R_{\text{HI}}$ , as defined in Section 5.1.2. As in the previous section, the strength and significance of the anti-correlation can change by  $<20\%$  on varying  $\beta$  between 0 to 0.4. Again as with  $b$ , the anti-correlations are stronger for the low-luminosity galaxies. The distribution of H I 21-cm optical depth as a function of  $R$  and  $R/R_{\text{HI}}$  is shown in Fig. 9.

From Table 4 and top panels of Fig. 9, we can see that  $C_{21}$  declines with increasing  $R$  and  $R/R_{\text{HI}}$ . The two galaxies (NGC 3067 (Carilli & van Gorkom 1992) and J135400.68+565000.3 (Zwaan et al. 2015)) in which H I 21-cm absorption arises at  $R/R_{\text{HI}} \geq 3$  are the ones with the radio sightline oriented close to the minor axis. Hence, in these systems the H I 21-cm absorption is not likely to arise from the extended H I disks, but due to high-velocity clouds (HVCs) or tidally disturbed/warped H I disks. We discuss such systems in the next section. From Fig. 9, it can be seen that  $C_{21}$  for galaxies with  $L_B \leq 10^{10} L_\odot$  follows a similar trend, with  $C_{21} \sim 0.3$  at  $R < 20$  kpc and  $R/R_{\text{HI}} < 2$ , and  $C_{21} \lesssim 0.05$  beyond. On the other hand,  $C_{21}$  for galaxies with  $L_B > 10^{10} L_\odot$  seems to be more or less constant ( $\sim 0.1-0.2$ ) with  $R$  and  $R/R_{\text{HI}}$ . The same result holds when we divide galaxies based on their stellar masses and colours.

*In conclusion: Both the H I 21-cm absorption strength ( $\int \tau dv$ ) and detectability ( $C_{21}$ ) around low- $z$  galaxies show a weak declining trend with  $b$ . Similar trends are found on converting  $b$  to the radial distance along the galaxy major axis as well on scaling the distances with the effective H I radius.*

## 5.2 Azimuthal profile of H I 21-cm absorbers

We investigate here whether the distribution of H I 21-cm absorbers around low- $z$  galaxies is spherically symmetric, or whether there is any dependence on the galaxy inclination and orientation of the radio sightline with respect to the galaxy. Due to lack of information about the H I morphology of the galaxies, we assume that the H I disks of the galaxies have the same ellipticity and position angle as that of their stellar disks. Additionally, we assume that the H I disks are not warped or twisted. In Fig. 10 we show the distribution of  $i$  and  $\phi$  of the QGPs, where the sizes of the symbols are based on the galaxy luminosities and their shapes are based on the impact parameters. We remind here that  $\phi$  is estimated only for galaxies with  $i \geq 30^\circ$ . The distributions of  $i$  for galaxies with H I 21-cm detections (median  $\sim 52^\circ$ ) and non-detections (median  $\sim 47^\circ$ ) are not

very different. A two-sided Kolmogorov-Smirnov (KS) test suggests that the maximum deviation between the two cumulative distribution functions is  $D_{KS} = 0.24$  with a probability of  $P_{KS} = 0.4$  (where  $P_{KS}$  is the probability of finding this  $D_{KS}$  value or lower by chance). However, when it comes to  $\phi$ , the distributions for the systems with H I 21-cm detections and the non-detections are quite different ( $D_{KS} = 0.49$  with  $P_{KS} = 0.02$ ). The 21-cm detections have median  $\phi = 21^\circ$  whereas the non-detections have median  $\phi = 47^\circ$ . This suggests that orientation may play a role in determining properties of H I 21-cm absorbers.

From Fig. 10 we can see that H I 21-cm absorption is detected only for  $\phi \lesssim 30^\circ$  (i.e. near the galaxy major axis) and for  $\phi \gtrsim 60^\circ$  (i.e. near the galaxy minor axis). A bimodality in the azimuthal orientation of Mg II absorbing gas around galaxies has been observed, which is believed to be driven by gas accreting along the galaxy major axis and outflowing along the galaxy minor axis (Bouché et al. 2012; Kacprzak et al. 2012; Bordoloi et al. 2014; Nielsen et al. 2015). However, there are only three H I 21-cm detections near the minor axis compared to nine near the major axis. These nine absorption are likely to arise from the H I disk of the galaxies. In all three cases where H I 21-cm absorption has been detected close to galaxy's minor axis,  $b \leq 15$  kpc, i.e. the absorption could be arising from a warped/disturbed H I disk. Indeed in two of these galaxies (NGC 3067 and ESO 1327-2041), the H I 21-cm absorption was found to be arising from the tidally disturbed H I gas around the galaxy (Carilli & van Gorkom 1992). Later studies of these QGPs using Hubble Space Telescope images have attributed the H I 21-cm absorbers to HVCs and extended spiral arm of a merging galaxy (Keeney et al. 2005, 2011; Stocke et al. 2010).

We point out that in the two cases where H I 21-cm absorption have been detected at  $b \gtrsim 20$  kpc (Dutta et al. 2016; Reeves et al. 2016), the galaxies are face-on (i.e.  $i < 30^\circ$ ), and hence the probability of intersecting the H I disk is higher as compared to galaxies with inclined disks. This along with larger number of H I 21-cm detection near the major axis could imply that H I 21-cm absorbers are mostly arising from the plane of the H I disk. In that case, the H I 21-cm optical depth is expected to correlate with the galaxy inclination and orientation. Specifically, the H I 21-cm optical depth should be maximum in the configuration where the sightline is aligned along the major axis of the galaxy which is viewed edge-on, since the sightline would traverse the full H I disk in that case. While we do not find any significant correlation of  $\int \tau dv$  with  $i$ , we find that  $\int \tau dv$  is weakly anti-correlated with  $\phi$  and weakly correlated with  $\sin(i)\cos(\phi)$  (see Table 3).

The covering factor of H I 21-cm absorbers as a function of  $i$ ,  $\phi$  and  $\sin(i)\cos(\phi)$  are given in Table 4.  $C_{21}$  falls from  $0.20^{+0.14}_{-0.09}$  near the major axis ( $\phi < 45^\circ$ ) to  $0.04^{+0.09}_{-0.03}$  near the minor axis ( $\phi \geq 45^\circ$ ), and  $C_{21}$  increases similarly with  $\sin(i)\cos(\phi)$ . To illustrate the dependence of  $C_{21}$  on  $i$  and  $\phi$ , we show in Fig. 10 the SDSS images of typical QGPs from our sample in five bins of  $i$  and  $\phi$  as marked in the top figure. Given below each image is  $C_{21}$  corresponding to that particular bin of  $i$  and  $\phi$ . While the errors are large, it can be seen that  $C_{21}$  is maximum for sightlines that pass near the major axis of edge-on galaxies, and minimum for sightlines that pass near the minor axis of inclined galaxies.

However, we find that  $\phi$  is correlated with  $b$  ( $r_k = +0.28$ ,  $P(r_k) = 0.004$ ,  $S(r_k) = 2.91\sigma$ ) in the Combined sample. This is due to the dearth of galaxies probed along the minor axis at small  $b$ . The correlation is mostly driven by the GOTOQs, where by construct the radio sightlines pass through the optical disks in SDSS images, and hence they are probed both at low  $b$  and at low  $\phi$ . We



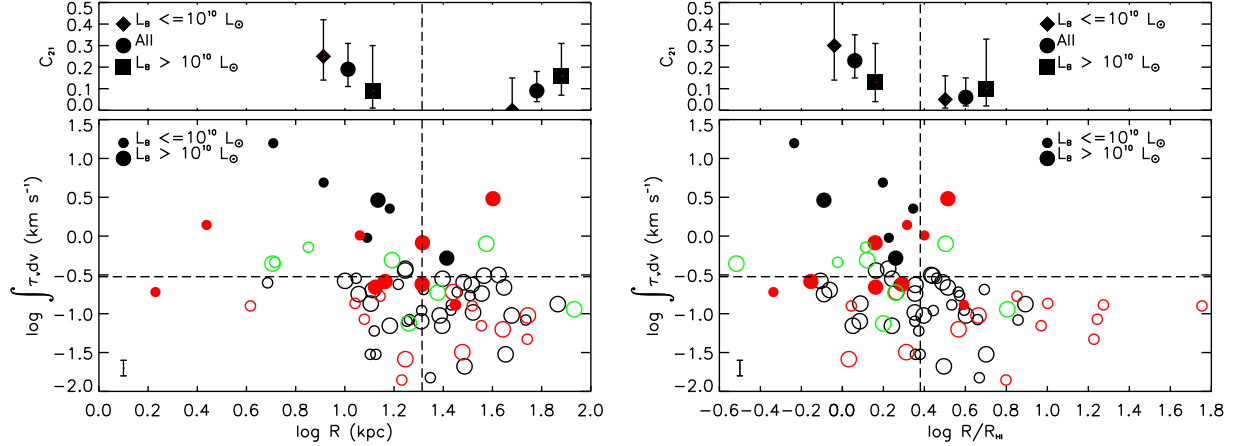


**Figure 9.** Same as in Fig. 7 for (left) the radial distance in the plane of the galaxy disk (as defined in Eqn. 1) and (right) the radial distance scaled by the effective H I radius.

caution that space-based high spatial resolution imaging of these GOTOQs are required to accurately measure their orientation angles. Since the strongest and most significant anti-correlation of  $\int \tau dv$  is found with  $b$  (see Table 3), it is possible that this is driving the weaker and less significant anti-correlation of  $\int \tau dv$  with  $\phi$  (as well as correlation with  $\sin(i)\cos(\phi)$ ). However, if we consider the average  $C_{21}$  within 30 kpc ( $0.16^{+0.07}_{-0.05}$ ; see Fig. 8), we find that it can be enhanced by  $\sim 50\%$  by restricting to sightlines passing close to the disk, i.e.  $C_{21} = 0.24^{+0.19}_{-0.11}$  at  $\phi \leq 30^\circ$ . Further, when we consider galaxies only at  $b < 15$  kpc (where  $C_{21}$  is highest; see Table 4), there is a tendency for more H I 21-cm absorbers to be detected closer to the major axis, i.e.  $C_{21} = 0.31^{+0.21}_{-0.14}$  at  $\phi < 45^\circ$  compared to  $C_{21} = 0.11^{+0.26}_{-0.09}$  at  $\phi \geq 45^\circ$ . However, this is not significant considering the  $1\sigma$  Poisson confidence intervals. More H I 21-cm detections are required to confirm this tentative dependence of  $C_{21}$  and  $\int \tau dv$  on  $\phi$ , and whether it is independent of that on  $b$ .

*In conclusion:  $\int \tau dv$  and  $C_{21}$  show weak dependence on the galaxy orientation, with tentative indication for most of the H I 21-cm absorbers to be co-planar with the H I disks. However, the dependence may not be independent from that on impact parameter.*

### 5.3 Galaxy properties

In Section 5.1, we have seen that the anti-correlation between  $\int \tau dv$  and  $b$  (as well as  $b/R_{\text{HI}}$ ,  $R$  and  $R/R_{\text{HI}}$ ) becomes more pronounced for the low luminosity, low stellar mass, bluer galaxies. However, none of the anti-correlations are at greater than  $\sim 2\sigma$  level of significance. Further, at larger radial distances,  $C_{21}$  tends to be higher for the higher luminosity, higher stellar mass, redder galaxies (see Fig. 9). While the errors are large due to small number statistics, these results seem to indicate that the probability of detecting H I 21-cm absorbers at large galactocentric distances is higher for galaxies with high luminosities and masses, in other words, the H I 21-cm absorbing gas cross-section may be larger for these galaxies.

However, we do not find any significant correlation of  $\int \tau dv$  with luminosity, stellar mass and colour of galaxies (see Table 3). Further, the H I 21-cm detections do not have different distributions of these galaxy properties from the H I 21-cm non-detections. Additionally, we can use the definition of magnitude-dependent  $g-r$

colour cut (Blanton & Berlind 2007), as described in Section 2.3, to classify the galaxies as red and blue. We find that  $C_{21}$  is similar for the blue ( $0.15^{+0.09}_{-0.06}$ ) and the red galaxies ( $0.12^{+0.16}_{-0.08}$ ). However, note that only two of the H I 21-cm absorption detections are from early morphological type galaxies (Gupta et al. 2013; Zwaan et al. 2015).

In order to study the dependence of H I 21-cm absorption on host galaxy SFR, we consider a subset of the galaxies (30) whose spectra are available from SDSS, since all the galaxies in our sample and in the literature do not have homogeneous optical spectra available. We also consider the GOTOQs (6) from which emission lines are detected in the background quasars' SDSS spectra. We estimate the surface SFR density,  $\Sigma_{\text{SFR}}$  (uncorrected for dust attenuation and fibre filling factor) from the H  $\alpha$  flux detected in the SDSS fibre using equations 6 and 7 of Argence & Lamareille (2009). The H I 21-cm optical depth does not have any significant correlation with  $\Sigma_{\text{SFR}}$  (see Table 3). Note that the total SFR of the host galaxies in case of the GOTOQs is likely to be higher than what is measured from the quasar spectra. In addition, we do not find any significant correlation between  $\int \tau dv$  and the SFR as well as the specific SFR (SFR per unit stellar mass) estimated from photometric measurements by the *kcorrect* algorithm. However, consistent measurement of SFR for all the galaxies is required to confirm any trend between  $\int \tau dv$  and star formation. Finally we note that, over the redshift range (0–0.4) probed by the Combined sample, we do not find any significant ( $< 1\sigma$ ) redshift evolution of  $\int \tau dv$  and  $C_{21}$ .

*In conclusion: We do not find any significant dependence of the strength and distribution of H I 21-cm absorbers on the host galaxy properties studied here, i.e. luminosity, stellar mass, colour,  $\Sigma_{\text{SFR}}$  and redshift.*

### 5.4 Kinematics

The H I 21-cm absorption lines are detected within  $\sim \pm 150 \text{ km s}^{-1}$  of the systematic redshift of the galaxy, with median value  $\sim 60 \text{ km s}^{-1}$ . Absorption from metal lines at the redshift of the H I 21-cm absorption have been detected in the SDSS spectra of the quasars in most cases (see Section 6.1). However, high resolution optical spectra of the quasars are required to compare the kinematics of the H I 21-cm absorption and the metal lines.

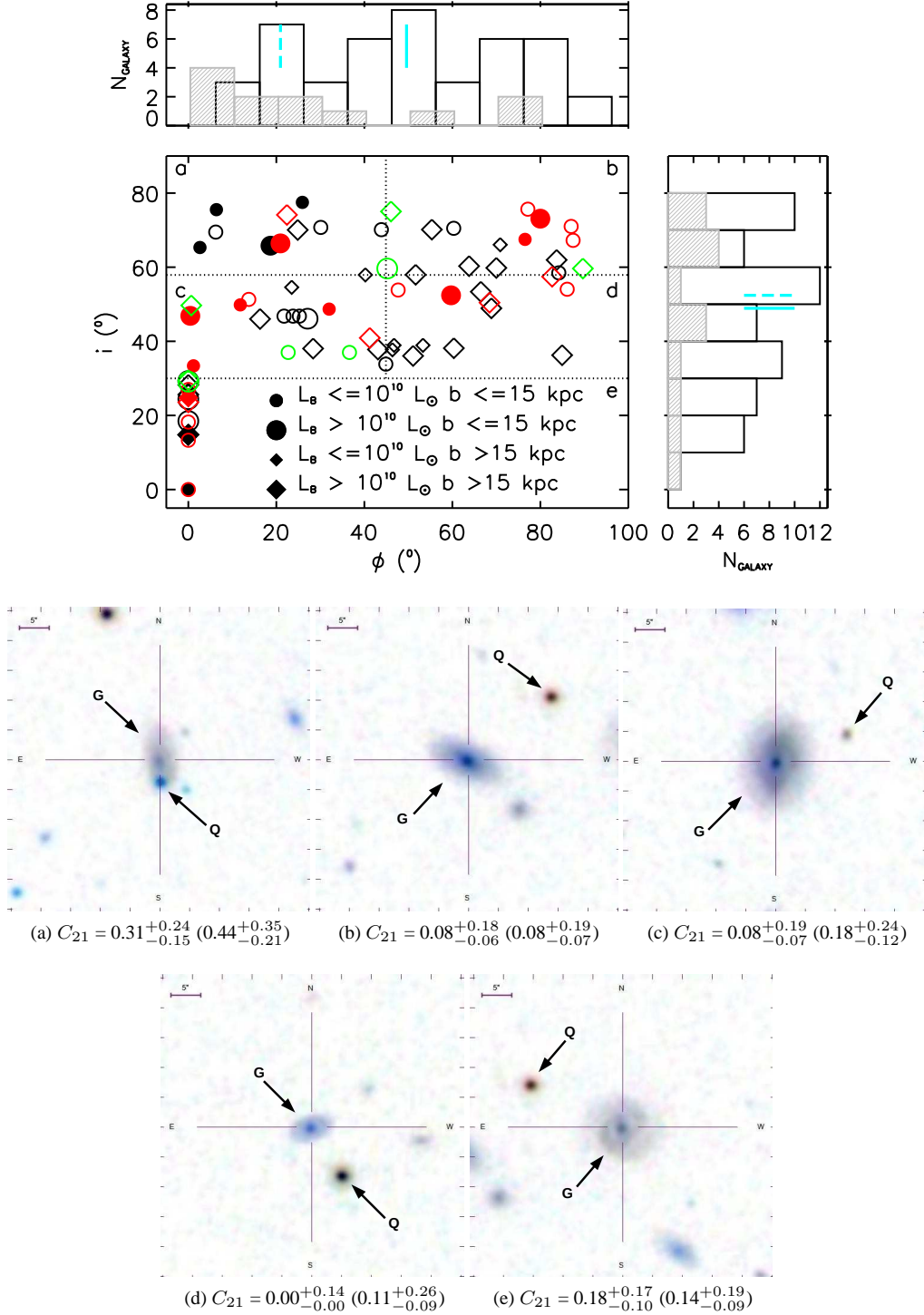


**Figure 10.** *Top:* The distribution of galaxy inclination ( $i$ ) and orientation ( $\phi$ ) angles for the QGPs in the primary sample (black), the literature sample (red), and the supplementary sample (green). The filled symbols are for the H I 21-cm detections and the open symbols are for the non-detections. The small symbols are for galaxies with  $L_B \leq 10^{10} L_\odot$  while the large symbols are for galaxies with  $L_B > 10^{10} L_\odot$ . The circles represent QGPs with  $b \leq 15$  kpc and the diamonds represent QGPs with  $b > 15$  kpc. Note that for galaxies with  $i < 30^\circ$  (i.e. face-on galaxies) we do not estimate  $\phi$ , but we show them at  $\phi = 0^\circ$  in the plot. The horizontal dotted lines mark  $i = 30^\circ$  and  $57^\circ$  and the vertical dotted line marks the median  $\phi = 43^\circ$ . The five different bins of  $i$  and  $\phi$  as marked with the dotted lines are identified by a, b, c, d and e. The histogram plots of  $i$  and  $\phi$  (excluding the supplementary measurements) are shown to the right and top, respectively. The open histograms are for the non-detections and the filled histograms are for the detections. The median values of  $i$  and  $\phi$  for the detections and the non-detections are marked by dashed and solid ticks, respectively. *Bottom:* SDSS composite colour images of five QGPs from our sample are shown as examples of the QGP configurations in the five bins a, b, c, d and e as marked in the figure to the top. The quasars and galaxies are identified by ‘Q’ and ‘G’, respectively. The covering factor of H I 21-cm absorbers for  $\tau_0 = 0.3 \text{ km s}^{-1}$  for galaxies in the Combined sample in a particular  $i$  and  $\phi$  bin are given below the corresponding image ( $C_{21}$  for  $\tau_0 = 0.2 \text{ km s}^{-1}$  are given in parenthesis).

Considering the H I 21-cm absorption detections where the lines are resolved, the lines have  $v_{90}$  in the range  $\sim 4\text{--}70\text{ km s}^{-1}$ , with median  $\sim 22\text{ km s}^{-1}$  ( $v_{90}$  is the velocity width within which 90% of the total optical depth is detected). The FWHM, from Gaussian fits of all the H I 21-cm absorption components which are resolved, is in the range  $\sim 4\text{--}50\text{ km s}^{-1}$ , with median  $\sim 10\text{ km s}^{-1}$ . The upper limits on the gas kinetic temperature, obtained assuming the line widths are purely due to thermal motion, range over  $\sim 300\text{--}60000\text{ K}$ . Note that Borthakur et al. (2010) have detected a narrow, single channel (FWHM  $\sim 1.1\text{ km s}^{-1}$ ) H I 21-cm absorption towards a dwarf galaxy (UGC 7408), which corresponds to  $T_K \sim 26\text{ K}$ . The typical temperature of the CNM gas ( $\sim 100\text{ K}$ ) corresponds to a thermal velocity dispersion of  $\sim 1\text{ km s}^{-1}$  (FWHM  $\sim 2\text{ km s}^{-1}$ ), while that of the WNM gas ( $\sim 5000\text{--}8000\text{ K}$ ) corresponds to  $\sim 6\text{--}8\text{ km s}^{-1}$  (FWHM  $\sim 14\text{--}19\text{ km s}^{-1}$ ), and spectral lines broader than this can be attributed to non-thermal motion in the ISM (Wolfire et al. 1995; Heiles & Troland 2003). However, we note that some of the large line widths of the H I 21-cm absorption can also be due to structure of the background radio sources, and multi-wavelength sub-arcsecond-scale images of the radio sources are required to characterize their structure (Gupta et al. 2012).

The kinematics of the H I 21-cm absorbers are expected to shed light on their spatial distribution. We do not find any significant correlation ( $<1.5\sigma$ ) between the kinematical parameters of the H I 21-cm absorbers and the various geometrical parameters explored in the previous sections. However, we note that we are limited by the small number of detections to infer any general trends. In addition, information about the velocity field of the galaxies is required to interpret the kinematics of the H I 21-cm absorbers.

## 6 DISCUSSION

In Section 5, we have studied the radial and azimuthal profiles of H I 21-cm absorption around low- $z$  galaxies. We have quantified the covering factor of H I 21-cm absorbers as a function of various geometrical parameters. We have found that the covering factor of H I 21-cm absorbers decreases with increasing impact parameter/radial distance. Further, the distribution of galaxy orientation hints that most of the H I 21-cm absorbers could be co-planar with the H I disks. Additionally, we have found that the distribution of H I 21-cm absorbers is more sensitive to geometrical parameters than physical parameters related to the star formation in galaxies.

The next step would be to relate the distribution of H I 21-cm absorbers with the distribution of cold H I gas around low- $z$  galaxies. However, that is not very straightforward since the H I 21-cm optical depth depends on  $N(\text{H I})$ ,  $T_s$  and  $C_f$ . It is difficult to quantify  $C_f$  since sub-arcsecond resolution images of all the radio sources are not available. We find  $C_{21} = 0.18^{+0.09}_{-0.06}$  towards radio sources that are compact at arcsecond-scale resolution in the Combined sample, as compared to  $C_{21} = 0.10^{+0.13}_{-0.06}$  towards those that are resolved. Note that Gupta et al. (2012) have found that the H I 21-cm detection rate is higher towards the quasars with flat or inverted spectral index at cm wavelengths and towards the quasars with linear sizes less than  $100\text{ pc}$  (see their figure 6).

For the purpose of the discussion here if we consider  $C_f \sim 1$ , the non-detection of H I 21-cm absorption could mean either that there is lack of H I gas along the sightline or that most of the H I gas along the sightline is warm. Independent information about H I gas along the sightline, for example from absorption from Lyman- $\alpha$  or metals in the optical/UV spectra or from H I 21-cm emission, can

lift this degeneracy. Stacking the spectra of all the H I 21-cm non-detections can help to detect weak absorption that is not detected due to noise in individual spectra. However, we do not detect any H I 21-cm absorption in the stacked spectrum and estimate  $\int \tau dv_{10}^{3\sigma} \leq 0.009\text{ km s}^{-1}$ . Hence, we can place constraint on the average  $N(\text{H I})$  along these sightlines as  $\leq 18.2$  ( $19.2$ ) for  $T_s = 100$  ( $1000$ ) K and  $C_f = 1$ .

From the results presented in Section 5, it appears that majority of the H I 21-cm non-detections could be due to the radio sightline not intersecting the H I disk of the galaxy. In  $\sim 77\%$  of the non-detections, the sightline passes outside twice the expected radius containing 50% of the H I mass of the galaxy or away from the major axis ( $\phi \geq 30^\circ$ ) of the galaxy. In rest of the H I 21-cm non-detections where the sightline is likely to pass through the H I disk, the non-detections could be due to the H I gas along the sightline being warm or small filling factor of cold gas. Radio interferometric H I 21-cm emission maps are available for only three of the galaxies with H I 21-cm non-detections. One of them has been discussed in Section 4.2, where the radio sightline passes through the outer regions of the H I disc. In the other two cases, the radio sightline does not pass through the H I disc (Greisen et al. 2009) or H I 21-cm emission is not detected from the galaxy (Carilli & van Gorkom 1992), respectively.

Next, we discuss about metal absorption towards the quasars in our sample in Section 6.1, and compare our results with H I 21-cm absorption searches from low- $z$  DLAs in Section 6.2. Finally, we discuss the implications of our results on the redshift evolution of H I 21-cm absorbers in Section 6.3.

### 6.1 Metal absorption

Ca II and Na I absorption are believed to arise from neutral gas near star-forming regions. Measurements of Ca II and Na I rest equivalent widths from the SDSS spectra of the background quasars are possible for 43 of the QGPs in the Combined sample. Ca II measurement is available for three other QGPs from Womble (1993). Ca II and Na I measurements from Keck High Resolution Echelle Spectrometer (HIRES) spectrum are available towards the QGP J0041–0043 (Dutta et al. 2016). Out of the 16 sightlines towards which H I 21-cm absorption have been detected, metal line absorption information is available for 11 cases. Absorption from either Ca II or Na I or both is detected in 9 of these systems. However, in two cases of H I 21-cm absorption detection (Borthakur et al. 2010, 2014), no metal lines are detected in the SDSS spectra ( $3\sigma$  upper limits on  $W_r(\text{Ca II}) \leq 1.1\text{ \AA}$  and  $\leq 0.27\text{ \AA}$ , and  $W_r(\text{Na I}) \leq 0.35\text{ \AA}$  and  $\leq 0.17\text{ \AA}$ , respectively).

We do not find any correlation of  $\int \tau dv$  with  $W_r(\text{Ca II})$  and  $W_r(\text{Na I})$ . Furthermore, there does not appear to be a minimum  $W_r(\text{Ca II})$  or  $W_r(\text{Na I})$  beyond which H I 21-cm absorption is detected with high probability and vice versa. However, higher resolution optical spectra towards the background quasars are required to study in detail the connection between Ca II and/or Na I absorption and H I 21-cm absorption. In most cases of H I 21-cm non-detections, Na I or Ca II absorption lines are not detected in the SDSS spectra. Stacking of the SDSS spectra without metals lines detected at the redshift of the galaxies gives  $3\sigma$  upper limit on  $W_r(\text{Ca II}) \leq 0.094\text{ \AA}$  and  $W_r(\text{Na I}) \leq 0.046\text{ \AA}$ . Assuming linear part of the curve of growth and correlation between  $N(\text{H I})$  and  $N(\text{Na I})$  as in the Milky Way (Wakker & Mathis 2000), gives  $\log N(\text{H I}) \leq 19.5$ . However, note that unlike in the Milky Way, no correlation is found between  $N(\text{Ca II})$  and  $N(\text{H I})$  in DLAs/sub-

DLAs over the range of  $\log N(\text{H I}) = 19.5\text{--}21.5$  (Rahmani et al. 2016).

It is interesting to note that in eight cases H I 21-cm absorption is not detected despite Ca II or Na I absorption being present along the quasar sightline. Note that these eight QGPs have a range of  $b$  ( $\sim 10\text{--}30$  kpc) as well as galaxy orientation ( $\sim 30^\circ\text{--}80^\circ$ ). In these cases at least one knows that H I gas is present along the sightline. One such case has been discussed in Section 4.3, where Ca II absorption has been detected but no H I 21-cm or Na I absorption. Another such example is J0041–0143, where Ca II and Na I absorption have been detected towards the core but not H I 21-cm absorption (Dutta et al. 2016). Interestingly, H I 21-cm absorption is detected towards one of the lobes ( $\sim 4$  kpc away from the core) of this radio source, implying a patchy distribution of cold gas in the H I disc. Comparison of the  $N(\text{H I})$  estimated from the metal column densities assuming optically thin gas and correlations seen in the Milky Way (Wakker & Mathis 2000), with the H I 21-cm optical depth measurements, indicates that the H I gas along these sightlines is likely to be warmer than 100 K.

The ratio of column density of Na I to Ca II can be used to probe the physical conditions in the gas. High values ( $\gtrsim 1$ ) of  $N(\text{Na I})/N(\text{Ca II})$  are expected in the cold dense ( $T \lesssim 100$  K,  $n_{\text{H}} \gtrsim 100\text{ cm}^{-3}$ ) ISM where Ca is usually heavily depleted onto dust grains, whereas low values ( $\lesssim 1$ ) are expected in the warmer diffuse gas ( $T \gtrsim 1000$  K,  $n_{\text{H}} \lesssim 10\text{ cm}^{-3}$ ), where most of Ca is still in the gas phase (Welty et al. 1996). The ratio of  $W_r(\text{Na I})/W_r(\text{Ca II})$  is  $\lesssim 1$  ( $N(\text{Na I})/N(\text{Ca II}) < 1$  under the optically thin approximation) in most ( $\sim 90\%$ ) cases of H I 21-cm absorption, indicating that these sightlines are not likely to be passing through the dusty star-forming disks. Only in one case of H I 21-cm detection, it has been demonstrated that the sightline is probing the translucent (defined as a region with  $1 \leq A_V \leq 10$ ; van Dishoeck & Black 1989; Snow & McCall 2006) of the foreground galaxy (Srianand et al. 2013). The quasar shows strong reddening along with absorption from Na I and diffuse interstellar band in this case. The poor SNR of the SDSS spectrum near the wavelength of the Ca II absorption prevents measurement of  $W_r(\text{Ca II})$  ( $3\sigma$  upper limit on  $W_r(\text{Ca II}) \leq 2.3$  Å). Out of the eight H I 21-cm absorbers for which  $W_r(\text{Ca II})$  is measured, only two have  $W_r(\text{Ca II}) \geq 0.7$  Å and can be classified as strong absorbers, while the rest can be classified as weak absorbers, according to Wild et al. (2006); Sardane et al. (2015). Based on abundance patterns and dust extinction, the former is shown to have properties intermediate between halo- and disc-type gas, while the latter is shown to have properties consistent with halo-type gas (Sardane et al. 2015). This is again consistent with the fact that even at low impact parameters, most of the sightlines studied here do not pass through the stellar disk of galaxies where there is ongoing star formation.

## 6.2 H I 21-cm absorption from low- $z$ DLAs

The QGPs discussed in this work have been selected based on the presence of a foreground galaxy at small angular separation from a background quasar, with no prior information about absorption along the quasar sightline, i.e. this sample of QGPs is absorption-blind. On the other hand, there have been numerous searches for H I 21-cm absorption in literature from samples selected on the basis of absorption lines (Mg II or Lyman  $-\alpha$ ) detected in the optical/UV spectra of the quasar (e.g. Briggs & Wolfe 1983; Kanekar & Chengalur 2003; Curran et al. 2005; Gupta et al. 2009; Curran et al. 2010; Srianand et al. 2012; Gupta et al. 2012; Kanekar et al. 2014). However, most of these have been at high- $z$

( $z > 1$ ), where identification of the host galaxy is difficult. In Table 5, we list 13 DLAs at  $z < 1$  that have been searched for H I 21-cm absorption in literature and whose host galaxies have been identified subsequently. Note that in some cases the host galaxy identification is based on photometric redshift or proximity to the quasar sightline. From Table 4 of Kanekar et al. (2014), we see that these systems have a range of  $T_s$  (median  $\sim 800$  K) and metallicities (median  $\sim -0.8$ ). Sufficient information is not available for all the DLA host galaxies in order to study the dependence of the H I 21-cm optical depth on orientation and other galaxy properties. H I 21-cm absorption has been detected in 10 of these DLAs.

In Fig. 11, we show the distribution of H I 21-cm optical depth as a function of impact parameter for the QGPs studied in the Combined sample and the DLAs listed in Table 5. It can be seen that the distribution and range of  $\int \tau dv$  values for the DLAs are not different from those of the QGPs, and median  $b = 13$  kpc and 15 kpc for the DLAs and the QGPs, respectively. We do not find any correlation between  $\int \tau dv$  and  $b$  of the DLAs ( $r_k = -0.05$ ,  $P(r_k) = 0.85$ ,  $S(r_k) = 0.24\sigma$ ). Unlike in the case of QGPs, the covering factor of H I 21-cm absorbers in case of DLAs remains more or less constant ( $\sim 0.6$ ) with  $b$ . The overall covering factor in DLAs ( $C_{21}^{\text{DLA}} = 0.62^{+0.30}_{-0.21}$ ) is higher by a factor of  $\sim 4$  (at  $2\sigma$  significance) compared to that in the QGPs ( $C_{21} = 0.16^{+0.07}_{-0.05}$ ). We note that the detection rate of H I 21-cm absorption in low- $z$  DLAs is comparable to that of molecular  $\text{H}_2$  absorption in low- $z$  DLAs/sub-DLAs ( $\sim 50\%$ ; Muzahid et al. 2015). Further, it has been found that the covering fraction of Mg II absorbers around low- $z$  galaxies drops from unity to  $\lesssim 0.5$  when going from absorption-selected samples to galaxy-selected samples (e.g. Bergeron & Boissé 1991; Steidel 1995; Bechtold & Ellingson 1992; Tripp & Bowen 2005). This is consistent with cold gas clouds in the extended disks/halos of galaxies having small sizes (parsec to sub-parsec scale) and being patchy in distribution. Indeed, variations in the H I 21-cm optical depth have been detected from parsec-scales (Srianand et al. 2013; Biggs et al. 2016) to kilo-parsec-scales (Dutta et al. 2016), indicating varying covering fractions over different spatial scales. Further, the H I 21-cm optical depth is known to vary as a power law over AU- to pc-scales (Stanimirović et al. 2010; Roy et al. 2012; Dutta et al. 2014).

With a simple approach we can try to reconcile the measured covering factors of H I 21-cm absorption in DLAs and QGPs. We can estimate the covering factor of DLAs ( $C_{\text{DLA}}$ ) around low- $z$  galaxies using  $C_{21} = C_{21}^{\text{DLA}} \times C_{\text{DLA}}$ . We have seen that  $C_{21}^{\text{DLA}}$  is remaining constant (0.6) with  $b$  (for  $b \lesssim 30$  kpc), while  $C_{21}$  shows a declining trend with  $b$  (Fig. 11). However, the errors on  $C_{21}$  being large, we assume for the sake of simplicity a constant  $C_{21}$  of  $\sim 0.2$  within  $b \leq 30$  kpc (see Fig. 8), and no luminosity dependence of  $C_{21}$ . Hence, using these we obtain average  $C_{\text{DLA}} \sim 0.3$  at  $b \lesssim 30$  kpc. Therefore, one can have a consistent picture where the covering factor of gas that can produce DLA absorption is  $\sim 0.3$  around galaxies for  $b \leq 30$  kpc. Roughly sixty percent of these clouds have cold gas that can produce detectable 21-cm absorption. However, we caution that most of the QGPs discussed in this work are at  $z \leq 0.2$  (Fig. 2), while all except one of the low- $z$  DLAs are at  $z \geq 0.2$  (Table 5).

We can use the following relation between the geometrical cross-section of the absorbers and the absorber number density per unit redshift ( $dN/dz$ ) to infer the spatial extent of absorbing gas

around galaxies (see e.g. Schaye et al. 2007; Kacprzak et al. 2008),

$$\frac{dN}{dz} = \frac{1}{2} \frac{c}{H_0} \frac{(1+z)^2}{\sqrt{\Omega_M(1+z)^3 + \Omega_\Lambda}} \Phi^* \Gamma(1+\alpha+2\beta, \frac{L_{min}}{L^*}) C \pi R^{*2}, \quad (2)$$

where,  $\Phi^*$  is the number density of  $L^*$  galaxies,  $\alpha$  is the faint-end slope of the Schechter galaxy luminosity function,  $\beta$  is a parameter to scale the radius with luminosity ( $R/R^* = (L/L^*)^\beta$ ),  $L_{min}$  is the minimum luminosity of galaxies contributing to absorption,  $C$  is the covering factor of the absorber, and  $R^*$  is the absorber radius for an  $L^*$  galaxy. The factor  $1/2$  is to account for the average projection of the physical cross-section area on the sky plane, assuming disc geometry (see Section 5.2). We adopt the Schechter function fit of  $\Phi^* = 1.49 \pm 0.04 \times 10^{-2} h^3 \text{ Mpc}^{-3}$ ,  $M^* = -5 \log_{10} h = -20.44 \pm 0.01$ ,  $\alpha = -1.05 \pm 0.01$ , estimated by Blanton et al. (2003) for SDSS  $r$ -band data of galaxies at  $z = 0.1$ . We assume a luminosity scaling of radius with  $\beta = 0.4$  as estimated from H I sizes of galaxies (see Section 5.1.2). We consider galaxies down to  $L_{min} = 0.05L^*$ , though we note that for the values of  $\alpha$  and  $\beta$  considered here, the value of the incomplete gamma function in Eqn. 2 does not depend significantly on the choice of  $L_{min}$ . Then for  $dN/dz$  of DLAs,  $n_{DLA} = 0.045 \pm 0.006$ , at  $z = 0$  as obtained by Zwaan et al. (2005),  $C_{DLA}$  is unity for  $R^* = 30$  kpc. However, if  $C_{DLA}$  were lower, then  $R^*$  could be larger than 30 kpc. For example if  $C_{DLA} = 0.3$  as obtained above, then  $R^* \sim 60$  kpc.

There exists no measurement of the covering factor and extent of gas that can produce DLAs around low- $z$  galaxies in literature. Though we note that host galaxies of  $z < 1$  DLAs have been detected upto  $b \sim 70$  kpc with median  $b \sim 17$  kpc (Rao et al. 2011). Richter et al. (2011) estimated the mean projected covering factor of  $z < 0.5$  Ca II absorbers around galaxies as 0.33 and the characteristic radial extent of partly neutral gas clouds (HVCs) with  $\log N(\text{H I}) \geq 17.4$  around  $L \geq 0.05L^*$  galaxies as  $\sim 55$  kpc. Note that they have not assumed any luminosity scaling of galaxy sizes, i.e.  $\beta = 0$ , and have considered a spherical distribution of the neutral gas clouds. Under these assumptions (i.e.  $\beta = 0$  and not considering the factor  $1/2$  in Eqn. 2), we obtain  $R^* \sim 30$  kpc for  $C_{DLA} = 0.3$  and  $R^* \sim 15$  kpc for  $C_{DLA} = 1$ . Kacprzak et al. (2008) estimated a covering factor of  $\sim 0.5$  and  $R^*$  of  $\sim 120$  kpc for Mg II absorbers at  $z = 0.5$  around  $L \geq 0.05L^*$  galaxies, for  $\beta = 0.2$  and spherical halo. For comparison, we obtain  $R^* \sim 37$  kpc for  $C_{DLA} = 0.3$  and  $R^* \sim 20$  kpc for  $C_{DLA} = 1$ , under the same assumptions. The larger covering factor and halo radius of the Mg II absorbers is expected since Mg II absorbers can trace partly ionized gas with lower  $N(\text{H I})$  (sub-DLAs and Lyman limit systems) which extends further out from the galaxy.

### 6.3 Redshift evolution of H I 21-cm absorbers

We can use Eqn. 2 to estimate the  $dN/dz$  of H I 21-cm absorbers ( $n_{21}$ ) at low redshift. We assume that the distribution of H I 21-cm absorbers is planar, and  $C_{21}$  is constant ( $\sim 0.2$ ) within  $R^*$  with no luminosity dependence. We consider  $R^*$  for H I 21-cm absorbers around low- $z$  galaxies to be  $\sim 30$  kpc, where we have measured  $C_{21}$ . Under these assumptions, we obtain the  $n_{21}$  at  $z = 0.1$  as  $0.008^{+0.005}_{-0.004}$ . In Fig. 12, we show our  $n_{21}$  estimate along with those made by Gupta et al. (2012) based on search for H I 21-cm absorption in Mg II absorbers and DLAs. We also show for comparison  $n_{DLA}$  at  $z = 0$  as estimated by Zwaan et al. (2005), at  $z = 0.6$  as estimated by Neeleman et al. (2016), and its redshift evolution as estimated by Rao et al. (2006), i.e.  $n_{DLA}(z) = n_0(1+z)^\gamma$  with  $n_0 = 0.044 \pm 0.005$  and  $\gamma = 1.27 \pm 0.11$ . Note that the  $n_{21}$  mea-

**Table 5.** List of  $z < 1$  DLAs from the literature with H I 21-cm absorption measurement and host galaxy information.

Quasar	$z_{\text{abs}}$	$\int \tau dv$ ( $\text{km s}^{-1}$ )	$b$ (kpc)	Ref.
(1)	(2)	(3)	(4)	(5)
0235+164	0.5243	13.1	13.1	1,2
0454+039	0.8596	$\leq 0.10$	5.5	1,2
0738+313	0.0912	1.05	$< 3.4^a$	2,3
0738+313	0.2212	0.49	19.2	1,2
0827+243	0.5247	0.23	32.8	1,2
0952+179	0.2378	0.12	$< 4.2^a$	1,2
1122-168	0.6819	$\leq 0.06$	$25.2^b$	1,2
1127-145	0.3127	3.02	45.6	1,2
1229-021	0.3950	1.36	$7.5^a$	1,2
1243-072	0.4367	0.82	12.5	4
1331+305	0.6922	0.91	$6.4^a$	2,5
1629+120	0.5318	0.49	$17.1^b$	1,6
2149+212	0.9115	$\leq 0.10$	$13.3^a$	1,2

Column 1: Quasar name. Column 2: Absorption redshift. Column 3: Integrated H I 21-cm optical depth in case of detections or  $3\sigma$  upper limit with data smoothed to  $10 \text{ km s}^{-1}$  in case of non-detections. Column 4: Projected separation or impact parameter (kpc) between radio sightline and centre of galaxy. Columns 5: References — 1: Rao et al. (2011); 2: Kanekar et al. (2014); 3: Turnshek et al. (2001); 4: Kanekar et al. (2002); 5: Le Brun et al. (2000); 6: Kanekar & Chengalur (2003).  
<sup>a</sup> based on proximity <sup>b</sup> based on photometric redshift

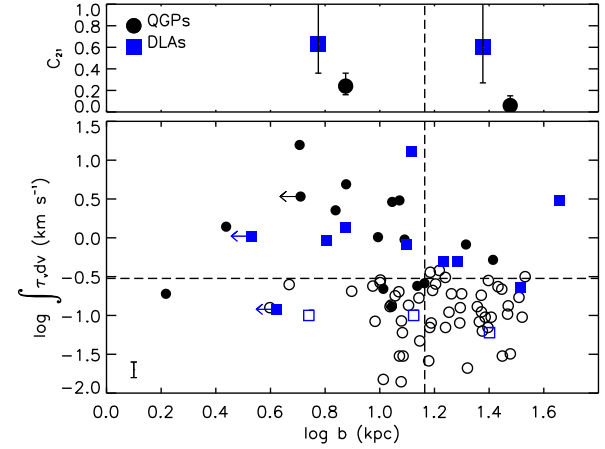


**Figure 11.** Integrated H I 21-cm optical depth around galaxies as a function of impact parameter. The black circles and blue squares are for QGPs in the Combined sample and  $z < 1$  DLAs from the literature, respectively. The solid and open symbols represent  $\int \tau dv$  and  $\int \tau dv_{10}^{3\sigma}$  of the H I 21-cm detections and non-detections, respectively. The typical error in the optical depth measurements is shown at the bottom left of the plot. The horizontal dotted line marks  $\int \tau dv = 0.3 \text{ km s}^{-1}$  and the vertical dotted line marks  $b = 15$  kpc. To the top of the plot, the covering factor of H I 21-cm absorbers (for  $\tau_0 = 0.3 \text{ km s}^{-1}$ ) is shown as a function of impact parameter in two different bins demarcated at the median  $b$ .

surements at different redshifts, while obtained for an uniform sensitivity of  $\tau_0 = 0.3 \text{ km s}^{-1}$ , are based on different kinds of systems, possibly having different  $N(\text{H I})$  thresholds used in the target selection. For example, all the Mg II systems at  $z \sim 1.3$  used to derive  $n_{21}$  need not be DLAs and all the QGPs in our sample need not produce Mg II absorption with rest equivalent width greater than  $1 \text{ \AA}$ . Therefore, the correct mapping of  $n_{21}(z)$  has to wait till the advent of large blind H I 21-cm absorption surveys using SKA pathfind-



ers. Here we make some generic statements based on the measurements in hand. It is interesting to note that the  $n_{21}$  we infer from our QGP observations is lower than what has been found from the high- $z$  Mg II absorbers and DLAs. We try to understand this by using Eqn. 2 and the measured redshift evolution of  $L^*$  and  $\Phi^*$  of galaxies.

Firstly, the expected  $n_{21}(z)$  for no intrinsic redshift evolution in all of the parameters in Eqn. 2 is shown in Fig. 12 (solid cyan curve). Next, from the measured redshift evolution of the galaxy luminosity function in the optical bands, it can be seen that  $L^*$  evolves as  $\sim (1+z)^{2.7}$  and  $\Phi^*$  evolves as  $\sim (1+z)^{-1}$  (Gabasch et al. 2004; Ilbert et al. 2005; Dahlen et al. 2007). The redshift evolution of  $L^*$  comes into Eqn. 2 in two ways. First is through the dependence of  $R^*$  on  $L^*$  ( $R^* \sim L^{*0.4}$ ), and second is through the incomplete gamma function. For the simplistic calculation here we neglect any redshift evolution in the value of the incomplete gamma function. If we assume that the scaling relation between galaxy luminosity and H I size, as well as  $C_{21}$ , do not evolve with redshift, then it can be seen from Fig. 12 that  $n_{21}$  is expected to increase with redshift (short dashed blue curve). However, galaxies of all morphological types have been observed to have much smaller sizes at high redshifts, with the effective optical radius of disc galaxies decreasing as  $\sim (1+z)^{-1}$  (Trujillo et al. 2007; Buitrago et al. 2008; van der Wel et al. 2014). Assuming that  $R^*$  of H I 21-cm absorbers follows the redshift evolution of the optical radius of disc galaxies and factoring in its decrease with redshift, we find that  $n_{21}$  is expected to decrease with redshift for constant  $C_{21}$  (Fig. 12; dotted-dashed purple curve). On the other hand, observations suggest that  $n_{21}$  is increasing with redshift, i.e.  $n_{21}(z) = 0.007(1+z)^{1.58}$  (Fig. 12; long dashed red curve). Further, the covering factor of cold gas is expected to decrease with redshift, with  $C_{21}^{DLA}$  at  $z < 1$  being  $\sim 0.6$  compared to  $\sim 0.2$  at  $2.0 \leq z \leq 3.5$  (Srianand et al. 2012). This basically implies that if we take into account the evolution of size and luminosity of galaxies with redshift, the radius of the cold H I gas around a galaxy that gives rise to H I 21-cm absorption will be much higher at high- $z$  than what is seen at low- $z$  for a galaxy with same optical luminosity.

As noted above, the interpretation of the redshift evolution of H I 21-cm absorbers based on the present measurements is difficult due to the large errors and different selection techniques used at different redshifts. Accurate (upto  $\sim 10\%$ ) and uniform determination of the redshift evolution of  $n_{21}$  and hence that of the cold gas fraction in galaxies at  $z \leq 1.5$  will be possible with the upcoming blind H I 21-cm absorption line surveys, e.g. the MeerKAT Absorption Line Survey, the Search for H I absorption with APTIF, and the ASKAP First Large Absorption Survey in H I (see e.g. Allison et al. 2016). Preliminary results of blind H I 21-cm absorption searches from the ALFALFA survey (Darling et al. 2011; Wu et al. 2015) and ASKAP (Allison et al. 2015) are already beginning to demonstrate the ability of future blind H I 21-cm absorption surveys.

## 7 SUMMARY

We have presented in this work the results from our survey of H I 21-cm absorption of a large sample (55) of low- $z$  ( $z < 0.4$ ) galaxies at small impact parameters to background radio sources using the GMRT, WSRT and VLA. Our primary sample of 40 QGPs spans a range of impact parameters (5–34 kpc) and galaxy types ( $\log M_* \sim 7.8$ – $11.0 M_\odot$ ,  $\log L_B \sim 8.5$ – $10.6 L_\odot$ ,  $g-r \sim 0.1$ – $1.6$ ). The H I 21-cm spectral line measurements from our survey have increased

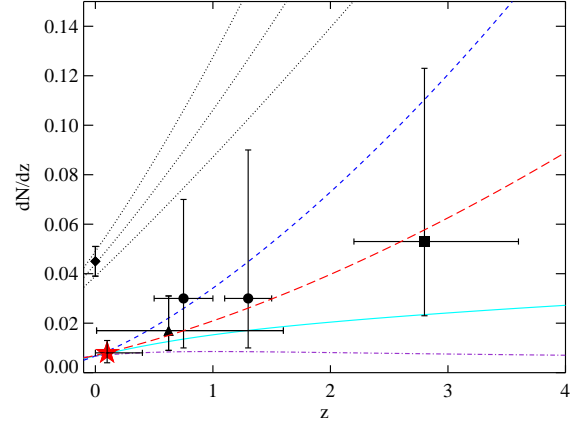


**Figure 12.** Number of H I 21-cm absorbers per unit redshift range for  $\tau_0 = 0.3 \text{ km s}^{-1}$ . The red star is the  $n_{21}$  estimated in this work. The circles and the square are the  $n_{21}$  estimates based on Mg II and DLAs, respectively (Gupta et al. 2012). Also shown for reference are  $n_{DLA}$  at  $z = 0$  estimated by Zwaan et al. (2005) (diamond),  $n_{DLA}$  at  $z = 0.6$  estimated by Neeleman et al. (2016) (triangle) and its redshift evolution estimated by Rao et al. (2006) with errors (dotted black lines). The long dashed red line is a fit by eye to the  $n_{21}$  estimates,  $n_{21}(z) = n_0(1+z)^\gamma$  with  $n_0 = 0.007$  and  $\gamma = 1.58$ . The solid cyan curve represents no intrinsic evolution in the product of space density and cross-section of H I 21-cm absorbers, normalized at  $z = 0.1$ . The short dashed blue curve represents the redshift evolution of  $n_{21}$  for the observed redshift evolution of  $L^*$  and  $\Phi^*$  of galaxies (and no evolution in  $C_{21}$ ). The dotted-dashed purple curve represents  $n_{21}(z)$  accounting for the redshift evolution of sizes of galaxies in addition to that of  $L^*$  and  $\Phi^*$ , and constant  $C_{21}$ .

the number of existing sensitive (i.e.  $\int \tau dv_{10}^{3\sigma} \sim 0.3 \text{ km s}^{-1}$ ) H I 21-cm optical depth measurements at low- $z$  by a factor  $\sim 3$ . We have detected H I 21-cm absorption from seven QGPs in our primary sample, two of which are reported here for the first time. The H I 21-cm detections from our survey have increased the existing number of detections from  $z < 0.4$  QGPs by almost a factor of two. Combining our primary sample with measurements from the literature having similar optical depth sensitivity, we have quantified the H I 21-cm optical depth and covering factor of H I 21-cm absorbers as a function of spatial location around low- $z$  galaxies. Below we list our main results.

- The H I 21-cm optical depth and impact parameter are weakly anti-correlated. Performing survival analysis by including the upper limits as censored data points, we obtain,  $r_k = -0.20$ ,  $P(r_k) = 0.01$ ,  $S(r_k) = 2.42\sigma$ . Similar anti-correlation is also present between  $\int \tau dv$  and the radial distance along the galaxy’s major axis, as well the impact parameter and the radial distance scaled with the effective H I radius of the galaxies.

- We find that the covering factor of H I 21-cm absorbers is  $0.24^{+0.12}_{-0.08}$  at  $b \leq 15$  kpc and decreases to  $0.06^{+0.09}_{-0.04}$  at  $b = 15$ – $35$  kpc when we use  $\tau_0 = 0.3 \text{ km s}^{-1}$ . The average  $C_{21}$  within  $b = 30$  kpc is  $0.16^{+0.07}_{-0.05}$ .  $C_{21}$  shows similar declining trend with increasing scaled  $b$ ,  $R$  and scaled  $R$ .

- The H I 21-cm optical depth shows weak anti-correlation ( $r_k = -0.17$ ,  $P(r_k) = 0.07$ ,  $S(r_k) = 1.79\sigma$ ) with the azimuthal orientation of the radio sightline with respect to the galaxy’s major axis. There is similar weak correlation between  $\int \tau dv$  and  $\sin(i)\cos(\phi)$ , i.e.  $\int \tau dv$  shows mild increase with increasing galaxy inclination and decreasing orientation. However, these could

be driven by the stronger and more significant anti-correlation of  $\int \tau dv$  with  $b$ , since these parameters are correlated with  $b$  in our sample.

- We find that  $C_{21}$  is  $0.20^{+0.14}_{-0.09}$  near the galaxy major axis ( $\phi < 45^\circ$ ) and  $0.04^{+0.09}_{-0.03}$  near the minor axis ( $\phi \geq 45^\circ$ ), and this declining trend of  $C_{21}$  with increasing  $\phi$  is also seen at  $b < 15$  kpc. This tentative indication that most of the H I 21-cm absorbers could be co-planar with that of the H I disk is supported by the fact that the only two H I 21-cm detections at  $b \geq 15$  kpc in the Combined sample arise from face-on galaxies. Further,  $C_{21}$  is maximum ( $0.31^{+0.24}_{-0.15}$ ) for sightlines that pass near the major axis of edge-on galaxies ( $i \geq 58^\circ$ ). If this is true even for high- $z$  galaxies, then it will have important implications for the detection rate of H I 21-cm absorption towards Mg II absorbers, which are found to be typically tracing the halo gas and not the extended H I disks. However, high- $z$  galaxies are not expected to have such well-formed H I disks, but to be more irregular. Hence, the dependence of H I 21-cm absorption on galaxy orientation needs to be probed over a larger redshift range.

- No significant dependence of  $\int \tau dv$  and  $C_{21}$  on galaxy luminosity, stellar mass, colour and surface star formation rate density is found from the present data. However, our results suggest that the H I 21-cm absorbing gas cross-section may be larger for the brighter galaxies. A correlation between  $\int \tau dv$  and  $C_{21}$  and properties associated with star formation in galaxies are expected from the models of ISM as discussed in Section 1. Hence, it appears that most of our sightlines are outside the stellar disks of galaxies and probably tracing the outer quiescent regions that are not affected by the ongoing star formation activities.

- No correlation is found between H I 21-cm optical depth and  $W_r(\text{Ca II})$  or  $W_r(\text{Na I})$ . We also find that  $W_r(\text{Ca II})$  and the ratio  $W_r(\text{Na I})/W_r(\text{Ca II})$  suggests that most of the H I 21-cm absorbers observed around low- $z$  galaxies are not tracing the dusty star-forming disks.

- From the data available in the literature, we find that the covering factor of H I 21-cm absorption from host galaxies of  $z < 1$  DLAs ( $0.62^{+0.30}_{-0.21}\%$ ) is a factor of  $\sim 4$  times higher compared to that from the galaxy-selected QGPs. There is also no correlation between  $\int \tau dv$  and  $b$  for DLAs. This result is analogous to the finding that the covering factor of Mg II gaseous halos around galaxies is close to 1 when one searches for galaxies around Mg II absorbers (see Bergeron & Boissé 1991; Steidel 1995), and is lower when one searches for Mg II absorption along sightlines close to known galaxies (see Bechtold & Ellingson 1992; Tripp & Bowen 2005). Broadly, we can conclude that the H I distribution around galaxies that can contribute to the DLA population is patchy (i.e. with a covering factor of about 30%) and about 60% of the DLAs have cold gas that can produce detectable H I 21-cm absorption. Such a picture will be consistent with the observed covering factors of DLAs and H I 21-cm absorbers around galaxies and fraction of DLAs producing H I 21-cm absorption.

- We estimate  $n_{21}$  at  $z = 0.1$  as  $0.008^{+0.005}_{-0.004}$  from our QGP observations. This is lower than what has been found from the high- $z$  Mg II absorbers and DLAs. This along with the observed redshift evolution of galaxy size and luminosity may suggest an evolution in the correlation between optical luminosity and the extent of the H I gas around galaxies with redshift.

## ACKNOWLEDGEMENTS

We thank the staff at GMRT, VLA, WSRT and SALT for their help during the observations. GMRT is run by the National Centre for Radio Astrophysics of the Tata Institute of Fundamental Research. The VLA is run by the National Radio Astronomy Observatory (NRAO). The NRAO is a facility of the National Science Foundation operated under cooperative agreement by Associated Universities, Inc. The WSRT is operated by the ASTRON (Netherlands Foundation for Research in Astronomy) with support from the Netherlands Foundation for Scientific Research (NWO). Some of the observations reported in this paper were obtained with the Southern African Large Telescope (SALT). NG, PN, RS and PPJ acknowledge the support from Indo-Fench centre for the promotion of Advanced Research (IFCPAR) under Project No. 5504-2. We thank the referee for his/her detailed and useful comments. This research has made use of the NASA/IPAC Extragalactic Database (NED) which is operated by the Jet Propulsion Laboratory, California Institute of Technology, under contract with the National Aeronautics and Space Administration. Funding for SDSS-III has been provided by the Alfred P. Sloan Foundation, the Participating Institutions, the National Science Foundation, and the U.S. Department of Energy Office of Science. The SDSS-III web site is <http://www.sdss3.org/>. SDSS-III is managed by the Astrophysical Research Consortium for the Participating Institutions of the SDSS-III Collaboration including the University of Arizona, the Brazilian Participation Group, Brookhaven National Laboratory, Carnegie Mellon University, University of Florida, the French Participation Group, the German Participation Group, Harvard University, the Instituto de Astrofísica de Canarias, the Michigan State/Notre Dame/JINA Participation Group, Johns Hopkins University, Lawrence Berkeley National Laboratory, Max Planck Institute for Astrophysics, Max Planck Institute for Extraterrestrial Physics, New Mexico State University, New York University, Ohio State University, Pennsylvania State University, University of Portsmouth, Princeton University, the Spanish Participation Group, University of Tokyo, University of Utah, Vanderbilt University, University of Virginia, University of Washington, and Yale University.

## REFERENCES

- Alam, S., Albareti, F. D., Allende Prieto, C., et al., 2015, *ApJS*, 219, 12
- Allison, J. R., Sadler, E. M., Moss, V. A., et al., 2015, *MNRAS*, 453, 1249
- Allison, J. R., Zwaan, M. A., Duchesne, S. W., & Curran, S. J., 2016, *MNRAS*, 462, 1341
- Argence, B. & Lamareille, F., 2009, *A&A*, 495, 759
- Bagetakos, I., Brinks, E., Walter, F., de Blok, W. J. G., Usero, A., Leroy, A. K., Rich, J. W., & Kennicutt, Jr., R. C., 2011, *AJ*, 141, 23
- Bahcall, J. N. & Ekers, R. D., 1969, *ApJ*, 157, 1055
- Bechtold, J. & Ellingson, E., 1992, *ApJ*, 396, 20
- Begum, A., Chengalur, J. N., Karachentsev, I. D., Sharina, M. E., & Kaisin, S. S., 2008, *MNRAS*, 386, 1667
- Bergeron, J. & Boissé, P., 1991, *A&A*, 243, 344
- Best, P. N., Arts, J. N., Röttgering, H. J. A., Rengelink, R., Brookes, M. H., & Wall, J., 2003, *MNRAS*, 346, 627
- Biggs, A. D., Zwaan, M. A., Hatziminaoglou, E., Péroux, C., & Liske, J., 2016, *MNRAS*, 462, 2819
- Bigiel, F., Leroy, A., Walter, F., Blitz, L., Brinks, E., de Blok, W. J. G., & Madore, B., 2010, *AJ*, 140, 1194



- Blanton, M. R. & Berlind, A. A., 2007, *ApJ*, 664, 791
- Blanton, M. R., Hogg, D. W., Bahcall, N. A., et al., 2003, *ApJ*, 592, 819
- Blanton, M. R. & Roweis, S., 2007, *AJ*, 133, 734
- Bohlin, R. C., Savage, B. D., & Drake, J. F., 1978, *ApJ*, 224, 132
- Boisse, P., Dickey, J. M., Kazes, I., & Bergeron, J., 1988, *A&A*, 191, 193
- Bordoloi, R., Lilly, S. J., Kacprzak, G. G., & Churchill, C. W., 2014, *ApJ*, 784, 108
- Borthakur, S., 2016, *ApJ*, 829, 128
- Borthakur, S., Heckman, T., Tumlinson, J., et al., 2015, *ApJ*, 813, 46
- Borthakur, S., Momjian, E., Heckman, T. M., York, D. G., Bowen, D. V., Yun, M. S., & Tripp, T. M., 2014, *ApJ*, 795, 98
- Borthakur, S., Tripp, T. M., Yun, M. S., Bowen, D. V., Meiring, J. D., York, D. G., & Momjian, E., 2011, *ApJ*, 727, 52
- Borthakur, S., Tripp, T. M., Yun, M. S., Momjian, E., Meiring, J. D., Bowen, D. V., & York, D. G., 2010, *ApJ*, 713, 131
- Bouché, N., Hohensee, W., Vargas, R., Kacprzak, G. G., Martin, C. L., Cooke, J., & Churchill, C. W., 2012, *MNRAS*, 426, 801
- Briggs, F. H. & Wolfe, A. M., 1983, *ApJ*, 268, 76
- Broeils, A. H. & Rhee, M.-H., 1997, *A&A*, 324, 877
- Brookes, M. H., Best, P. N., Peacock, J. A., Röttgering, H. J. A., & Dunlop, J. S., 2008, *MNRAS*, 385, 1297
- Brookes, M. H., Best, P. N., Rengelink, R., & Röttgering, H. J. A., 2006, *MNRAS*, 366, 1265
- Buitrago, F., Trujillo, I., Conselice, C. J., Bouwens, R. J., Dickinson, M., & Yan, H., 2008, *ApJ*, 687, L61
- Carilli, C. L. & van Gorkom, J. H., 1992, *ApJ*, 399, 373
- Catinella, B. & Cortese, L., 2015, *MNRAS*, 446, 3526
- Chen, H.-W., Lanzetta, K. M., Webb, J. K., & Barcons, X., 2001, *ApJ*, 559, 654
- Chen, H.-W., Wild, V., Tinker, J. L., Gauthier, J.-R., Helsby, J. E., Shectman, S. A., & Thompson, I. B., 2010, *ApJ*, 724, L176
- Chung, A., van Gorkom, J. H., Kenney, J. D. P., Crowl, H., & Vollmer, B., 2009, *AJ*, 138, 1741
- Churchill, C. W., Nielsen, N. M., Kacprzak, G. G., & Trujillo-Gomez, S., 2013, *ApJ*, 763, L42
- Corbelli, E. & Schneider, S. E., 1990, *ApJ*, 356, 14
- Crawford, S. M., Still, M., Schellart, P., et al., 2010, in *Proc. SPIE*, Vol. 7737, *Observatory Operations: Strategies, Processes, and Systems III*, p. 773725
- Curran, S. J., Murphy, M. T., Pihlström, Y. M., Webb, J. K., & Purcell, C. R., 2005, *MNRAS*, 356, 1509
- Curran, S. J., Reeves, S. N., Allison, J. R., & Sadler, E. M., 2016, *MNRAS*, 459, 4136
- Curran, S. J., Tzanavaris, P., Darling, J. K., Whiting, M. T., Webb, J. K., Bignell, C., Athreya, R., & Murphy, M. T., 2010, *MNRAS*, 402, 35
- Dahlen, T., Mobasher, B., Dickinson, M., Ferguson, H. C., Gialalisco, M., Kretchmer, C., & Ravindranath, S., 2007, *ApJ*, 654, 172
- Darling, J., Macdonald, E. P., Haynes, M. P., & Giovanelli, R., 2011, *ApJ*, 742, 60
- de Blok, W. J. G., Walter, F., Brinks, E., Trachternach, C., Oh, S.-H., & Kennicutt, Jr., R. C., 2008, *AJ*, 136, 2648
- DeBoer, D. R., Gough, R. G., Bunton, J. D., et al., 2009, *IEEE Proceedings*, 97, 1507
- Dutta, P., Chengalur, J. N., Roy, N., Goss, W. M., Arjunwadkar, M., Minter, A. H., Brogan, C. L., & Lazio, T. J. W., 2014, *MNRAS*, 442, 647
- Dutta, R., Gupta, N., Srianand, R., & O'Meara, J. M., 2016, *MNRAS*, 456, 4209
- Elmegreen, B. G. & Hunter, D. A., 2015, *ApJ*, 805, 145
- Epinat, B., Amram, P., Marcelin, M., et al., 2008, *MNRAS*, 388, 500
- Fernández, X., Gim, H. B., van Gorkom, J. H., et al., 2016, *ApJ*, 824, L1
- Field, G. B., 1959, *ApJ*, 129, 536
- Gabasch, A., Bender, R., Seitz, S., et al., 2004, *A&A*, 421, 41
- Gehrels, N., 1986, *ApJ*, 303, 336
- Greisen, E. W., Spekkens, K., & van Moorsel, G. A., 2009, *AJ*, 137, 4718
- Gupta, N., Srianand, R., Bowen, D. V., York, D. G., & Wadadekar, Y., 2010, *MNRAS*, 408, 849
- Gupta, N., Srianand, R., Noterdaeme, P., Petitjean, P., & Muzahid, S., 2013, *A&A*, 558, A84
- Gupta, N., Srianand, R., Petitjean, P., Bergeron, J., Noterdaeme, P., & Muzahid, S., 2012, *A&A*, 544, A21
- Gupta, N., Srianand, R., Petitjean, P., Noterdaeme, P., & Saikia, D. J., 2009, *MNRAS*, 398, 201
- Haschick, A. D. & Burke, B. F., 1975, *ApJ*, 200, L137
- Haynes, M. P., Giovanelli, R., & Roberts, M. S., 1979, *ApJ*, 229, 83
- Heiles, C. & Troland, T. H., 2003, *ApJ*, 586, 1067
- Hwang, C.-Y. & Chiou, S.-H., 2004, *ApJ*, 600, 52
- Ianjamasimanana, R., de Blok, W. J. G., Walter, F., & Heald, G. H., 2012, *AJ*, 144, 96
- Ilbert, O., Tresse, L., Zucca, E., et al., 2005, *A&A*, 439, 863
- Jiang, P., Ge, J., Zhou, H., Wang, J., & Wang, T., 2011, *ApJ*, 732, 110
- Jonas, J. L., 2009, *IEEE Proceedings*, 97, 1522
- Kacprzak, G. G., Churchill, C. W., Barton, E. J., & Cooke, J., 2011, *ApJ*, 733, 105
- Kacprzak, G. G., Churchill, C. W., & Nielsen, N. M., 2012, *ApJ*, 760, L7
- Kacprzak, G. G., Churchill, C. W., Steidel, C. C., & Murphy, M. T., 2008, *AJ*, 135, 922
- Kanekar, N., Athreya, R. M., & Chengalur, J. N., 2002, *A&A*, 382, 838
- Kanekar, N. & Chengalur, J. N., 2003, *A&A*, 399, 857
- Kanekar, N., Prochaska, J. X., Smette, A., et al., 2014, *MNRAS*, 438, 2131
- Keeney, B. A., Momjian, E., Stocke, J. T., Carilli, C. L., & Tumlinson, J., 2005, *ApJ*, 622, 267
- Keeney, B. A., Stocke, J. T., Danforth, C. W., & Carilli, C. L., 2011, *AJ*, 141, 66
- Kennicutt, Jr., R. C., 1998a, *ARA&A*, 36, 189
- , 1998b, *ApJ*, 498, 541
- Kewley, L. J., Geller, M. J., & Jansen, R. A., 2004, *AJ*, 127, 2002
- Khare, P., vanden Berk, D., York, D. G., Lundgren, B., & Kulkarni, V. P., 2012, *MNRAS*, 419, 1028
- Krogager, J.-K., Fynbo, J. P. U., Møller, P., Ledoux, C., Noterdaeme, P., Christensen, L., Milvang-Jensen, B., & Sparre, M., 2012, *MNRAS*, 424, L1
- Kulkarni, S. R. & Heiles, C., 1988, Neutral hydrogen and the diffuse interstellar medium, Kellermann, K. I. & Verschuur, G. L., eds., pp. 95–153
- Lah, P., Pracy, M. B., Chengalur, J. N., et al., 2009, *MNRAS*, 399, 1447
- Le Brun, V., Smette, A., Surdej, J., & Claeskens, J.-F., 2000, *A&A*, 363, 837
- Liszt, H., 2001, *A&A*, 371, 698

- McKee, C. F. & Ostriker, J. P., 1977, *ApJ*, 218, 148
- Mihos, J. C., Keating, K. M., Holley-Bockelmann, K., Pisano, D. J., & Kassim, N. E., 2012, *ApJ*, 761, 186
- Miller, N. A., Hornschemeier, A. E., & Mobasher, B., 2009, *AJ*, 137, 4436
- Morganti, R., Sadler, E. M., & Curran, S., 2015, *Advancing Astrophysics with the Square Kilometre Array (AASKA14)*, 134
- Muzahid, S., Srianand, R., & Charlton, J., 2015, *MNRAS*, 448, 2840
- Neeleman, M., Prochaska, J. X., Ribaud, J., Lehner, N., Howk, J. C., Rafelski, M., & Kanekar, N., 2016, *ApJ*, 818, 113
- Nielsen, N. M., Churchill, C. W., Kacprzak, G. G., & Murphy, M. T., 2013, *ApJ*, 776, 114
- Nielsen, N. M., Churchill, C. W., Kacprzak, G. G., Murphy, M. T., & Evans, J. L., 2015, *ApJ*, 812, 83
- Noterdaeme, P., Petitjean, P., Ledoux, C., & Srianand, R., 2009, *A&A*, 505, 1087
- Noterdaeme, P., Srianand, R., & Mohan, V., 2010, *MNRAS*, 403, 906
- Oosterloo, T., Fraternali, F., & Sancisi, R., 2007, *AJ*, 134, 1019
- Péroux, C., Bouché, N., Kulkarni, V. P., York, D. G., & Vladilo, G., 2012, *MNRAS*, 419, 3060
- Poznanski, D., Prochaska, J. X., & Bloom, J. S., 2012, *MNRAS*, 426, 1465
- Prochaska, J. X., Weiner, B., Chen, H.-W., Mulchaey, J., & Cooksey, K., 2011, *ApJ*, 740, 91
- Rafelski, M., Wolfe, A. M., & Chen, H.-W., 2011, *ApJ*, 736, 48
- Rahmani, H., Péroux, C., Turnshek, D. A., et al., 2016, *MNRAS*, 463, 980
- Rao, S. M., Belfort-Mihalyi, M., Turnshek, D. A., Monier, E. M., Nestor, D. B., & Quider, A., 2011, *MNRAS*, 416, 1215
- Rao, S. M., Turnshek, D. A., & Nestor, D. B., 2006, *ApJ*, 636, 610
- Reeves, S. N., Sadler, E. M., Allison, J. R., Koribalski, B. S., Curran, S. J., & Pracy, M. B., 2015, *MNRAS*, 450, 926
- Reeves, S. N., Sadler, E. M., Allison, J. R., et al., 2016, *MNRAS*, 457, 2613
- Reid, R. I., Kronberg, P. P., & Perley, R. A., 1999, *ApJS*, 124, 285
- Richter, P., Krause, F., Fechner, C., Charlton, J. C., & Murphy, M. T., 2011, *A&A*, 528, A12
- Rosenberg, J. L. & Schneider, S. E., 2002, *ApJ*, 567, 247
- Roy, N., Chengalur, J. N., & Srianand, R., 2006, *MNRAS*, 365, L1
- Roy, N., Minter, A. H., Goss, W. M., Brogan, C. L., & Lazio, T. J. W., 2012, *ApJ*, 749, 144
- Sancisi, R., Fraternali, F., Oosterloo, T., & van der Hulst, T., 2008, *A&A Rev.*, 15, 189
- Sardane, G. M., Turnshek, D. A., & Rao, S. M., 2015, *MNRAS*, 452, 3192
- Schaye, J., Carswell, R. F., & Kim, T.-S., 2007, *MNRAS*, 379, 1169
- Schneider, S. E. & Corbelli, E., 1993, *ApJ*, 414, 500
- Schombert, J. M., Pildis, R. A., & Eder, J. A., 1997, *ApJS*, 111, 233
- Snow, T. P. & McCall, B. J., 2006, *ARA&A*, 44, 367
- Srianand, R., Gupta, N., Momjian, E., & Vivek, M., 2015, *MNRAS*, 451, 917
- Srianand, R., Gupta, N., Petitjean, P., Noterdaeme, P., Ledoux, C., Salter, C. J., & Saikia, D. J., 2012, *MNRAS*, 421, 651
- Srianand, R., Gupta, N., Petitjean, P., Noterdaeme, P., & Saikia, D. J., 2008, *MNRAS*, 391, L69
- Srianand, R., Gupta, N., Rahmani, H., Momjian, E., Petitjean, P., & Noterdaeme, P., 2013, *MNRAS*, 428, 2198
- Stanghellini, C., O’Dea, C. P., Dallacasa, D., Baum, S. A., Fanti, R., & Fanti, C., 1998, *A&AS*, 131, 303
- Stanimirović, S., Weisberg, J. M., Pei, Z., Tuttle, K., & Green, J. T., 2010, *ApJ*, 720, 415
- Steidel, C. C., 1995, in *QSO Absorption Lines*, Meylan, G., ed., p. 139
- Stocke, J. T., Keeney, B. A., & Danforth, C. W., 2010, *PASA*, 27, 256
- Stocke, J. T., Keeney, B. A., Danforth, C. W., Shull, J. M., Froning, C. S., Green, J. C., Penton, S. V., & Savage, B. D., 2013, *ApJ*, 763, 148
- Straka, L. A., Whichard, Z. L., Kulkarni, V. P., Bishof, M., Bowen, D., Khare, P., & York, D. G., 2013, *MNRAS*, 436, 3200
- Tamburro, D., Rix, H.-W., Leroy, A. K., Mac Low, M.-M., Walter, F., Kennicutt, R. C., Brinks, E., & de Blok, W. J. G., 2009, *AJ*, 137, 4424
- Toribio, M. C., Solanes, J. M., Giovanelli, R., Haynes, M. P., & Martin, A. M., 2011, *ApJ*, 732, 93
- Tripp, T. M. & Bowen, D. V., 2005, in *IAU Colloq. 199: Probing Galaxies through Quasar Absorption Lines*, Williams, P., Shu, C.-G., & Menard, B., eds., pp. 5–23
- Trujillo, I., Conselice, C. J., Bundy, K., Cooper, M. C., Eisenhardt, P., & Ellis, R. S., 2007, *MNRAS*, 382, 109
- Tumlinson, J., Thom, C., Werk, J. K., et al., 2013, *ApJ*, 777, 59
- Turnshek, D. A., Rao, S., Nestor, D., Lane, W., Monier, E., Bergeron, J., & Smette, A., 2001, *ApJ*, 553, 288
- van der Hulst, J. M., van Albada, T. S., & Sancisi, R., 2001, in *Astronomical Society of the Pacific Conference Series*, Vol. 240, *Gas and Galaxy Evolution*, Hibbard, J. E., Rupen, M., & van Gorkom, J. H., eds., p. 451
- van der Wel, A., Franx, M., van Dokkum, P. G., et al., 2014, *ApJ*, 788, 28
- van Dishoeck, E. F. & Black, J. H., 1989, *ApJ*, 340, 273
- Vanden Berk, D. E., Richards, G. T., Bauer, A., et al., 2001, *AJ*, 122, 549
- Verheijen, M., van Gorkom, J. H., Szomoru, A., Dwarakanath, K. S., Poggianti, B. M., & Schiminovich, D., 2007, *ApJ*, 668, L9
- Verheijen, M. A. W., Oosterloo, T. A., van Cappellen, W. A., Bakker, L., Ivashina, M. V., & van der Hulst, J. M., 2008, in *American Institute of Physics Conference Series*, Vol. 1035, *The Evolution of Galaxies Through the Neutral Hydrogen Window*, Minchin, R. & Momjian, E., eds., pp. 265–271
- Wakker, B. P. & Mathis, J. S., 2000, *ApJ*, 544, L107
- Walter, F., Brinks, E., de Blok, W. J. G., Bigiel, F., Kennicutt, Jr., R. C., Thornley, M. D., & Leroy, A., 2008, *AJ*, 136, 2563
- Welty, D. E., Morton, D. C., & Hobbs, L. M., 1996, *ApJS*, 106, 533
- White, R. L., Becker, R. H., Helfand, D. J., & Gregg, M. D., 1997, *ApJ*, 475, 479
- Wild, V., Hewett, P. C., & Pettini, M., 2006, *MNRAS*, 367, 211
- Wolfe, A. M., Gawiser, E., & Prochaska, J. X., 2005, *ARA&A*, 43, 861
- Wolfe, A. M., Prochaska, J. X., & Gawiser, E., 2003, *ApJ*, 593, 215
- Wolfire, M. G., Hollenbach, D., McKee, C. F., Tielens, A. G. G. M., & Bakes, E. L. O., 1995, *ApJ*, 443, 152
- Womble, D. S., 1993, *PASP*, 105, 1043
- Wu, X.-B., Hao, G., Jia, Z., Zhang, Y., & Peng, N., 2012, *AJ*, 144, 49
- Wu, Z., Haynes, M. P., Giovanelli, R., Zhu, M., & Chen, R., 2015, *Chinese Astron. Astrophys.*, 39, 466
- York, D. G., Adelman, J., Anderson, Jr., J. E., et al., 2000, *AJ*,

120, 1579

York, D. G., Khare, P., Vanden Berk, D., et al., 2006, MNRAS, 367, 945

York, D. G., Straka, L. A., Bishof, M., et al., 2012, MNRAS, 423, 3692

Zwaan, M. A., Liske, J., Péroux, C., Murphy, M. T., Bouché, N., Curran, S. J., & Biggs, A. D., 2015, MNRAS, 453, 1268

Zwaan, M. A., van der Hulst, J. M., Briggs, F. H., Verheijen, M. A. W., & Ryan-Weber, E. V., 2005, MNRAS, 364, 1467

Zwaan, M. A., van Dokkum, P. G., & Verheijen, M. A. W., 2001, Science, 293, 1800

## **APPENDIX A: SAMPLE PROPERTIES**

Properties of the QGPs observed by us as described in Section 2.3 are provided here.

**Table A1.** Details of the QGPs observed by us.

QGP	Radio Source	$z_{\text{rad}}$	Type	Mor.	Galaxy	$z_{\text{gal}}$	$z_{\text{gal}}$ Source	$g - r$	$\log M_*$ ( $M_{\odot}$ )	$\log L_B$ ( $L_{\odot}$ )	$b$ (kpc)	$i$ ( $^{\circ}$ )	$\phi$ ( $^{\circ}$ )
(1)	(2)	(3)	(4)	(5)	(6)	(7)	(8)	(9)	(10)	(11)	(12)	(13)	(14)
<i>Primary Sample</i>													
J0041–0143N	J004126.11–014305.6	1.679	Q	R	J004121.53–014257.0	0.01769	1	0.58	10.5	10.4	25.0	15	—
J0041–0143C	J004126.01–014314.6			R							25.0		—
J0041–0143S	J004125.98–014324.6			R							26.0		—
J0043+0024	J004332.71+002459.9	1.127	Q	C	J004333.64+002516.2	0.07975	2	0.39	9.6	9.9	32.3	27	—
J0134+0003	J013412.70+000345.2	0.879	Q	C	J013411.28+000327.5	0.05198	2	0.44	9.8	9.9	28.1	58	52
J0802+1601	J080240.89+160104.6	1.784	Q	C	J080241.68+160035.2	0.01565	2	0.43	8.8	9.0	10.1	34	45
J0817+1958	J081705.49+195842.8	5.154	Q	C	J081707.13+195907.9	0.04363	2	0.74	10.8	10.4	29.3	38	43
J0821+5031	J082153.82+503120.4	2.123	Q	C	J082153.74+503125.7	0.1835	3	0.23	9.4	10.1	16.5	38	28
J0849+5108_1	J084957.97+510829.0	0.584	Q	C	J084957.49+510842.3	0.07342	2	0.46	10.5	10.6	19.6	46	16
J0849+5108_2	J084957.97+510829.0	0.584	Q	C	J084958.10+510826.6	0.3120	3	1.65	10.4	9.7	12.3	0	—
J0856+1020	J085624.91+102017.0	3.701	Q	C	J085625.41+102020.1	0.1043	4	0.45	10.1	10.2	15.3	36	51
J0911+1958	J091133.45+195814.1	1.635	Q	C	J091134.38+195830.2	0.02293	5	0.39	8.7	9.0	9.6	58	84
J1015+1637	J101514.63+163740.4	$\geq 0.5^a$	U	C	J101514.22+163758.3	0.05436	2	0.43	9.5	9.8	19.9	58	40
J1110+0321E	J111022.59+032133.5	0.965	Q	R	J111025.09+032138.8	0.02996	2	0.49	9.7	9.8	15.4	39	47
J1110+0321W	J111022.97+032130.5			R							22.7		53
J1126+3802	J112613.04+380216.4	0.515 <sup>b</sup>	U	C	J112612.57+380228.6	0.06190	2	0.57	10.1	10.0	16.0	60	70
J1133+0015_1	J113303.02+001549.0	1.171	Q	C	J113302.01+001541.7	0.0762	4	0.49	10.0	10.0	24.3	28	—
J1133+0015_2	J113303.02+001549.0	1.171	Q	C	J113303.96+001538.2	0.07584	2	0.76	10.6	10.2	25.6	60	64
J1156+3412	J115659.62+341216.9	$\geq 0.5^a$	G	R	J115659.59+341221.7	0.13797	2	0.59	10.6	10.5	11.7	46	27
J1209+4119	J120922.78+411941.3	1.364	Q	C	J120923.25+411949.3	0.17098	2	0.73	10.7	10.4	27.9	53	66
J1228+3706	J122847.42+370612.0	1.517	Q	C	J122847.72+370606.9	0.13837	2	0.64	10.6	10.4	15.2	26	—
J1241+6332	J124157.54+633241.6	2.613	Q	C	J124157.26+633237.6	0.1430	6	0.37	10.3	10.6	11.1	66	19
J1243+4043	J124355.78+404358.4	1.520	Q	C	J124357.17+404346.1	0.01693	2	0.47	9.6	9.6	6.9	77	26
J1243+1622N	J124357.79+162246.3	0.555	Q	R	J124342.64+162335.9	0.00263	7	0.77	9.8	9.4	12.2	47	25
J1243+1622C	J124357.79+162252.3			R							12.1		24
J1243+1622S	J124357.51+162301.3			R							11.8		22
J1254+0546	J125422.19+054619.8	2.252	Q	C	J125422.21+054610.4	0.0246	4	0.21	7.8	8.5	4.7	69	6
J1300+2830	J130028.53+283010.1	0.647	Q	C	J130028.66+283012.1	0.2229	6	0.47	9.8	9.9	9.4	71	30
J1300–0121	J130050.09–012146.2	$\geq 0.5^a$	U	R	J130049.15–012136.4	0.02275	2	0.29	8.3	9.1	7.9	70	60
J1345+0347	J134528.74+034719.7	0.825	Q	C	J134528.42+034723.0	0.2622	4	0.77	11.0	10.5	23.5	70	25
J1359+2935	J135907.77+293531.8	0.225 <sup>b</sup>	U	R	J135908.47+293541.5	0.14607	2	0.76	10.9	10.5	34.0	36	85
J1422+0540	J142253.22+054013.4	0.618 <sup>b</sup>	G	C	J142253.99+053947.9	0.05422	2	0.79	10.4	9.9	29.5	70	55
J1438+1758	J143806.79+175805.4	2.031	Q	C	J143806.76+175802.5	0.1468	6	0.34	9.0	9.3	7.5	76	6
J1443+0214	J144304.53+021419.3	1.820	Q	C	J144304.53+021419.3	0.3714	6	—	—	—	<5.1	—	—
J1457+0519	J145722.53+051921.8	3.174	Q	C	J145722.40+051918.8	0.2198	2	0.29	9.4	10.1	12.7	29	—
J1525+4201	J152523.55+420117.0	1.195	Q	R	J152522.99+420131.7	0.09094	4	0.68	10.7	10.4	27.1	38	60
J1539+0534	J153905.20+053438.3	1.509	Q	R	J153905.16+053416.5	0.02594	2	0.70	10.7	10.4	11.4	18	—
J1551+0713	J155121.13+071357.7	0.675	Q	C	J155121.06+071352.4	0.1007	4	0.79	10.8	10.3	10.0	24	—

Table A1. Continued from previous page.

QGP	Radio Source	$z_{\text{rad}}$	Type	Mor.	Galaxy	$z_{\text{gal}}$	$z_{\text{gal}}$ Source	$g - r$	$\log M_*$ ( $M_\odot$ )	$\log L_B$ ( $L_\odot$ )	$b$ (kpc)	$i$ ( $^\circ$ )	$\phi$ ( $^\circ$ )
(1)	(2)	(3)	(4)	(5)	(6)	(7)	(8)	(9)	(10)	(11)	(12)	(13)	(14)
J1606+2717	J160658.29+271705.5	0.933	Q	R	J160659.13+271642.6	0.04620	2	0.35	9.3	9.7	23.1	66	71
J1634+3900	J163402.95+390000.5	1.083	Q	C	J163403.30+390001.0	0.36620	8	0.64	10.2	10.0	20.9	49	69
J1639+1127	J163956.35+112758.7	0.994	Q	C	J163956.37+112802.1	0.0790	6	0.49	9.8	9.9	5.1	65	3
J1643+3547	J164315.58+354729.7	0.224 <sup>b</sup>	G	R	J164315.10+354701.6	0.03121	2	0.65	9.9	9.7	17.9	55	23
J1648+2429	J164802.37+242916.9	0.791	Q	C	J164804.38+242935.3	0.03583	2	0.75	10.0	9.6	23.5	38	46
J1748+7005	J174832.84+700550.8	0.770	Q	C	J174926.43+700839.7	0.00008	7	—	—	9.2	10.3	70	44
J2240–0836	J224013.41–083628.7	0.581	Q	C	J224013.49–083633.6	0.2111	4	0.84	10.8	10.3	17.4	62	84
<i>Supplementary Sample</i>													
J0820+0826	J082015.85+082612.6	0.686	Q	C	J082015.88+082610.5	0.07750	9	1.63	8.5	7.5	3.1	—	—
J0919+3400E	J091917.07+340049.5	0.108 <sup>b</sup>	U	R	J091917.45+340029.4	0.02376	2	0.73	10.6	10.2	9.9	60	45
J0919+3400W	J091914.80+340051.4	—	—	R	—	—	—	—	—	—	19.0	—	90
J0947+1113	J094745.85+111354.0	1.774	U	C	J094745.85+111354.0	0.11240	9	—	—	—	4.1	—	—
J0954+3733	J095433.96+373336.3	—	U	C	J095432.89+373333.1	0.07282	2	0.45	10.1	10.2	18.2	50	1
J0956+1614N	J095604.27+161420.5	—	U	R	J095604.09+161427.1	0.03346	2	0.49	9.3	9.4	4.7	37	37
J0956+1614S	J095604.20+161417.0	—	—	R	—	—	—	—	—	—	6.8	—	23
J1050+0002	J105053.93+000213.6	0.662	Q	C	J105053.93+000213.6	0.23380	9	—	—	—	7.4	—	—
J1359+2708	J135947.90+270828.3	1.832	Q	C	J135947.90+270828.3	0.04320	9	—	—	—	1.7	—	—
J1438+0920	J143809.90+092016.9	—	U	R	J143810.20+092009.8	0.03029	2	0.81	11.1	10.6	5.1	29	—
J1624+2328	J162434.18+232859.9	0.230	Q	C	J162433.76+232912.3	0.09382	2	0.50	10.3	10.3	23.8	29	—
J2242–0019	J224247.89–001944.9	0.405	Q	C	J224247.65–001918.7	0.05815	2	0.79	10.7	10.3	29.8	75	46
<i>Miscellaneous Sample</i>													
J0846+0704	J084600.36+070424.6	0.342	Q	R	J084600.52+070428.8	0.34120	2	0.79	10.4	9.9	23.5	9	—
J0942+0623	J094221.98+062335.2	0.123	G	C	J094221.94+062337.1	0.12390	2	0.54	10.5	10.4	4.4	53	41
J1214+2931	J121417.80+293143.4	0.063	Q	R	J121418.25+293146.7	0.06326	2	0.78	11.0	10.6	8.2	47	7
J1643+2419	J164330.03+241951.8	0.087	G	R	J164331.92+241939.6	0.08723	2	0.53	10.9	10.9	37.1	29	—
J2054+0041	J205449.61+004153.0	0.284 <sup>b</sup>	G	C	J205449.64+004149.8	0.20153	2	0.53	10.2	10.1	10.7	36	21

Column 1: QGP name; in case of multiple radio sightlines for the same QGP, the name is suffixed with N, S, E, W or C (denoting north, south, east, west and centre, respectively) to indicate the radio sightline; in case of two galaxies around the same radio sightline, the name is suffixed with \_1 and \_2 to differentiate the two QGPs. Column 2: Radio source name. Column 3: Redshift of radio source. Column 4: Type of radio source – quasar (Q), radio galaxy (G) or unknown (U). Column 5: Morphology of radio source at arcsecond-scale – compact (C) or resolved (R). Column 6: Galaxy name. Column 7: Galaxy redshift. Column 8: Source of galaxy redshift – 1: Jonas (2009); 2: SDSS; 3: APO observations (Gupta et al. 2009); 4: SALT observations (this work); 5: Schombert et al. (1997); 6: identified by us as GOTOQ; 7: Epinat et al. (2008); 8: Womble (1993); 9: Ca II absorption identified by us in SDSS quasar spectra. Column 9: Rest-frame SDSS  $g - r$  colour of galaxy. Column 10: Log of stellar mass ( $M_\odot$ ) of galaxy from *kcorrect* (Blanton & Roweis 2007). Column 11: Log of  $B$ -band luminosity ( $L_\odot$ ). Column 12: Projected separation or impact parameter (kpc) between radio sightline and centre of galaxy. Column 13: Galaxy inclination. Column 14: Orientation of radio sightline with respect to galaxy’s major axis.

<sup>a</sup> based on SDSS and WISE colours (see text for details) <sup>b</sup> photometric redshift

## APPENDIX B: LITERATURE SAMPLE

The details of the QGPs from literature that are considered in this work (as described in Section 2.2) are provided here.

**Table B1.** Details of the QGPs searched for H I 21-cm absorption in the literature that are included in this work.

Radio Source	$z_{\text{rad}}$	Type	Mor.	Galaxy	$z_{\text{gal}}$	$g - r$	$\log M_*$ ( $M_\odot$ )	$\log L_B$ ( $L_\odot$ )	$b$ (kpc)	$i$ ( $^\circ$ )	$\phi$ ( $^\circ$ )	$\int \tau dv_{10}^{3\sigma}$ ( $\text{km s}^{-1}$ )	$\int \tau dv$ ( $\text{km s}^{-1}$ )	Ref.
(1)	(2)	(3)	(4)	(5)	(6)	(7)	(8)	(9)	(10)	(11)	(12)	(13)	(14)	(15)
J010644.15–103410.6	0.468	Q	R	J010643.93–103419.3	0.1460	0.39	9.9	10.2	23.7	57	83	$\leq 0.063$	—	1
J025134.53+431515.8	1.313	Q	C	J025135.79+431511.7	0.0520	0.81	11.3	10.8	14.6	47	0	$\leq 0.054$	0.26	2
J044858.80–204446.5	1.894	Q	C	J044858.62–204454.7	0.0661	—	—	—	15.6	77	9	$\leq 0.210$	—	3
J085521.37+575144.1	0.368 <sup>a</sup>	U	C	J085519.05+575140.7	0.02600	0.48	9.0	9.2	9.9	49	32	$\leq 0.019$	1.02	4
J091011.01+463617.8	1.020	Q	C	J091010.55+463633.4	0.0998	0.58	10.5	10.4	30.0	23	—	$\leq 0.032$	—	1
J095820.94+322402.2	0.531	Q	C	J095821.07+322211.4	0.00484	0.74	10.0	9.7	11.1	67	76	$\leq 0.009$	0.13	5
J102258.41+123429.7	1.724	Q	R	J102257.92+123439.2	0.1253	0.87	10.7	10.2	33.2	74	22	$\leq 0.095$	—	1
J104257.58+074850.5	2.667	Q	C	J104257.74+074751.3	0.03321	0.50	9.1	9.0	1.7	50	12	$\leq 0.057$	0.19	1
J115917.87+441216.3	1.211	Q	R	J115856.84+441133.8	0.00233	0.48	8.0	8.0	10.9	67	87	$\leq 0.130$	—	6
J120321.93+041419.0	1.224	Q	C	J120322.71+041347.2	0.02036	0.65	9.0	8.8	14.0	76	77	$\leq 0.047$	—	6
J121846.60+173817.2	1.809	Q	C	J121841.78+174308.6	0.00232	0.54	7.6	8.2	13.9	0	0	$\leq 0.168$	—	6
J122106.87+454852.1	0.525	Q	R	J122115.22+454843.2	0.0015	0.08	7.4	7.8	2.7	33	1	$\leq 1.900$	1.39	7
J122154.17+305146.4	0.776	Q	C	J122216.72+305323.5	0.00185	0.53	7.1	7.1	12.0	27	—	$\leq 0.085$	—	6
J122847.42+370612.0	1.517	Q	C	J122828.08+371405.3	0.00132	0.28	7.0	7.6	11.0	13	—	$\leq 0.136$	—	6
J125248.28+474044.0	0.922	Q	R	J125249.22+474106.1	0.0321	0.89	11.0	10.5	18.3	50	68	$\leq 0.190$	—	1
J125757.23+322929.2	0.805	Q	C	J125756.40+322853.9	0.02337	0.44	8.8	9.0	17.4	69	44	$\leq 0.070$	—	6
J132155.68+351037.2	1.918	Q	C	J132227.58+351219.5	0.00215	0.15	6.1	6.9	19.7	54	75	$\leq 0.126$	—	6
J132840.56+622136.9	1.218	Q	C	J132839.89+622136.0	0.0423	0.51	8.9	8.9	4.0	51	14	$\leq 0.126$	—	1
J132846.53–485638.7	—	U	—	J132844.09–485500.5	0.00997	—	—	10.4	20.7	25	—	$\leq 0.030$	0.82	8
J133007.70–205616.2	1.169	Q	R	J133005.30–205558.7	0.0178	—	—	10.1	13.7	52	60	$\leq 0.007$	0.24 <sup>b</sup>	9
J135400.09+565004.9	—	U	R	J135400.68+565000.3	0.09549	0.80	10.7	10.2	11.8	73	80	$\leq 0.038$	3.03	4
J145907.58+714019.9	0.905	Q	—	J145745.71+714056.4	0.00149	—	—	8.6	12.0	54	48	$\leq 0.014$	—	10
J202346.20–365520.5	1.048	Q	—	J202345.21–365505.7	0.02700	—	—	9.9	10.3	66	21	$\leq 0.049$	0.22	3
J225503.89+131333.9	0.543	Q	—	J225503.10+131313.7	0.03253	0.75	11.0	10.6	15.1	41	44	$\leq 0.026$	—	11

Column 1: Radio source name. Column 2: Redshift of radio source. Column 3: Type of radio source – quasar (Q), radio galaxy (G) or unknown (U). Column 4: Morphology of radio source at arcsecond-scale – compact (C) or resolved (R). Column 5: Galaxy name. Column 6: Galaxy redshift. Column 7: Rest-frame SDSS  $g - r$  colour of galaxy. Column 8: Log of stellar mass ( $M_\odot$ ) of galaxy from *kcorrect* (Blanton & Roweis 2007). Column 9: Log of  $B$ -band luminosity ( $L_\odot$ ). Column 10: Projected separation or impact parameter (kpc) between radio sightline and centre of galaxy. Columns 11: Galaxy inclination. Column 12: Orientation of radio sightline with respect to galaxy’s major axis. Column 13:  $3\sigma$  upper limit on integrated H I 21-cm optical depth from spectra smoothed to  $10 \text{ km s}^{-1}$ . Column 14: Integrated H I 21-cm optical depth in case of detections at the observed spectral resolution. Column 15: References for the H I 21-cm optical depth measurements – 1: Borthakur et al. (2011); 2: Hwang & Chiou (2004); 3: Carilli & van Gorkom (1992); 4: Zwaan et al. (2015); 5: Keeney et al. (2005); 6: Borthakur (2016); 7: Borthakur et al. (2014); 8: Reeves et al. (2016); 9: Keeney et al. (2011); 10: Haschick & Burke (1975); 11: Corbelli & Schneider (1990).

<sup>a</sup> photometric redshift <sup>b</sup>  $\int \tau dv$  corresponds to stronger of the two absorption components separated by  $250 \text{ km s}^{-1}$

#### **APPENDIX C: SALT SPECTRA**

The details of the redshifts obtained from the SALT spectra of galaxies are provided in Table C1 and the galaxy spectra are shown in Fig. C1.

#### **APPENDIX D: RADIO OBSERVATION LOG**

The log of the radio observations carried out by us is provided here.

#### **APPENDIX E: RESULTS FROM H I 21-cm SPECTRAL LINE OBSERVATIONS**

The parameters derived from our radio spectral line observations are provided here.

#### **APPENDIX F: H I 21-cm ABSORPTION SPECTRA**

The H I 21-cm absorption spectra towards all the sources observed by us are shown here. The QGP name as given in Table A1 are provided for each spectra.



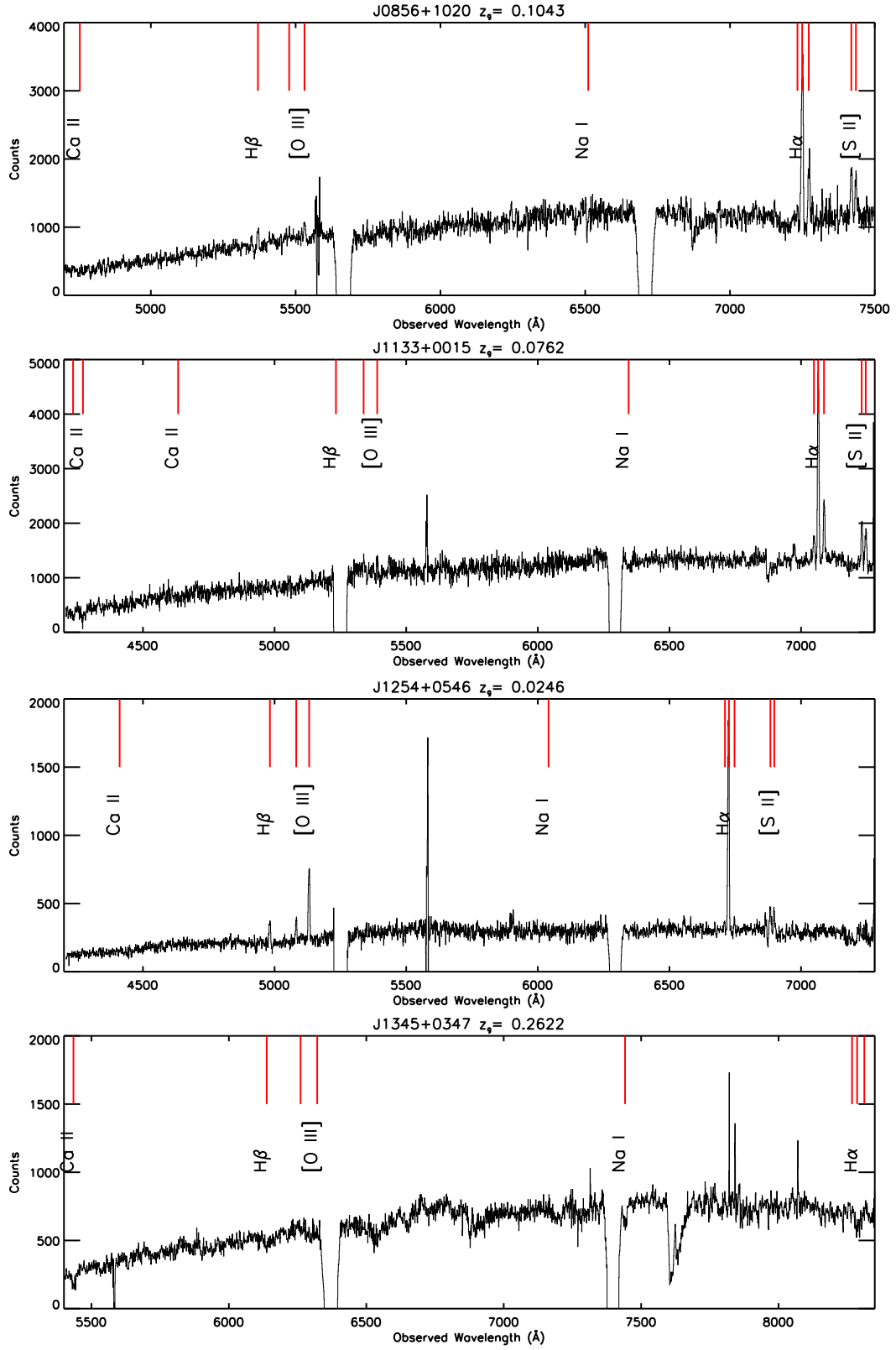


**Figure C1.** SALT spectra for seven of the galaxies in our sample. The expected positions of the H $\alpha$ , H $\beta$ , [O III], [N II], and [S II] emission lines, and Na I and Ca II absorption lines are marked by ticks.

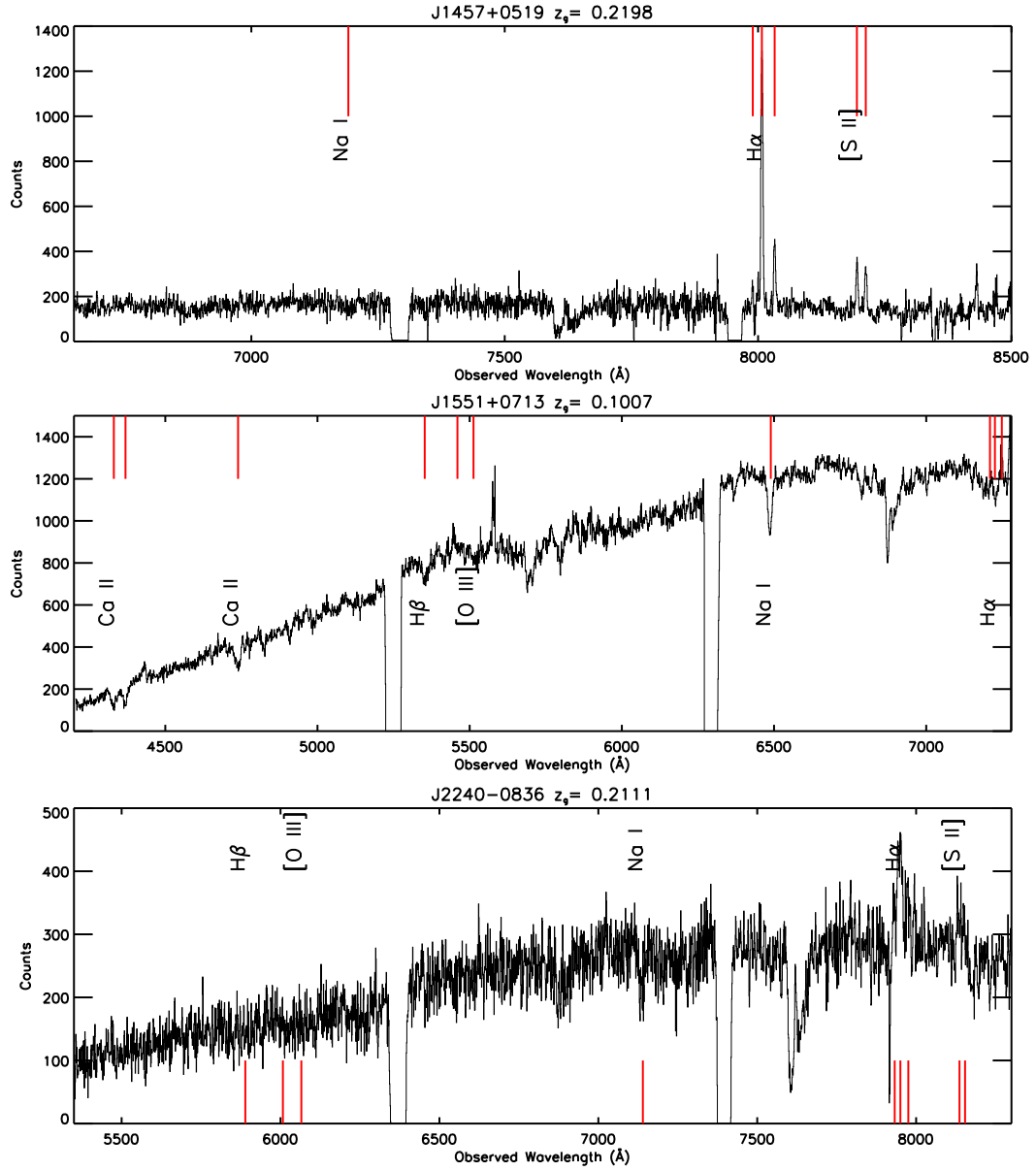


Figure C1. Continued from previous page.

**Table C1.** Details of the galaxy spectra obtained using SALT.

Galaxy (1)	$z_g$ (2)	Emission lines (3)	Absorption lines (4)
J085625.41+102020.1	$0.1043 \pm 0.0005$	H $\alpha$ , H $\beta$ , [O III], [N II], [S II]	Ca II
J113302.01+001541.7	$0.0762 \pm 0.0003$	H $\alpha$ , [O III], [N II], [S II]	Ca II
J125422.21+054610.4	$0.0246 \pm 0.0005$	H $\alpha$ , H $\beta$ , [O III], [N II], [S II]	—
J134528.42+034723.0	$0.2622 \pm 0.0005$	—	H $\alpha$ , H $\beta$ , Na I, Ca II
J145722.40+051918.8	$0.2198 \pm 0.0001$	H $\alpha$ , [N II], [S II]	—
J155121.06+071352.4	$0.1007 \pm 0.0005$	—	H $\alpha$ , H $\beta$ , Na I, Ca II
J224013.49−083633.6	$0.2111 \pm 0.0005$	H $\alpha$ , [N II], [S II]	Ca II

Column 1: Galaxy name. Column 2: Galaxy redshift. Columns 3 and 4: Emission and absorption lines detected in the SALT spectrum, respectively.

**Table D1.** Radio observation log of the sources observed by us.

Radio Source (1)	Galaxy (2)	$z_{\text{gal}}$ (3)	Telescope (4)	Date (5)	$\delta v$ (km s $^{-1}$ ) (6)	Time on source (h) (7)	Beam size (arcsec $^2$ ) (8)	Spatial resolution (kpc $^2$ ) (9)
<i>Primary Sample</i>								
J004126.01−014315.6	J004121.53−014257.0	0.01769	GMRT	17 October 2014	1.8	2.6	$3.4 \times 2.3$	$1.2 \times 0.8$
J004332.71+002459.9	J004333.64+002516.2	0.07975	GMRT	05 September 2014	1.9	2.7	$2.4 \times 2.3$	$3.6 \times 3.4$
J013412.70+000345.2	J013411.28+000327.5	0.05198	GMRT	17 October 2014	1.8	2.4	$2.9 \times 2.3$	$2.9 \times 2.4$
J080240.89+160104.6	J080241.68+160035.2	0.01565	GMRT	03 May 2014	1.7	4.2	$2.8 \times 2.2$	$0.9 \times 0.7$
J081705.49+195842.8	J081707.13+195907.9	0.04363	GMRT	06 September 2014	1.8	2.4	$2.4 \times 2.1$	$2.0 \times 1.8$
J082153.82+503120.4	J082153.74+503125.7	0.1835	GMRT	19 September 2007	3.9	8.0	$3.5 \times 2.4$	$10.7 \times 7.3$
J084957.97+510829.0	J084957.49+510842.3	0.07342	GMRT	19 June 2007	3.5	7.7	$3.2 \times 2.5$	$4.5 \times 3.5$
J084957.97+510829.0	J084958.10+510826.6	0.3120	GMRT	18 July 2011	2.3	2.7	$3.4 \times 2.6$	$15.6 \times 12.0$
				03 July 2012		3.5		
J085624.91+102017.0	J085625.41+102020.1	0.1043	GMRT	25 April 2015	1.9	5.8	$2.5 \times 2.3$	$4.8 \times 4.4$
J091133.45+195814.1	J091134.38+195830.2	0.02293	GMRT	18 October 2014	1.8	5.9	$2.9 \times 2.2$	$1.3 \times 1.0$
J101514.63+163740.4	J101514.22+163758.3	0.05436	GMRT	16 July 2011	1.8	3.0	$2.5 \times 2.2$	$2.6 \times 2.3$
J111023.84+032136.1	J111025.09+032138.8	0.02996	GMRT	01 March 2008	3.4	7.6	$2.4 \times 1.9$	$1.4 \times 1.1$
J112613.04+380216.4	J112612.57+380228.6	0.06190	GMRT	15 July 2011	1.8	4.6	$2.3 \times 2.2$	$2.8 \times 2.6$
J113303.02+001549.0	J113302.01+001541.7	0.0762	GMRT	06 May 2014	1.9	2.2	$3.2 \times 2.1$	$4.6 \times 3.0$
J113303.02+001549.0	J113303.96+001538.2	0.07584	GMRT	06 May 2014	1.9	2.2	$3.2 \times 2.1$	$4.6 \times 3.0$
J115659.62+341216.9	J115659.59+341221.7	0.13797	GMRT	28 February 2015	1.9	5.0	$2.9 \times 2.2$	$7.2 \times 5.5$
J120922.78+411941.3	J120923.25+411949.3	0.17098	GMRT	25 July 2014	2.0	1.6	$4.1 \times 2.3$	$12.0 \times 6.8$
J122847.42+370612.0	J122847.72+370606.9	0.13837	GMRT	02 March 2008	3.7	7.5	$2.5 \times 1.9$	$6.1 \times 4.7$
J124157.54+633241.6	J124157.26+633237.6	0.1430	GMRT	03 March 2008	3.8	7.7	$4.0 \times 2.6$	$10.1 \times 6.5$
				13 June 2009		8.0		
				14 June 2009		5.4		
J124355.78+404358.4	J124357.17+404346.1	0.01693	GMRT	01 July 2010	3.4	4.6	$2.6 \times 2.1$	$0.9 \times 0.7$
J124357.65+162253.3	J124342.64+162335.9	0.00263	GMRT	18 October 2014	1.7	1.6	$2.8 \times 2.2$	$0.2 \times 0.1$
				22 November 2014		2.6		
J125422.19+054619.8	J125422.21+054610.4	0.0246	GMRT	26 May 2014	1.7	2.2	$2.4 \times 2.1$	$1.2 \times 1.0$
				29 August 2014		6.4		
J130028.53+283010.1	J130028.66+283012.1	0.2228	VLA	21 June 2015	0.5	1.9	$2.2 \times 1.8$	$7.9 \times 6.4$
				26 June 2015		1.9		
J130050.09−012146.2	J130049.15−012136.4	0.02275	GMRT	08 November 2014	1.7	4.5	$3.2 \times 2.8$	$1.5 \times 1.3$
J134528.74+034719.7	J134528.42+034723.0	0.2622	GMRT	30 January 2015	2.2	5.3	$3.3 \times 3.2$	$13.5 \times 12.8$
J135907.77+293531.8	J135908.47+293541.5	0.14607	GMRT	17 July 2011	2.0	3.0	$2.9 \times 2.2$	$7.5 \times 5.8$
J142253.22+054013.4	J142253.99+053947.9	0.05422	GMRT	06 March 2015	1.8	3.4	$2.6 \times 2.3$	$2.8 \times 2.4$
J143806.79+175805.4	J143806.76+175802.5	0.1468	GMRT	03 May 2014	2.0	5.1	$3.1 \times 2.3$	$7.9 \times 6.0$
J144304.53+021419.3	J144304.53+021419.3	0.3714	GMRT	02 June 2012	2.3	5.7	$3.9 \times 2.9$	$20.0 \times 15.0$
J145722.53+051921.8	J145722.40+051918.8	0.2198	GMRT	01 May 2014	2.1	3.0	$3.9 \times 2.6$	$13.7 \times 9.2$
J152523.55+420117.0	J152522.99+420131.7	0.09094	GMRT	25 May 2014	1.9	2.2	$3.0 \times 2.6$	$5.2 \times 4.4$
J153905.20+053438.3	J153905.16+053416.5	0.02594	GMRT	25 August 2013	1.8	3.0	$3.2 \times 2.4$	$1.7 \times 1.3$
J155121.13+071357.7	J155121.06+071352.4	0.1007	GMRT	06 May 2014	1.9	2.2	$3.6 \times 2.1$	$6.6 \times 3.9$
				22 November 2014		6.1		
J160658.29+271705.5	J160659.13+271642.6	0.04620	GMRT	25 July 2014	1.8	2.6	$3.4 \times 2.3$	$3.1 \times 2.1$
J163402.95+390000.5	J163403.30+390001.0	0.36620	GMRT	23 November 2014	2.4	2.5	$5.6 \times 2.7$	$28.6 \times 13.6$
J163956.35+112758.7	J163956.37+112802.1	0.0790	GMRT	02 July 2010	3.5	4.2		
				14 July 2010	0.9	3.8	$2.8 \times 2.1$	$4.2 \times 3.1$
				16 July 2010		3.1		
J164315.58+354729.7	J164315.10+354701.6	0.03121	WSRT	18 February 2011	1.1	9.7	$27.0 \times 13.2$	$16.9 \times 8.2$
J164802.37+242916.9	J164804.38+242935.3	0.03583	GMRT	24 July 2014	1.8	2.8	$2.4 \times 2.0$	$1.7 \times 1.4$
J174832.84+700550.8	J174926.43+700839.7	0.00008	GMRT	19 October 2014	1.7	2.6	$3.6 \times 2.4$	$0.1 \times 0.1$
J224013.41−083628.7	J224013.49−083633.6	0.2111	GMRT	06 December 2014	2.1	2.4	$3.3 \times 2.9$	$11.3 \times 10.0$
<i>Supplementary Sample</i>								
J082015.85+082612.6	J082015.88+082610.5	0.0775	GMRT	08 November 2014	1.8	3.5	$2.7 \times 2.2$	$3.9 \times 3.3$
				26 April 2015		5.2		
J091917.06+340049.5	J091917.45+340029.4	0.02376	GMRT	15 July 2011	1.8	3.0	$3.0 \times 1.8$	$1.5 \times 0.9$
J094745.85+111354.0	J094745.85+111354.0	0.1124	GMRT	02 May 2014	1.9	3.0	$4.7 \times 2.0$	$9.6 \times 4.0$
J095433.96+373336.3	J095432.89+373333.1	0.07282	WSRT	04 March 2011	1.1	6.0	$37.4 \times 13.6$	$51.8 \times 18.9$
J095604.34+161418.5	J095604.09+161427.1	0.03346	GMRT	03 July 2010	3.4	2.3	$4.0 \times 2.1$	$2.7 \times 1.4$
J105053.93+000213.6	J105053.93+000213.6	0.2338	GMRT	22 May 2014	2.1	4.7	$3.5 \times 2.6$	$12.8 \times 9.6$
J135947.90+270828.3	J135947.90+270828.3	0.0432	GMRT	02 May 2014	1.8	3.0	$2.9 \times 2.2$	$2.5 \times 1.8$
J143809.90+092016.9	J143810.20+092009.8	0.03029	GMRT	24 August 2014	1.8	2.0	$4.0 \times 2.3$	$2.4 \times 1.4$
J162434.18+232859.9	J162433.76+232912.3	0.09382	GMRT	07 March 2015	1.9	2.4	$2.7 \times 2.3$	$4.7 \times 4.0$
J224247.89−001944.9	J224247.65−001918.7	0.05815	GMRT	19 October 2014	1.8	2.5	$3.7 \times 2.1$	$4.2 \times 2.3$

**Table D1.** Continued from previous page.

Radio Source (1)	Galaxy (2)	$z_{\text{gal}}$ (3)	Telescope (4)	Date (5)	$\delta v$ (km s <sup>-1</sup> ) (6)	Time on source (h) (7)	Beam size (arcsec <sup>2</sup> ) (8)	Spatial resolution (kpc <sup>2</sup> ) (9)
<i>Miscellaneous Sample</i>								
J084600.36+070424.6	J084600.52+070428.8	0.34235	GMRT	01 June 2014	2.3	2.2	$4.3 \times 3.0$	$21.2 \times 14.8$
J094221.98+062335.2	J094221.94+062337.1	0.12390	WSRT	03 March 2011	1.2	9.8		
			GMRT	16 July 2011	1.9	3.0	$2.4 \times 1.8$	$5.3 \times 4.1$
			GMRT	17 July 2011		3.0		
J121417.80+293143.4	J121418.25+293146.7	0.06326	GMRT	24 December 2014	1.8	5.9	$2.8 \times 2.0$	$3.5 \times 2.4$
J164330.03+241951.8	J164331.92+241939.6	0.08723	GMRT	15 July 2011	1.9	4.6	$3.3 \times 2.4$	$5.4 \times 3.9$
J205449.61+004153.0	J205449.64+004149.8	0.20153	VLA	20 June 2015	0.5	1.2	$2.1 \times 1.6$	$6.9 \times 5.3$

Column 1: Radio source name. Column 2: Galaxy name. Column 3: Galaxy redshift. Column 4: Telescope used for radio observation. Column 5: Date of observation. Column 6: Spectral resolution in km s<sup>-1</sup> per channel. Column 7: Time on source in h. Column 8: The size of the restoring beam of the continuum image in arcsec<sup>2</sup>. Column 9: The spatial resolution corresponding to the beam size at the redshift of the galaxy in kpc<sup>2</sup>.

**Table E1.** Parameters derived from radio observations.

QGP	Peak Flux Density (mJy beam <sup>-1</sup> )	$\delta v$ (km s <sup>-1</sup> )	Spectral rms (mJy beam <sup>-1</sup> )	$\sigma_\tau$	$\tau_p$	$\int \tau dv_{10}^{3\sigma}$ (km s <sup>-1</sup> )	$\int \tau dv$ (km s <sup>-1</sup> )	Ref.
(1)	(2)	(3)	(4)	(5)	(6)	(7)	(8)	(9)
<i>Primary Sample</i>								
J0041-0143N	354	1.8	2.3	0.006	—	$\leq 0.070$	—	1
J0041-0143C	67	1.8	2.1	0.033	—	$\leq 0.282$	—	1
J0041-0143S	215	1.8	2.1	0.010	0.08	$\leq 0.094$	$0.52 \pm 0.07$	1
J0043+0024	128	1.9	1.9	0.015	—	$\leq 0.171$	—	2
J0134+0003	907	1.8	2.1	0.002	—	$\leq 0.030$	—	2
J0802+1601	74	1.7	1.6	0.022	—	$\leq 0.286$	—	2
J0817+1958	309	1.8	2.2	0.007	—	$\leq 0.104$	—	2
J0821+5031	48	3.9	0.9	0.019	—	$\leq 0.380$	—	3
J0849+5108.1	248	3.5	1.0	0.004	—	$\leq 0.080$	—	3
J0849+5108.2	233	2.3	2.0	0.009	0.09	$\leq 0.077$	$0.95 \pm 0.06$	4
J0856+1020	54	1.9	1.3	0.024	—	$\leq 0.360$	—	2
J0911+1958	259	1.8	1.4	0.006	—	$\leq 0.084$	—	2
J1015+1637	88	1.8	1.8	0.020	—	$\leq 0.257$	—	2
J1110+0321E	155	3.4	1.1	0.007	—	$\leq 0.080$	—	3
J1110+0321W	223	3.4	0.9	0.004	—	$\leq 0.130$	—	3
J1126+3802	123	1.8	2.4	0.020	—	$\leq 0.254$	—	2
J1133+0015.1	420	1.9	3.0	0.007	—	$\leq 0.095$	—	2
J1133+0015.2	420	1.9	3.0	0.007	—	$\leq 0.095$	—	2
J1156+3412	97	1.9	1.8	0.018	—	$\leq 0.202$	—	2
J1209+4119	178	2.0	2.5	0.014	—	$\leq 0.218$	—	2
J1228+3706	298	3.7	1.1	0.004	—	$\leq 0.070$	—	3
J1241+6332	68	3.8	0.7	0.009	0.16	$\leq 0.170$	$2.90 \pm 0.16$	3
J1243+4043	196	3.4	1.5	0.008	0.18	$\leq 0.131$	$2.26 \pm 0.10$	2
J1243+1622N	1257	1.7	1.6	0.001	—	$\leq 0.030$	—	2
J1243+1622C	419	1.7	1.3	0.003	—	$\leq 0.060$	—	2
J1243+1622S	645	1.7	1.4	0.002	—	$\leq 0.030$	—	2
J1254+0546	109	1.7	0.8	0.008	—	$\leq 0.250$	—	2
J1300+2830	119	0.5	3.9	0.033	—	$\leq 0.239$	—	2
J1300-0121	132	1.7	1.9	0.015	—	$\leq 0.205$	—	2
J1345+0347	91	2.2	1.1	0.013	—	$\leq 0.182$	—	2
J1359+2935	104	2.0	2.5	0.024	—	$\leq 0.316$	—	2
J1422+0540	220	1.8	2.0	0.009	—	$\leq 0.133$	—	2
J1438+1758	53	2.0	1.3	0.024	0.38	$\leq 0.254$	$4.89 \pm 0.19$	2
J1443+0214	163	2.4	0.9	0.006	0.33	$\leq 0.072$	$3.40 \pm 0.10$	4
J1457+0519	157	2.1	2.1	0.014	—	$\leq 0.135$	—	2
J1525+4201	93	1.9	1.9	0.021	—	$\leq 0.235$	—	2
J1539+0534	124	1.8	1.8	0.015	—	$\leq 0.179$	—	2
J1551+0713	68	1.9	1.0	0.015	—	$\leq 0.265$	—	2
J1606+2717	214	1.8	2.0	0.010	—	$\leq 0.140$	—	2
J1634+3900	1100	2.4	1.7	0.002	—	$\leq 0.021$	—	2
J1639+1127	155	0.9	1.6	0.012	0.71	$\leq 0.088$	$15.70 \pm 0.13$	5
J1643+3547	126	1.1	1.4	0.011	—	$\leq 0.110$	—	2
J1648+2429	293	1.8	2.1	0.007	—	$\leq 0.111$	—	2
J1748+7005	977	1.7	3.8	0.004	—	$\leq 0.077$	—	2
J2240-0836	171	2.1	3.9	0.009	—	$\leq 0.309$	—	2
<i>Supplementary Sample</i>								
J0820+0826	106	1.8	1.0	0.010	—	$\leq 0.157$	—	2
J0919+3400E	66	1.8	2.5	0.039	—	$\leq 0.490$	—	2
J0919+3400W	38	1.8	2.4	0.063	—	$\leq 0.797$	—	2
J0947+1113	227	1.9	2.7	0.012	—	$\leq 0.162$	—	2
J0954+3733	311	1.1	1.7	0.005	—	$\leq 0.075$	—	2
J0956+1614N	73	3.4	1.7	0.023	—	$\leq 0.460$	—	2
J0956+1614S	35	3.4	1.7	0.049	—	$\leq 0.718$	—	2
J1050+0002	59	2.1	1.2	0.021	—	$\leq 0.293$	—	2
J1359+2708	142	1.8	1.8	0.013	—	$\leq 0.220$	—	2
J1438+0920	59	1.8	2.1	0.036	—	$\leq 0.442$	—	2
J1624+2328	120	1.9	1.8	0.015	—	$\leq 0.187$	—	2
J2242-0019	291	1.8	2.6	0.009	—	$\leq 0.114$	—	2

**Table E1.** Continued from previous page.

QGP	Peak Flux Density (mJy beam <sup>-1</sup> )	$\delta v$ (km s <sup>-1</sup> )	Spectral rms (mJy beam <sup>-1</sup> )	$\sigma_\tau$	$\tau_p$	$\int \tau dv_{10}^{3\sigma}$ (km s <sup>-1</sup> )	$\int \tau dv$ (km s <sup>-1</sup> )	Ref.
(1)	(2)	(3)	(4)	(5)	(6)	(7)	(8)	(9)
<i>Miscellaneous Sample</i>								
J0846+0704	155	2.3	3.7	0.024	—	$\leq 0.333$	—	2
J0942+0623	116	2.0	1.9	0.016	0.70	$\leq 0.215$	$49.90 \pm 0.40$	6
J1214+2931	59	1.8	1.8	0.030	—	$\leq 0.390$	—	2
J1643+2419	199	1.9	1.8	0.009	—	$\leq 0.157$	—	2
J2054+0041	362	0.5	9.5	0.022	0.61	$\leq 0.174$	$29.92 \pm 0.22$	2

Column 1: QGP name as given in Table A1. Column 2: Peak flux density in mJy beam<sup>-1</sup>. Column 3: Spectral resolution in km s<sup>-1</sup> per channel. Column 4: Spectral rms in mJy beam<sup>-1</sup>. Column 5: Standard deviation of the H I 21-cm optical depth. Column 6: Maximum H I 21-cm optical depth in case of H I 21-cm detections. Column 7:  $3\sigma$  upper limit on integrated H I 21-cm optical depth from spectra smoothed to 10 km s<sup>-1</sup>. Column 8: Integrated H I 21-cm optical depth in case of H I 21-cm detections. Column 9: References — 1: Dutta et al. (2016); 2: This work; 3: Gupta et al. (2010); 4: Gupta et al. (2013); 5: Srianand et al. (2013); 6: Srianand et al. (2015).

Note that the values in Columns 4, 5, 6 and 8 are at the spectral resolution specified in Column 3.



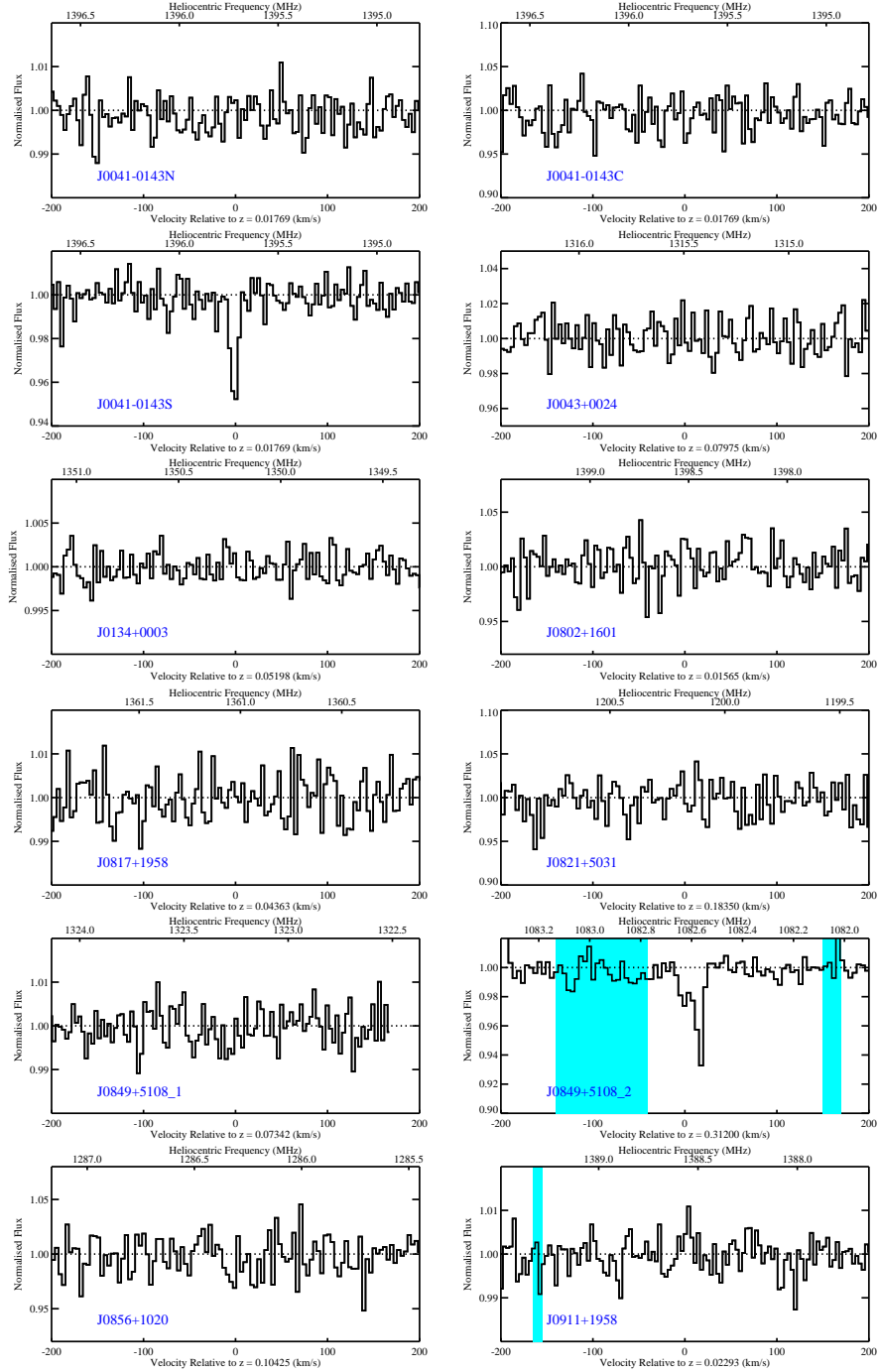


**Figure F1.** H I 21-cm absorption spectra towards the radio sources in our primary sample, smoothed to  $\sim 4 \text{ km s}^{-1}$ . The shaded regions are affected by RFI.

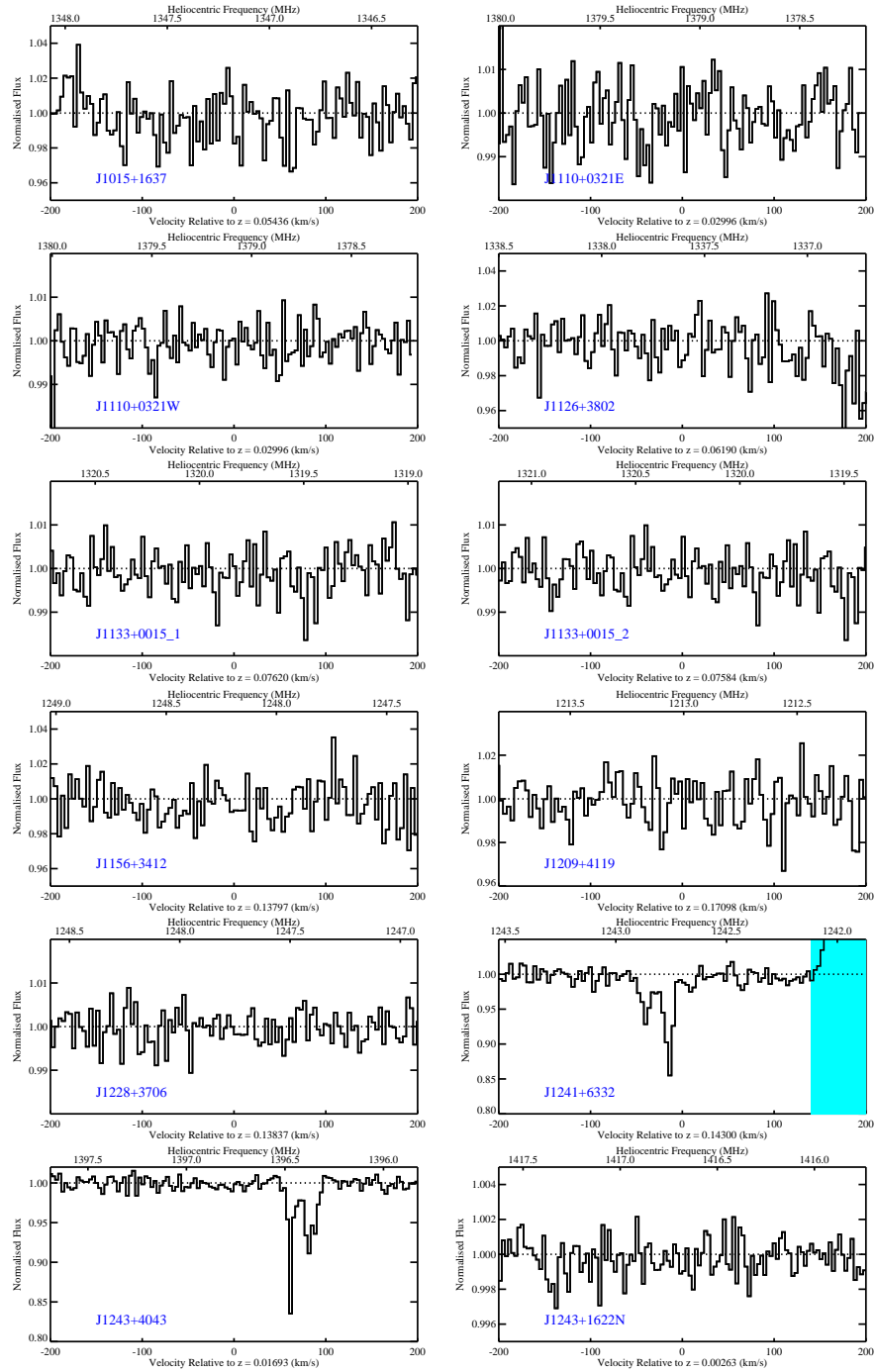


Figure F1. Continued from previous page.

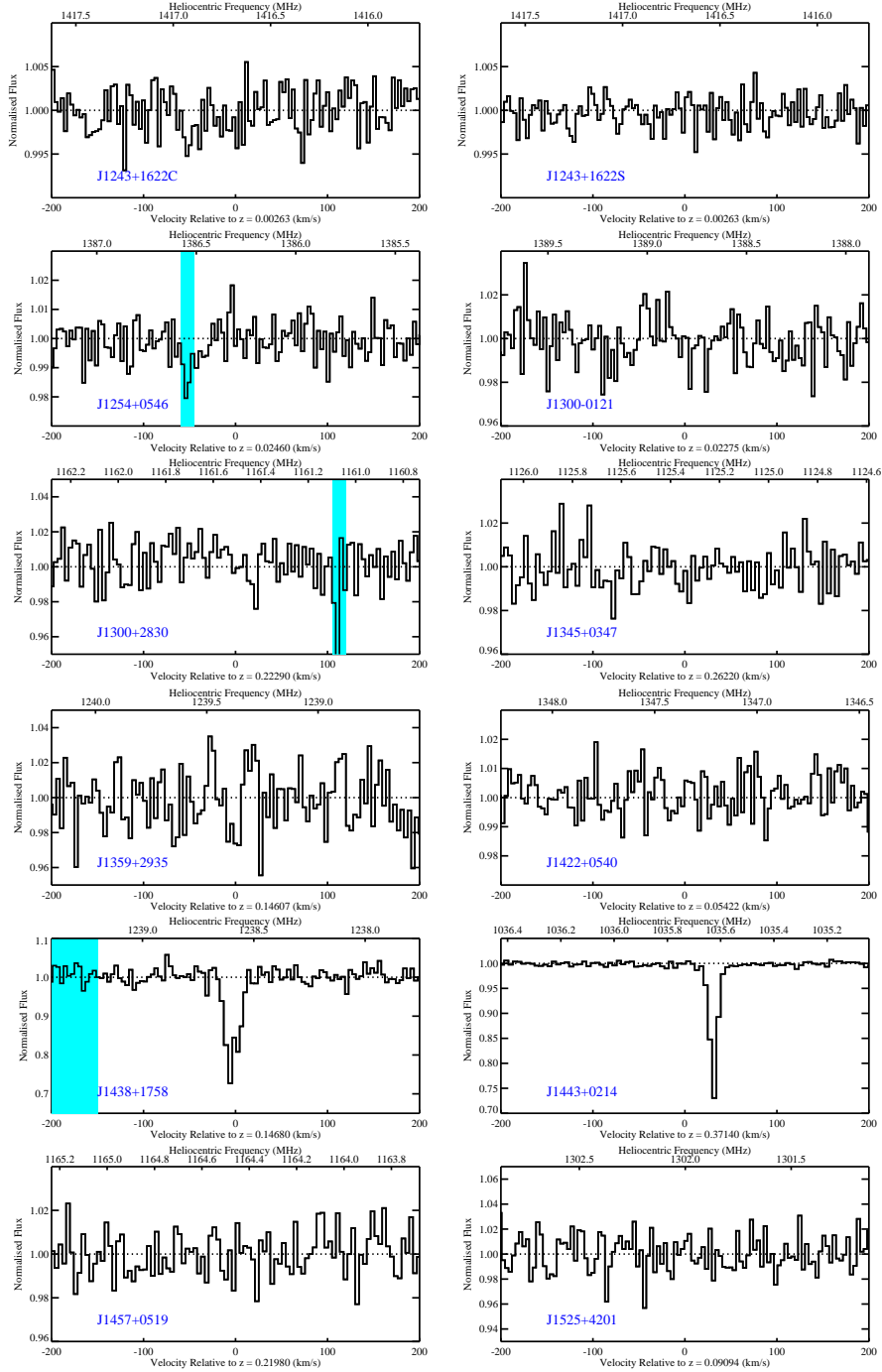
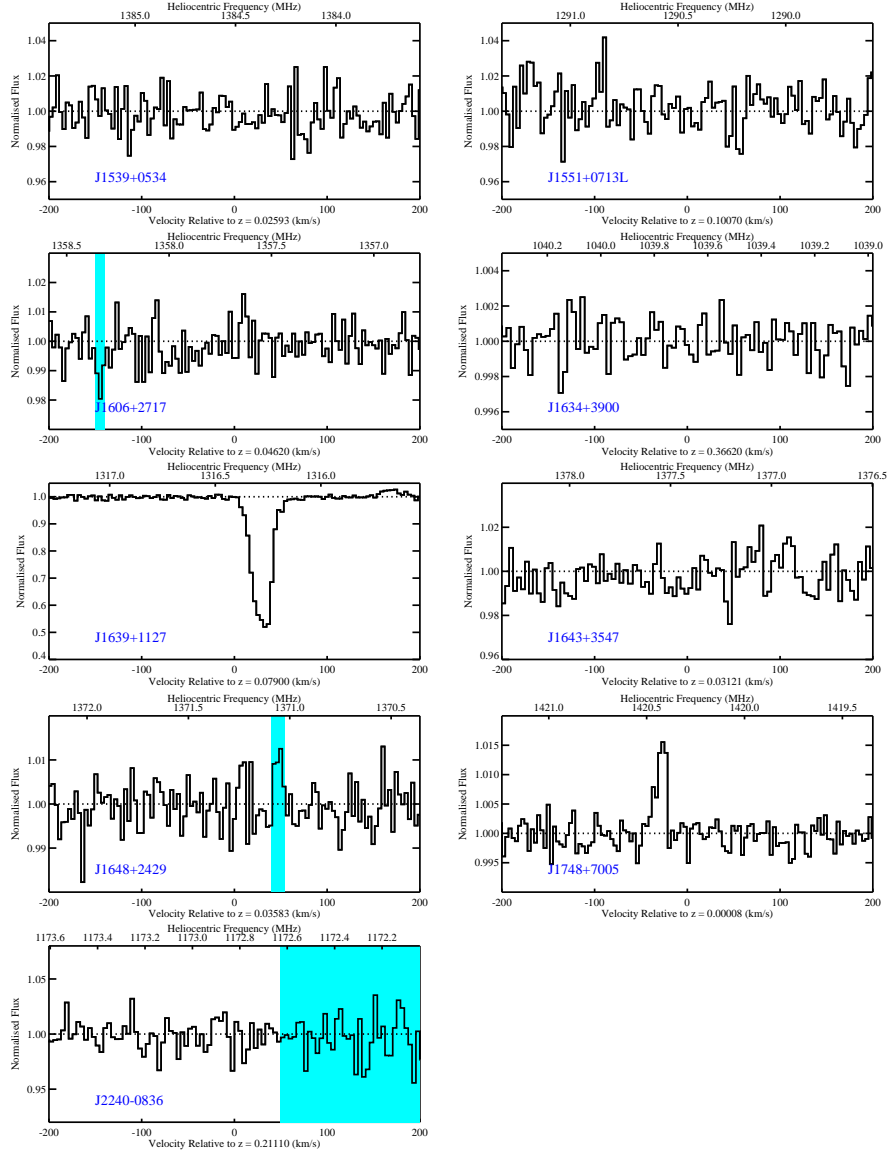
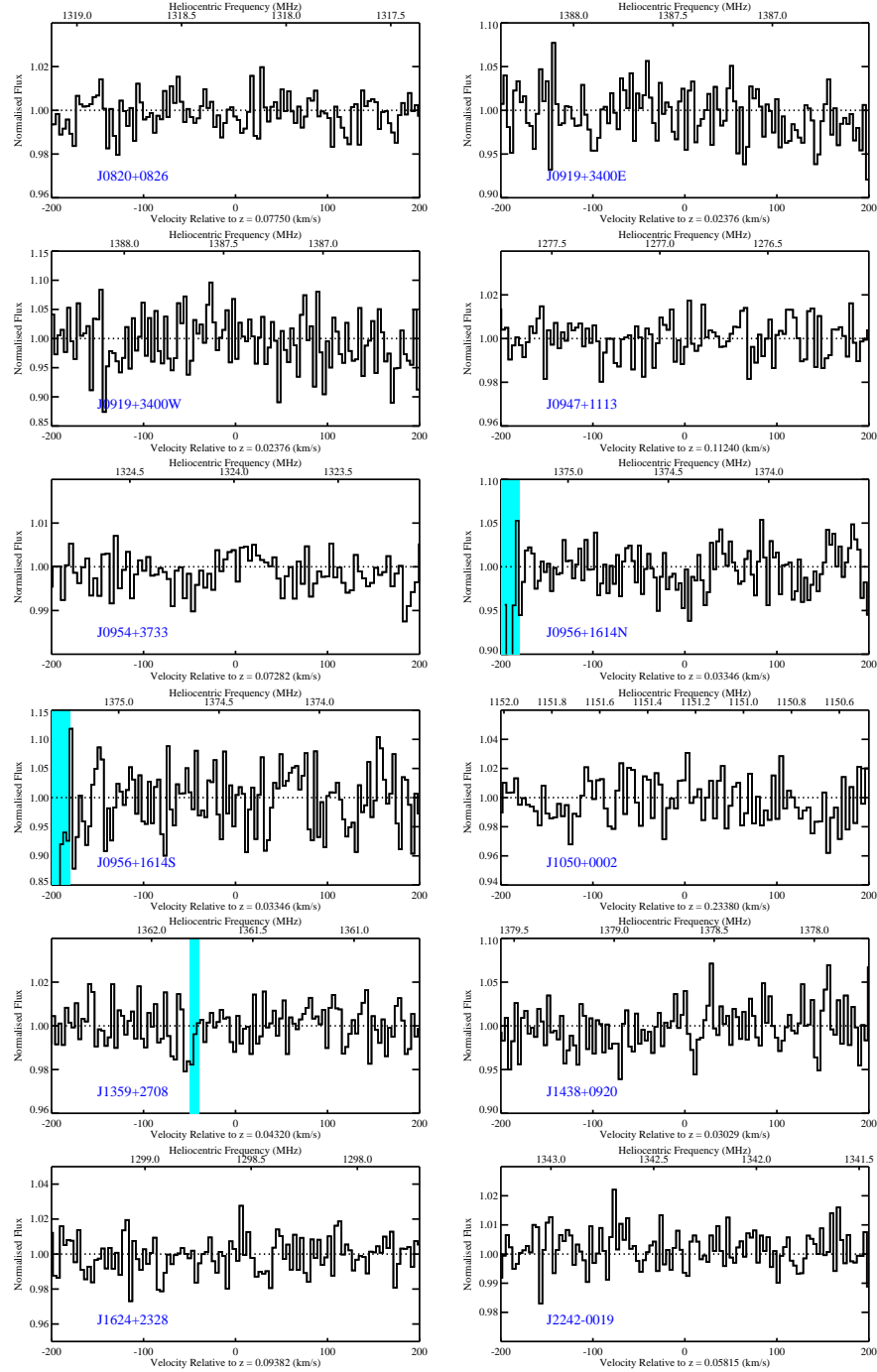
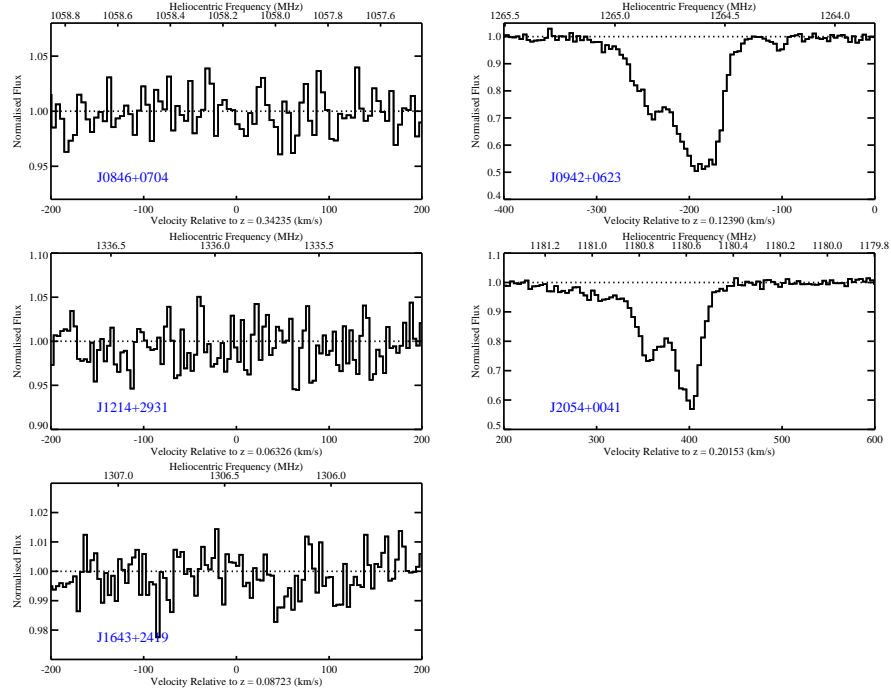


Figure F1. Continued from previous page.

**Figure F1.** Continued from previous page.



**Figure F2.** Same as in Fig. F1 for the radio sources in the supplementary sample.



**Figure F3.** Same as in Fig. F1 for the radio sources in the miscellaneous sample.